Lappeenranta
University of Technology

Antti Uusitalo

WORKING FLUID SELECTION AND DESIGN OF SMALL-SCALE WASTE HEAT RECOVERY SYSTEMS BASED ON ORGANIC RANKINE CYCLES

Thesis for the degree of Doctor of Science (Technology) to be presented with due permission for public examination and criticism in the Auditorium 1383 at Lappeenranta University of Technology, Lappeenranta, Finland on the 10th of December, 2014, at noon.

Acta Universitatis
Lappeenrantaensis 615

Supervisors Academy Research Fellow Teemu Turunen-Saaresti
Laboratory of Fluid Dynamics
LUT Energy
Lappeenranta University of Technology
Finland

Professor Jari Backman
Laboratory of Fluid Dynamics
LUT Energy
Lappeenranta University of Technology
Finland

Reviewers Professor Martijn van den Broek
Department of Industrial System and Product Design
Ghent University
Belgium

Professor Costante Invernizzi
Department of Mechanical and Industrial Engineering
University of Brescia
Italy

Opponent Professor Martijn van den Broek
Department of Industrial System and Product Design
Ghent University
Belgium

ISBN 978-952-265-710-7
ISBN ISBN 978-952-265-711-4 (PDF)
ISSN-L 1456-4491
ISSN 1456-4491
Lappeenrannan teknillinen yliopisto
Yliopistopaino 2014

Abstract

Antti Uusitalo
Working fluid selection and design of small-scale waste heat recovery systems based on organic Rankine cycles
Lappeenranta 2014
130 pages
Acta Universitatis Lappeenrantaensis 615
Diss. Lappeenranta University of Technology
ISBN 978-952-265-710-7, ISBN 978-952-265-711-4 (PDF), ISSN 1456-4491

Demand for the use of energy systems, entailing high efficiency as well as availability to harness renewable energy sources, is a key issue in order to tackling the threat of global warming and saving natural resources. Organic Rankine cycle (ORC) technology has been identified as one of the most promising technologies in recovering low-grade heat sources and in harnessing renewable energy sources that cannot be efficiently utilized by means of more conventional power systems. The ORC is based on the working principle of Rankine process, but an organic working fluid is adopted in the cycle instead of steam.

This thesis presents numerical and experimental results of the study on the design of small-scale ORCs. Two main applications were selected for the thesis: waste heat recovery from small-scale diesel engines concentrating on the utilization of the exhaust gas heat and waste heat recovery in large industrial-scale engine power plants considering the utilization of both the high and low temperature heat sources. The main objective of this work was to identify suitable working fluid candidates and to study the process and turbine design methods that can be applied when power plants based on the use of non-conventional working fluids are considered. The computational work included the use of thermodynamic analysis methods and turbine design methods that were based on the use of highly accurate fluid properties. In addition, the design and loss mechanisms in supersonic ORC turbines were studied by means of computational fluid dynamics.

The results indicated that the design of ORC is highly influenced by the selection of the working fluid and cycle operational conditions. The results for the turbine designs indicated that the working fluid selection should not be based only on the thermodynamic analysis, but requires also considerations on the turbine design. The turbines tend to be fast rotating, entailing small blade heights at the turbine rotor inlet and highly supersonic flow in the turbine flow passages, especially when power systems with low power outputs are designed. The results indicated that the ORC is a potential solution in utilizing waste heat streams both at high and low temperatures and both in micro and larger scale applications.

Keywords: organic Rankine cycle, working fluid selection, waste heat recovery, turbine design, supersonic flow
UDC: 662.99:536.7:620.9:62-135:004.942

Acknowledgements

This thesis work was carried out at the Lappeenranta University of Technology Finland, in the Laboratory of Fluid Dynamics between years 2010 and 2014. The research was funded by the Finnish Graduate School in Computational Fluid Dynamics, LUT micro-ORC project, Finnish Cluster for Energy and Environment (Cleen Ltd.) FCEP-project, and Henry Ford Foundation. Part of the research was financed by the Finnish Funding Agency for Technology and Innovation (Tekes).

I would like to express my sincere gratitude to Professor Jari Backman, Academy Research Fellow Teemu Turunen-Saaresti, and Professor Jaakko Larjola for guiding, supervising, and offering the possibility to do this research. I would like to thank all the people at the Laboratory of Fluid Dynamics for interesting discussions and guidance during the years. Special thanks go to Associate Professors Aki Grönman and Ahti Jaatinen-Värri, and Researcher Juha Honkatukia for helping me to conduct this work.

I would like to thank my reviewers Professor Martijn van den Broek and Professor Costante Invernizzi for their valuable and constructive comments during the review process that helped me to improve the quality of the work. I would also like to thank Professor Piero Colonna and his research group at TU Delft for all the help and guidance during my research exchange period in the Netherlands in 2012. Many thanks to Assistant Professor Alberto Guardone from Politecnico Di Milano for helping me in the research on supersonic flows.

Finally, I would like to thank my family Saila, Eetu, Timo, Seija, and Ville for supporting, listening, and encouraging me on this path. Without your help and support during these years it would have been impossible to conduct this work.

Antti Uusitalo
November 2014
Lappeenranta, Finland

Contents

Abstract

Acknowledgments

Contents

List of publications supporting the present monograph

1 Introduction **11**

2 Organic Rankine Cycles **13**
2.1 Working principle 13
2.2 Literature review 14
2.2.1 Applications 15
2.2.2 Working fluid selection and process design considerations 16
2.2.3 Studies on waste heat recovery by means of ORC from diesel and gas engines and gas turbines 18
2.2.4 Studies on micro-scale ORC power cycles 20
2.2.5 Special features of ORC turbines 21
2.2.6 Conclusions and discussions based on the literature 23
2.3 ORC process based on high-speed turbogenerator technology 24

3 Numerical methods **27**
3.1 Thermodynamic analysis and process design methods 27
3.2 Turbine design methods 31
3.3 Computational fluid dynamics 37
3.3.1 Real Gas Model 38
3.3.2 Stator and nozzle simulations 40
3.3.3 Rotor simulations 40
3.3.4 Convergence monitoring 42

4 Study on dry ORC working fluids **43**
4.1 Thermodynamic analysis 43
4.1.1 The relation between the molecular weight and the critical temperature and critical pressure 45
4.1.2 Cycle efficiency 45
4.1.3 Condensing pressure and expansion ratio over the turbine 47
4.1.4 Enthalpy change over the turbine 49
4.1.5 Speed of sound 50
4.2 Turbine design considerations with different working fluids 51
4.2.1 Turbine design as a function of turbine power output 52
4.2.2 Effect of the degree of reaction on the turbine design 57

4.2.3 Effect of the turbine inlet pressure on the cycle efficiency and on the turbine design . . . 58
4.3 Conclusions and discussion . . . 60

5 Siloxanes as working fluids in mini ORC systems 63
5.1 Results . . . 65
5.1.1 Design point results . . . 65
5.1.2 Effect of the condensing temperature on the cycle performance and process design . . . 69
5.1.3 Turbine design considerations . . . 71
5.2 Conclusions and discussion . . . 73

6 Radial turbine design for a micro-ORC test setup 75
6.1 Design and flow analysis of the turbine . . . 75
6.1.1 Expansion in a converging-diverging nozzle . . . 77
6.1.2 Stator simulations . . . 78
6.1.3 Rotor simulations . . . 86
6.2 Conclusions and discussion . . . 90

7 Waste heat recovery of large scale reciprocating engine 93
7.1 Results of thermodynamic analysis . . . 94
7.1.1 Exhaust gas heat utilization . . . 94
7.1.2 Charge air heat utilization . . . 96
7.1.3 The effect of the condensing temperature and the minimum pinch-point temperature difference on the ORC performance . . . 99
7.1.4 Case study . . . 99
7.2 Experimental results for charge air utilization . . . 101
7.2.1 Description of the experimental setup . . . 101
7.2.2 Condensing conditions . . . 104
7.2.3 Experimental results at 100 % engine load . . . 104
7.2.4 Experimental results at engine part load . . . 105
7.2.5 Process with pressure reduction system replaced with a turbine . . . 107
7.3 Conclusions and discussion . . . 110

8 Summary and recommendations 113

References 117

List of publications supporting the present monograph

The present monograph contains both material that has been published previously by the author elsewhere and material, that has not been published before. A large part of the results presented in the present monograph are related to the following scientific publications. Antti Uusitalo is the principal author of the papers.

Scientific journal papers

Publication I: Uusitalo A., Turunen-Saaresti T., Honkatukia J., Colonna P., and Larjola J. (2013). Siloxanes as Working Fluids for Mini-ORC Systems Based on High-Speed Turbogenerator Technology. *Journal of Engineering for Gas Turbines and Power*, 135(4):042305, pp.1-9.

Chapter 5 is based on the results presented in this paper. The use of siloxanes as working fluids in mini-scale ORC systems is studied and discussed in Publication I by means of thermodynamic analysis. The author was responsible for the numerical work presented in this paper.

Publication II: Uusitalo A., Honkatukia J., Turunen-Saaresti T., and Larjola J. (2014). A Thermodynamic Analysis of Waste Heat Recovery from Reciprocating Engine Power Plants by means of Organic Rankine Cycles. *Applied Thermal Engineering*, 70(1), pp. 33-41.

Section 7.1 is based on the results presented in this paper. The waste heat recovery in large-scale reciprocating engines by means of ORC is studied and discussed in Publication II by means of thermodynamic analysis. The author was responsible for the numerical work presented in this paper.

Refereed conference articles

Publication III: Uusitalo A., Turunen-Saaresti T., Guardone A., and Grönman A. (2014). Design and Modeling of Highly Supersonic Small Scale Radial ORC Turbine Stator with High Molecular Complexity Working Fluids. Proceedings of ASME Turbo Expo 2014, GT2014-26204, 16-20 June 2014, Düsseldorf, Germany.

The results presented in section 6.1 are partly based on the results presented in this paper. The paper presents the design and flow analysis of a highly supersonic turbine stator. The author was responsible for the numerical work including the design of the stator geometry, pre processign, numerical modelling, and post processing. Alberto Guardone from Politecnico Di Milano provided the design tool for supersonic nozzles used in the design of the studied turbine stator.

Nomenclature

Latin alphabet

A	Heat transfer area,	m^2
a	Speed of sound,	m/s
b	Width,	m
c	Absolute flow velocity,	m/s
c_p	Isobaric heat capacity,	kJ/kgK
c_r	Radial component of the absolute velocity,	m/s
c_u	Tangential component of the absolute velocity,	m/s
C_d	Drag coefficient,	-
d	Distance along the flow direction,	m
D	Diameter,	m
D_s	Specific diameter,	-
h	Specific enthalpy,	kJ/kg
k	Thermal conductivity,	W/mK
L	Length,	m
Ma	Mach number,	-
n	Rotational speed,	rpm, 1/s
N_s	Specific speed,	-
P	Power,	W
p	Pressure,	Pa, bar
q_m	Mass flow rate,	kg/s
q_v	Volumetric flow rate,	m^3/s
r	Degree of reaction,	-
s	Specific entropy,	kJ/kgK
T	Temperature,	^{o}C,K
t	Blade height,	m
U	Heat transfer coefficient,	W/m^2K
u	Peripheral speed,	m/s
v	Specific volume,	m^3/kg
w	Relative velocity,	m/s
y^+	Nondimesional wall distance,	-

Greek alphabet

α	Flow angle,	deg
β	Relative flow angle/Shock wave angle,	deg
Γ	Fundamental derivative of gas dynamics,	-
ε	Recuperator effectiveness,	-
η	Efficiency,	-
θ	Circumferential angle/Wake angle,	deg
μ	Dynamic viscosity,	Pa s
ρ	Density,	kg/m^3
ϕ	Heat rate,	W
ω	Angular speed,	rad/s

Subscripts

ad	Acid dew point
c	Condensing
co	Condenser
crit	Critical
des	Design point
e	Electric
ev	Evaporator/evaporation
fp	Feed pump
gm	Generator and mechanical
h	Blade hub
hs	Heat source
in	Inlet
inv	Frequency converter
l	Liquid
max	Maximum
mis	Miscellaneous
m	Motor
LMTD	Log Mean Temperature Difference
net	Net
out	Outlet
pl	Pressure loss
pp	Pinch-point
ref	Reference
re	Recuperator
rot	Rotor
r	Radial/Radius
sh	Superheating
sp	Shaft power
s	Isentropic
st	Stator/Static
theo	Theoretical
tot	Total
t	Turbine/Blade tip/Throat
v	Vapour
wf	Working fluid

Abbreviations

AA	Acyclic Alkene
BCA	Branched-Chain Alkane
CA	Cycloalkane/Charge Air
CAC	Charge Air Cooler
CFD	Computational Fluid Dynamics
CHP	Combined Heat and Power
CS	Cyclic Siloxane

EG	Exhaust Gas
FC	Fluorocarbons
HMC	High Molecular Complexity
LA	Linear Alkane
LMC	Low Molecular Complexity
LS	Linear Siloxane
LUT	Lappeenranta University of Technology
MOC	Method Of Characteristics
ORC	Organic Rankine Cycle
PL	Pressure Loss
VTT	Technical Research Centre of Finland

1 Introduction

This thesis work has been carried out as a part of the research projects on organic Rankine cycle (ORC) technology at Lappeenranta University of Technology (LUT). The laboratory of Fluid Dynamics at LUT has a long history of the research on high-speed turbomachinery. Several research projects and test setups have been realized during the years on high-speed turbines, compressors, refrigeration machines, and ORC power plants. The high-speed technology concept allows the design of compact and maintenance free processes that are completely hermetic. Several dissertations and research papers have been published in the field of high-speed technology, presenting the main findings on the numerical and experimental work done on turbine and compressor research for different applications. The results presented in this thesis are a continuation of the research on ORC power plants adopting high-speed turbogenerator technology.

The growing concerns on the negative environmental impacts of energy production systems based on the use of fossil fuels have been increasing during the last decades. The use of renewable energy sources and the production of carbon neutral energy can be identified as potential solutions, in tackling the problems related to the threat of global warming. Systems based on ORC have been identified as a potential candidate in small-scale and low-temperature energy systems in producing electricity with minor environmental impacts. The working principle of ORC power plants is based on the conventional Rankine process, but an organic substance is adopted in the cycle instead of steam. The ORC technology has been proven successful in geothermal power, small biomass power plants, as well as in small-scale and low-temperature waste heat recovery applications, such as the exhaust gas heat recovery from reciprocating engines and gas turbines and in the utilization of low grade industrial waste heat (Schuster et al., 2009; Tchanche et al., 2011).

This thesis presents the main findings of studies on implementing the ORC technology to recover waste heat streams of existing prime movers. Two main applications were selected for the study: the exhaust gas heat recovery from small-scale diesel engines that can be found in numerous applications such as remote stationary power systems and mobile vehicles and the heat recovery from industrial-scale power plant engines. The selection of the studied applications was based on the literature review and knowledge gained from the industrial partners that have been participating in the research projects. The objectives of this study can generally be divided into four parts:

1) To identify potential working fluid candidates for the studied waste heat recovery applications and to discuss the effect of working fluid selection on the design and optimization of ORCs.

2) To study the design of micro-scale ORCs adopting high-speed turbogenerator technology.

3) To study the design and loss mechanisms of supersonic radial turbines, adopting high

molecular complexity working fluids.

4) To study the potential of the exhaust gas and charge air heat recovery in industrial scale power plant engines.

The structure of the thesis is as follows: Chapter 2, Organic Rankine Cycle, describes the main principles and features of ORC power systems and shortly presents the most common ORC applications, cycle configuration options, as well as the special features related to the design of ORC turbomachinery based on a literature review. Chapter 3, Numerical methods, presents the numerical methods used in this thesis work in the design and modelling of ORC power systems, as well as the methods used in the turbine design and computational fluid dynamics (CFD) flow analysis. Chapter 4, Study on dry ORC working fluids, presents the main results of a study on special features related to the use of fluids from different fluid groups that have been identified as suitable in ORC systems as well as discusses the effect of critical temperature of the fluid on the ORC design. In addition, the main results of a simplified radial turbine design with different working fluids as a function of turbine power are presented. Chapter 5, Siloxanes as working fluids in mini ORC systems, discusses the use of siloxanes as working fluids in micro-scale ORC processes adopting high-speed turbogenerator technology for waste heat recovery in small diesel engines. Chapter 6, Radial turbine design for a micro-ORC test setup, presents a detailed design and flow analysis of a supersonic small-scale ORC turbine, adopting working fluid with high molecular complexity. Chapter 7, Waste heat recovery of large scale reciprocating engine, presents the main results of a work aiming to study the heat recovery potential in industrial scale reciprocating engines as well as presents the experimental results for the charge air heat utilization by means of an experimental ORC setup. Chapter 8, Summary and recommendations, summarizes the main findings presented in this thesis as well as contains recommendations and suggestions for the future research.

The literature review has been carried out solely by the author. The numerical work presented in this thesis has been carried out by the author, including the thermodynamic calculations, turbine design calculations, and the CFD calculations. The thermodynamic analysis tool and the turbine design tool have been developed at LUT, and they were further modified for the current study by the author. The measurements presented in Chapter 7 were carried out at the Technical Research Centre of Finland (VTT) and were not made by the author. The post processing of the experimental results has been carried out by the author and Juha Honkatukia.

The first scientific contribution of this work is to provide knowledge on the selection of suitable working fluids for small-scale ORCs adopting turbine technology and highlight the most important aspects in the design of small-scale high-expansion ratio radial turbines for ORC applications. The second scientific contribution of this work is the numerical and experimental work on studying the utilization of different waste heat streams by means of ORC in industrial-scale engine power plants.

2 Organic Rankine Cycles

2.1 Working principle

Power conversion systems based on the conventional Rankine process are a widely implemented technology in different types of power plants. However, the use of steam as the working fluid may not be feasibe if the power level is low or if the temperature level of the process is low, mainly due to the difficulties related to the turbine design and obtainable efficiency with steam (Larjola, 1995). When adopting organic fluids instead of steam the low temperature heat streams can be utilized more efficiently, if the turbine inlet temperature level is below approximately 400 ^{o}C or if the power level is below 1 MW - 2 MW(Angelino and Moroni, 1973; Larjola, 1995; Hung et al., 1997). Working fluids can be divided into three categories, based on the shape of the saturated vapor line in a temperature-entropy diagram. Fluids having a positive slope (dT/ds) can be identified as dry fluids, fluids with a nearly infinitely large slope as isentropic fluids, and fluids having a negative slope as wet fluids (Hung et al., 1997). Examples of the saturation vapor line of a wet, an isentropic, and a dry fluid are presented in Figure 2.1.

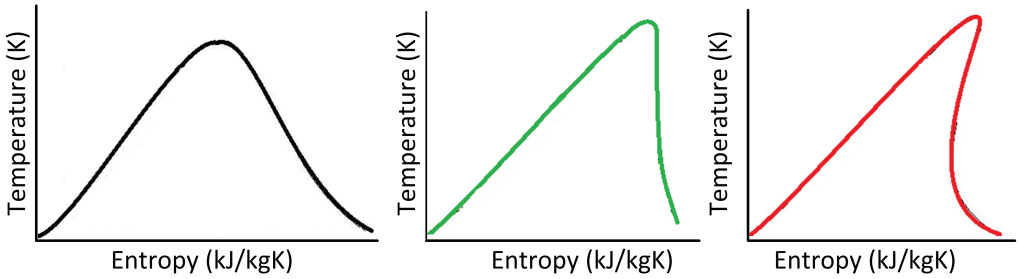

Figure 2.1: Examples of a wet, an isentropic, and a dry fluid in a T,s-diagram.

The main components of a simple ORC are the evaporator, expander, condenser, and a feed pump. The ORC expander can be a turbine (Angelino et al., 1984; Larjola, 1995) or an expander classified as a volumetric expander, namely a screw (Wang et al., 2011), a piston (Seher et al., 2012), or a scroll expander (Lemort et al., 2009; Quoilin et al., 2010). If a working fluid having a dry expansion is used in the process, and thus, the working fluid vapor exits the expander at a superheated state, a recuperator can be used to improve the cycle efficiency. The recuperator is an internal heat exchanger in which the liquid working fluid entering the evaporator can be preheated by using the superheated vapor exiting the expander (Angelino et al., 1984). A simplified process flow diagram of a typical ORC process, having a recuperator, is presented in Figure 2.2. A simplified T,s-diagram of a subcritical ORC process, having a saturated expander inlet state, is presented in Figure 2.3a, a slightly superheated ORC process is presented in Figure 2.3b and a supercritical process in Figure 2.3c.

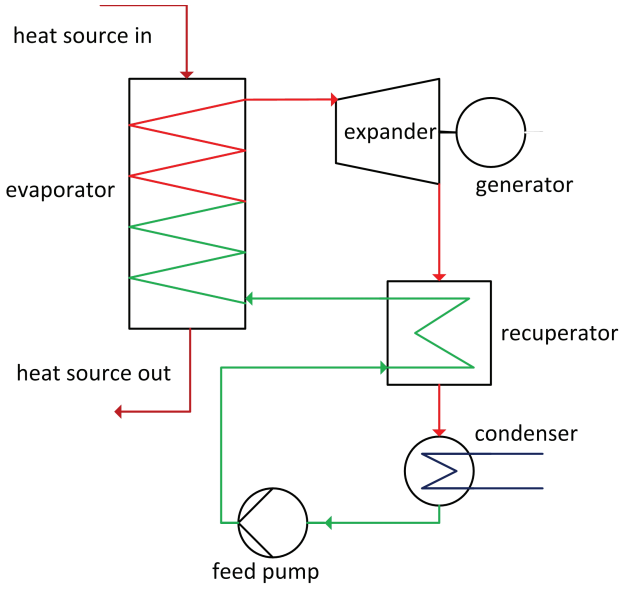

Figure 2.2: Simplified ORC process flow diagram.

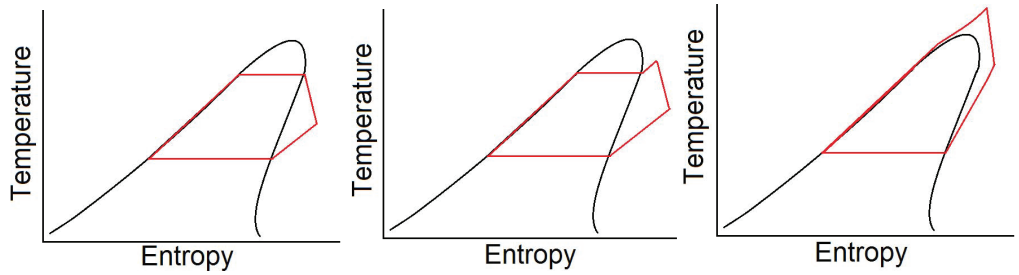

Figure 2.3: Examples of a subcritical saturated (a), subcritical and slightly superheated (b), and supercritical (c) ORC process in a T,s-diagram.

2.2 Literature review

The most common ORC applications, most relevant studies on ORC working fluids, cycle configuration options, and the special features related to the design of ORC turbomachinery are presented and discussed in this section based on a literature review on the ORC technology.

2.2.1 Applications

Probably the first commercial ORC applications were designed for remote power stations (Bronicki, 1988) in the 1960s. These units were based on high speed turbogenerators having a power output of only a few kW (Bronicki, 1988). Following the small power stations, large-scale geothermal power plants using organic fluids were becoming more popular and commercially successful, and currently there are about 1000 MW installed geothermal power based on ORC technology or on a combination of ORC and steam process (Bronicki, 2008). In the recent years, the largest number of installed ORC power plants have been biomass power plants, having a power output in a range from 0.5 MW to 2.5 MW, and in Europe, over 100 biomass ORC power plants are currently operating (Bini et al., 2010). Combined heat and power (CHP) plants are common solutions in biomass ORC applications (Bini and Manciana, 1996). Based on the reviews on ORC technology carried out by Tchanche et al. (2011) and Schuster et al. (2009), biomass and geothermal power plants are the most commercially mature ORC applications. Other potential ORC applications can be found in the solar power (Tchanche et al., 2011) and waste heat recovery applications, such as the heat recovery of gas turbines (Invernizzi et al., 2007; Chacartegui et al., 2009) and reciprocating engines (Bombarda et al., 2010; Vaja and Gambrotta, 2010) as well as the waste heat recovery in the energy intensive oil and gas, steel, cement, and glass industry (Campana et al., 2013). The relevant literature related to the waste heat recovery of gas turbines and reciprocating engines will be discussed in more detail later in this section.

More novel applications implementing ORC technology can also be identified. Angelino and Invernizzi (1993) studied the possibility of using the ORC technology in space power cycles. Angelino and Colonna (2000a and 2000b) studied and discussed the use of ORCs in recovering the waste heat of molten carbonate fuel cells. Khristenko (1961) studied the possibility of using organic fluids as the working fluid in nuclear reactors. Another interesting idea, which has been studied more recently, is related to the ocean thermal energy conversion (Straatman and van Sark, 2008; Bombarda et al., 2013; Yang and Yeh, 2014). The system working principle is based on the utilization of the temperature gradient between the ocean surface and bottom to produce electricity by means of a Rankine cycle. This type of power system can be identified as a source of clean energy, but on the other hand, the system represents a very low electric efficiency, due to the small temperature difference between the heat sink and the heat source (Tchanche et al., 2011). In addition, recently published research papers by Bracco et al. (2013) and Qui et al. (2012) show increasing interest towards the use of small-scale ORCs as domestic power units. The use of micro-scale Rankine cycles in utilizing the exhaust gas and the heat from the engine cooling system in automotive applications, such as heavy duty trucks, has been recently studied, and different technical solutions, working fluids, and cycle configurations have been suggested(Wang et al., 2011; Seher at al., 2012; Lang et al., 2013; Sprouse and Depcik, 2013).

2.2.2 Working fluid selection and process design considerations

Several studies have been carried out to study the use of different working fluids and optimal working parameters for different ORC applications. Hung et al. (1997) studied several working fluid candidates for recovering waste heat. They concluded that the shape of the saturation vapor curve of the fluid has a large effect on the system design and performance. They also concluded that the cycle efficiency is a weak function of the turbine inlet temperature, but an increase of superheating at the turbine inlet will not result in a significant increase in the cycle efficiency in all the cases. Saleh et al. (2007) studied the use of 31 working fluids for low-temperature organic Rankine cycles including alkanes, fluorinated alkanes, ethers, and fluorinated ethers. They studied the use of different working fluids in a low-temperature application, concentrating on temperature levels typical to geothermal heat power plants, and the maximum temperature of the working fluid was limited to 100 ^{o}C in their study. Both subcritical and supercritical pressure level processes were studied. They concluded that when using fluids having a dry expansion, a decrease in the process thermal efficiency can be observed by superheating the fluid.

Liu et al. (2004) studied the influence of using different working fluids in ORCs. Their results showed that the cycle thermal efficiency for various working fluids is a weak function of the critical temperature of the fluid and the use of fluids having a hydrogen bond in certain molecules, such as water, ammonia, and ethanol, results in a wet expansion and are regarded as inappropriate for ORC systems. Chen et al. (2010) studied 35 working fluids, including wet, isentropic, and dry fluids for ORCs including supercritical cycles. They concluded that the selection of working fluid has a significant impact on the obtainable cycle performance, and their study indicated that the fluids categorized as isentropic or dry are preferred in ORCs. According to their study, the working fluids can be evaluated based on several criteria, such as the thermodynamic and physical properties, stability and compatibility, environmental impacts, safety, and availability, as well as cost. Their conclusion was that no single fluid could be identified that would meet all the discussed criteria for cycles utilizing different heat sources with different temperature levels.

Angelino and Colonna (1998) studied the use of siloxane mixtures as working fluids in ORCs. They concluded that by using a working fluid mixture instead of single fluid the working fluid can be better matched to the heat source in the evaporator and to the heat sink in the condenser because of the non-isothermal phase change. Schuster et al. (2010) carried out a study on supercritical ORCs. Their results showed that by using supercritical fluid conditions a higher cycle efficiency can be obtained when compared to a subcritical cycle. Karellas et al. (2012) studied the design of heat exchangers for supercritical ORCs. They presented a method to calculate and design heat exchangers for supercritical fluid conditions and concluded that experimental studies are necessary to validate the presented method because the heat transfer mechanisms with fluid conditions near the critical point are relatively unknown.

Quoilin et al. (2011) studied both the thermodynamic and economic optimization of a

small-scale ORC for an application recovering waste heat. The studied working fluids were R245fa, R123, n-butane, n-pentane, R1234yf, and Solkatherm. Their results showed that using different objective functions, mainly optimizing with respect to the economics or cycle thermodynamic efficiency, will lead to different optimal working conditions for the same fluid. They concluded that a thermodynamic optimization can give a good idea of the best working fluids for the application, but the thermodynamic optimization will not necessarily lead to the selection of the optimal working fluid in terms of economics. Madhava Hettiarachi et al. (2007) studied the use of ammonia, HCFC123, n-pentane, and PF5050 as potential working fluids for a geothermal application. They suggested a design criteria based on the ratio of heat transfer area needed in the process to the net power produced since they suggest that this ratio can be used as a suitable measure in evaluating the total power plant cost. Their results show that the selection of working fluid has a significant impact, not only on the power output but also on the power plant cost. Branchini et al. (2013) presented six ORC performance indexes that they suggested being beneficial when designing ORC systems. The presented performance indexes were namely the ORC cycle efficiency, ORC specific work, volumetric expansion ratio over the turbine, ORC working fluid to heat source fluid mass flow ratio, and recovery efficiency, as well as the heat exchanger surfaces of the ORC. They suggested that these indexes could be used in the design of ORC processes in terms of both the performance and economics.

One interesting working fluid group can be identified as siloxanes. Fernandez et al. (2011) studied the use of siloxanes in high-temperature ORC applications. The analysis included saturated and superheated, subcritical, and supercritical cycles adopting linear and cyclic siloxanes as the working fluids. They concluded that the simple linear siloxanes MM (hexamethyldisiloxane, $C_6H_{18}OSi_2$) and MDM (octamethyltrisiloxane, $C_8H_{24}O_2Si_3$) show high efficiencies and ensure the thermal stability of the working fluid in the saturated and regenerative cycles. They also concluded that the low condensing pressure, when using siloxanes D_5 (decamethylcyclopentasiloxane, $C_{10}H_{30}O_5Si_5$), D_6 (dodecamethylcyclohexasiloxane, $C_{12}H_{36}Si_6O_6$), and MD_2M (decamethyltetrasiloxane, $C_{10}H_{30}O_3Si_4$), makes these fluids more suitable in cycles having high condensing temperatures. In most of the biomass ORC processes, siloxane MDM is used as the working fluid (Drescher and Brüggeman, 2007). The use of siloxanes as working fluids have also been considered in several studies for different applications including space power cycles (Angelino and Invernizzi, 1993), the heat recovery in molten carbonate fuel cells (Angelino and Colonna, 2000a; Angelino and Colonna, 2000b) and the exhaust gas heat recovery from micro-gas turbines (Invernizzi et al., 2007).

Despite a large number of studies concerning the working fluid selection for ORC cycles, no single fluid can be identified as the most suitable one for all the ORC applications. The working fluid selection is highly dependent on the considered application, power scale, heat source temperature level, and the heat sink temperature level. The objective of the optimization can result in the selection of different optimal fluids depending on whether the fluid selection is based on maximizing the cycle power output, environmental considerations, or economics.

2.2.3 Studies on waste heat recovery by means of ORC from diesel and gas engines and gas turbines

Sprouse III and Depcik (2013) reviewed the literature related to studies on heat recovery of diesel engines by means of Rankine cycles. They summarized that the Rankine processes using steam or organic fluids have been more attractive in the waste heat recovery applications when compared to the Brayton, Stirling, Kalina, and supercritical CO_2 cycles because the Rankine cycles are relatively simple, representing comparably high efficiency and low component costs. They concluded that the high fuel prices and concerns about the environmental impacts led to the first studies on using the ORC technology in improving the energy efficiency in cars and long haul trucks. They also concluded that the recently published research papers, sponsored by large companies, are showing a renewed interest towards the use of this type of waste heat recovery systems(Sprouse III and Depcik, 2013).

Angelino and Moroni (1973) made one of the first studies on recovering waste heat of different prime movers. They concluded that by using an organic fluid instead of steam, a larger amount of heat can be extracted to the waste heat process when a relatively low-temperature exhaust gas stream is used as the heat source. They estimated that by using the ORC as a bottoming cycle it is possible to generate 12 % additional power, and their results showed that the combined cycle efficiencies around 47 % could be achieved from low-speed diesel engine when a waste heat recovery system was added.

More recent studies on utilizing waste heat from large-scale engines have been carried out by Bombarda et al. (2010) as well as by Vaja and Gambrotta (2010). These studies have concentrated mainly on the utilization of the exhaust gas heat. Bombarda et al. (2010) carried out a study comparing ORC and Kalina processes utilizing exhaust gas heat streams from two 8.9 MW diesel engines. Their results showed that the ORC technology has certain advantages in this kind of applications due to lower pressure levels, simpler turbine, and less corrosive fluids when compared to Kalina cycles. The thermodynamic efficiencies of the Kalina and ORC processes obtained from the simulations were comparably similar. The electrical power produced using the Kalina cycle was 1615 kW, while using the ORC, a power output of 1603 kW was achieved. The electrical efficiency of the studied diesel engine was 46.0 % without a bottoming cycle, and the electrical efficiencies of 50.2 % and 50.1 % were obtained when using the Kalina cycle and the ORC as the bottoming cycle, respectively. The working fluid used in the ORC was siloxane MM, and a recuperator was used. According to their study, also the heat streams from jacket cooling water, charge air, and lube oil system are available, but no further analysis utilizing these low-temperature heat sources was conducted. The waste heat recovery from a natural gas-fired medium-speed engine was studied by Vaja and Gambrotta (2010). The electrical power of the studied engine was 3 MW, the exhaust gas temperature was about 470 °C, and the rated electrical efficiency of the studied engine was 41.8 %. It was evaluated that there was a capacity of 1700 kW available by cooling the exhaust gases to 120 °C and approximately 1000 kW from the engine cooling water. Three different ORC cycle configurations were adopted to utilize the waste heat streams. First, using a

simple ORC cycle utilizing exhaust gases only; second, using a simple ORC cycle with the engine cooling water implemented to preheat the organic fluid; and third, using an ORC cycle with a recuperator utilizing exhaust gases only. Also three different working mediums were studied; namely benzene, R11, and R134a. They concluded that it was possible to achieve a significant efficiency increase using the ORC as a bottoming cycle. The highest electrical efficiency, 47.1 %, was achieved using benzene as a working fluid, and using the ORC cycle with a recuperator or the ORC cycle with preheating. Another conclusion was that the use of preheating leads to a simpler heat exchanger compared to the use of a recuperator.

The waste heat recovery in small-scale engines has been studied recently as well. Wang et al. (2012) studied a dual-loop ORC process having two waste heat recovery cycles. The studied engine was a four stroke gasoline engine having a power output of 130 kW. First, using the exhaust gas heat in high temperature ORC loop using R245fa as working fluid, and second, utilizing the low-temperature heat of the engine coolant by using R134a as the working fluid. Their results indicated that 9.6 kW net power output was obtained from the exhaust gas heat and 26.4 kW was obtained from the engine cooling system. Srinivasan et al. (2010) studied the exhaust gas heat recovery using ORC. They used test data available from a 1-cylinder dual-fuel test engine where supercharging was simulated using compressed air and exhaust gas pressure regulation. A simple ORC cycle (without a recuperator) was studied using R11 as a working fluid. Simulations were performed using different injection timing and exhaust gas recirculation levels, and an average of 20 % increase on the total power output was noticed when using the ORC. Seher et al. (2012) presented a study on the exhaust gas heat recovery system for commercial vehicles and considered the potential working fluids and expander types. Both the production of the mechanical power and the electrical power were considered, and an experimental study was conducted for a system having a piston expander and for a system having a turbine. Based on their results they concluded that the most favorable system consists a piston expander using water or ethanol as the working fluid or a turbine using ethanol as the working fluid. They considered the use of siloxane MM, toluene, and R245fa as unfeasible in the system when using a piston expander because the volumetric flow rate of these fluids is high and would lead to a large sized and low efficiency piston expander.

Waste heat recovery of high efficiency gas turbines by means of ORCs was studied by Chacartegui et al. (2009), and their results showed that the ORC technology is a potential technology in utilizing the exhaust gas heat from gas turbines, especially if the exhaust gas temperature is relatively low. They considered toluene and cyclohexane as the most potential fluids based on the obtained cycle efficiency. The study estimated that this type of combined cycle would be economically interesting for medium- and large-scale power plants if the capital cost of gas turbine would be under 350 €/kW and the capital costs of ORC system would be under 2000 €/kW. Waste heat recovery from a micro-scale gas turbine was studied by Invernizzi et al. (2007). The electric power output of the studied micro gas turbine was 100 kW, and the exhaust gas temperature level was in range from 250 °C to 300 °C. Several fluids were considered, including siloxanes and hydrocarbons.

They noticed that the thermodynamic efficiency of the ORC increased as the molecular complexity of the working fluid increased, but on the other hand, the higher molecular complexity led to higher exhaust gas outlet temperatures, and thus, a lower amount of heat could be extracted from the heat source. Therefore, it was recommended to use working fluids with a rather low molecular complexity. Invernizzi et al. (2007) also discussed the preliminary design of an ORC turbine for the heat recovery application. The designed turbine was a 40 kW two-stage axial turbine, and hexamethyldisiloxane (MM) was used as the working fluid. It was also roughly estimated in their study that by adding the ORC as a bottoming cycle, the specific cost of the system increased from 1200 €/kW to 1600 - 1800 €/kW when the specific cost of the ORC was estimated to be in the range from 2500 €/kW to 3000 €/kW.

2.2.4 Studies on micro-scale ORC power cycles

The interest towards small-scale ORC systems has been increasing in the recent years. Wang et al. (2011) carried out a study on a 10 kW ORC system having a screw expander and designed for a waste heat recovery application. They considered eight different fluorocarbons and butane as potential working fluid candidates. Based on their study, R245fa and R245ca were considered as the most suitable working fluids for the studied systems, if in addition to the cycle performance, safety aspects as well as environmental issues are considered. They estimated the ORC system cost based on existing air conditioning systems and relevant engine components of a passenger car and concluded that a specific price of less than 100€/kW can be achieved in a case of mass production and a simple cycle configuration. Leibowitz et al. (2006) discussed the use of screw expanders in small scale ORCs having a power output in the range from 20 kW to 50 kW. They suggested that the use of screw expanders can bring certain benefits when compared to small scale turbines, such as lower rotational speed, the availability of directly coupling the expander into a generator, as well as a higher efficiency in small scale applications. They also concluded that the specific price of the commercial system would be in the range from 1500 $/kW to 2000 $/kW.

Kang (2012) carried out an experimental study on an ORC having a high speed radial turbine and high speed generator coupled directly into one shaft without a gear box and having a rotational speed of 63 000 rpm. The system used refrigerant R245fa as working fluid, and the evaporation temperature of the working fluid was in the range from 70 ^{o}C to 90 ^{o}C. The measured power output of the system was 32.7 kW, and the achieved turbine efficiency of 78.7 % was rather high for a small-scale ORC system. More recently, Borsukiewicz-Gozdur (2013) and Klonowicz et al. (2014) carried out an experimental study on a small-scale ORC system using refrigerant R227ea as the working fluid, and the system utilized low-temperature district heating water as a heat source. The system included a hermetic turbogenerator having a power output of 9 kW-10 kW and the designed turbine was a partial admission axial turbine. Based on the measurements, the electric efficiency of the turbogenerator of less than 60 % was achieved including the losses in the turbine and in the generator.

Qiu et al. (2012) carried out an experimental study aiming at designing a domestic-scale ORC process using biomass as a heat source and producing both thermal power and electricity. They used HFE7000 and HFE7100 as working fluids in the experimental setup and the process expander was modified from a vane type compressor. The system produced 900 W electric power and 47 kW of thermal power showing a CHP efficiency of 78.7 %. The main reasons for the low electric power output were the low efficiency of the expander, alternator, and boiler, and the large losses in the other process components. More recently, Brocco et. al (2013) carried out an experimental study on a small-scale ORC for domestic power production. The working fluid was R245fa, and the system had a scroll expander, which was derived from a commercial compressor, and an electric boiler was used instead of an external heat source to evaporate the liquid. The system reached a global electric efficiency of 8 % despite the fact that most of the process components were not optimized.

2.2.5 Special features of ORC turbines

In this study, ORC processes adopting turbines are mainly considered. The low enthalpy drop over the turbine and a large volumetric flow rate at the turbine outlet enable the use of turbines with relatively simple geometries when compared to conventional steam turbines (Macchi, 1977; Verneau, 1987; Larjola, 1995). Another advantage is that the most of the organic fluids remain at superheated state along the expansion, and therefore, there is no risk of liquid drops damaging the turbine (Liu et al., 2004). The turbines used in the existing ORC power systems are typically axial turbines (Jokinen et al., 1998; Colonna et al., 2006a) or radial inflow turbines (Larjola, 1995; van Buijtenen et al., 2003; Kang, 2012). Studies on the possibility of using multistage radial outflow turbines have been carried out recently, for example by Pini et al. (2013) since the multistage radial outflow arrangement allows to have lower rotational speeds when compared to the conventional axial and radial inflow flow arrangements. Another advantage related to the use of radial outflow arrangement is that the flow remains subsonic if a large number of turbine stages are adopted and large pressure ratios over the turbine can be achieved (Pini et al., 2013).

Macchi and Perdichizzi (1981) carried out a study on the design principles of axial turbine stage when nonconventional working fluids are adopted. They proposed that the efficiency of the turbine stage can be predicted based on three parameters, namely the ratio of volumetric flow rate at the inlet and outlet of the turbine, which takes into account the compressibility effects, the relation between the volumetric flow at the turbine outlet and isentropic enthalpy change in the turbine, $\sqrt{q_{v,out}}/\Delta h_s^{1/4}$, which takes into account the actual turbine dimensions, and the turbine specific speed N_s. Their results indicated that the effects of compressibility become very important for stages having a high pressure ratio and the stage efficiencies are low when adopting high pressure ratios. The turbine volumetric flow rate ratio between the outlet and inlet of the turbine can vary largely, depending on the selected fluid and the temperature level. According to Macchi (1977), values for volumetric flow rate ratio as low as five can be found in low-temperature ORC

applications and values as high as 200-300 can be found in high-temperature ORC applications. The two main difficulties related to turbines having high expansion ratios are the high relative Mach numbers at the turbine rotor inlet as well as large rotor blade height variations between the rotor inlet and outlet (Macchi, 1977). In ORC processes adopting high pressure ratio over a single turbine stage, zero reaction turbines are not feasible because of the large pressure ratio over the turbine stator, highly supersonic flow, and large relative Mach number at the turbine rotor inlet (Macchi, 1977). If 50% reaction turbines are considered, significant changes in the turbine rotor blade height and flow area are needed because of the large change in the volumetric flow rate from the turbine rotor inlet to rotor outlet (Macchi, 1977). Thus, the degree of reaction r is recommended to be $0 < r < 0.5$. The degree of reaction can be defined by dividing the isentropic enthalpy change in the turbine rotor by the total isentropic enthalpy change over the turbine stage.

Verneau (1987) presented experimental results for two 50 kW ORC turbines, using FC 75 as the working fluid. The total pressure ratio of the turbine was about 150, and the first design was a supersonic two-stage axial turbine. The second design was a single stage turbine having a pressure ratio of 150. Their test results showed that relatively high total to static efficiencies in the range from 70 % to 80 % were achieved for both the two-stage and single-stage turbine. The turbine design presented by van Buijtenen et al. (2003) showed reasonably good performance in test runs, despite the large pressure ratio of about 120 over a single-stage radial turbine.

In many ORC systems adopting turbines, despite the moderate flow velocities in turbine flow passages, the flow tends to be supersonic since most of the organic fluids are characterized by a low speed of sound. This leads to losses related to the occurrence of oblique shock waves and their reflections in the turbine flow passages (Hoffren et al., 2002; Colonna et al., 2006a; Harinck et al., 2010). Methods to improve the design of supersonic ORC stators have been developed in the recent years, for example by Harinck et al. (2013), presenting a turbine optimization method based on automated CFD design. Their results indicated that by bending and turning the stator flow channels the losses caused by the occurrence of oblique shock waves can be reduced significantly (Harinck et al., 2013).

One important parameter when designing turbine flow channels using organic fluids with high molecular complexity can be identified as the fundamental derivative of gas dynamics. The fundamental derivative of gas dynamics relates to the molecular complexity of the fluid and can be used to classify the gas dynamic behavior during the expansion (Harinck et al., 2009; Guardone et al., 2013). The fundamental derivative of gas dynamics is a quantitative measure of variation of the speed of sound to the specific volume in an isentropic expansion and can be defined as

$$\Gamma = 1 - \frac{v}{a}\left(\frac{\partial a}{\partial v}\right)_s. \tag{2.1}$$

Fluids having $\Gamma > 1$ and hence $(\partial a/\partial v)_s < 0$ in the vapor region can be classified as low

molecular complexity (LMC) fluids, which are made of molecularly simple molecules. For low molecular complexity fluids real-gas effects are limited to quantitative deviations with respect to ideal-gas fluid dynamics behavior. Fluids having $0 < \Gamma < 1$ in a finite thermodynamic region and hence $(\partial a/\partial v)_s > 0$ can be identified as high molecular complexity fluids (HMC). For HMC fluids also qualitative differences in fluid dynamics behavior can be observed in the real-gas region. Most notable is the increase in the speed of sound upon isentropic expansion, possibly leading to a local decrease in the Mach number, which instead increases monotonically for an isentropic ideal-gas expansion in the turbine (Harinck et al., 2009).

In the study by Colonna et al. (2006a) it was reported that when using molecularly complex working fluids, such as siloxane MDM, significant deviations when compared to ideal gas behaviour, including the increase in the speed of sound along the expansion, were noticed with reduced inlet pressure $p_{t,in}/p_{crit}$ = 0.56 and with reduced inlet temperature $T_{t,in}/T_{crit}$ = 0.95, especially at the first part of the expansion in a supersonic axial turbine stator. Thus, the design of ORC turbines requires the use of accurate thermodynamic models to predict the real gas effects of the flow, especially when adopting working fluids having a high molecular complexity or when the expansion occurs relatively close to the critical point of the fluid, in order to design turbines with a high efficiency and desired performance (Colonna et al., 2006a; Turunen-Saaresti et al., 2006; Harinck et al., 2010).

Despite several studies on the use of high-expansion ratio radial inflow turbines for ORC systems, general guidelines to design such expanders, especially for small power output systems, are lacking in the literature at the moment. In addition, only a few studies have been published presenting and discussing experimental results related to the operation and performance of high expansion ratio ORC turbines.

2.2.6 Conclusions and discussions based on the literature

Based on the literature review, the following conclusions were made:

• The most technologically mature ORC applications can be found in large-scale geothermal power plants and biomass power plants having the power range from 0.5 MW to 5 MW. In addition, the applications in the field of waste heat recovery have been commercially succesfull in a smaller scale.

• Several relatively new applications such as waste heat recovery in mobile applications and domestic scale ORCs have been studied recently.

• The working fluid selection and the achieved efficiency varies significantly depending on the selected application, power scale, temperature levels, cycle configuration, and the expander type.

• Despite several efforts aiming to identify the most suitable working fluids, no single working fluid can be identified as the best for all applications and temperature levels. Thus, a detailed working fluid selection study has to be carried out when designing new ORC systems for different applications.

• The working fluid selection and the cycle working parameters are highly affected by the selected objective function; in other words, whether the selection of working fluid and process design is based on maximising the system power output, maximising the economical profitability, optimizing the size of the process equipment, or on environmental considerations.

• Most of the small-scale ORC systems are designed for low-temperature applications, presenting low cycle efficiencies and small expansion ratios over the expander. Thus, a volumetric expander is considered in most of the cases.

• Only few studies have been published discussing the design of small-scale ORC turbines and presenting experimental results for high-expansion ratio ORC turbines.

2.3 ORC process based on high-speed turbogenerator technology

One interesting technical solution in the field of ORC technology is based on the use of high-speed turbogenerators. High-speed turbogenerator concept consists of a turbine, generator, and a feed pump coupled onto a single shaft having a high rotational speed of typically more than 10 000 rpm (Larjola, 1988; Larjola, 1995; van Buijtenen et al., 2003). A schematic process flow diagram of an ORC process based on high-speed technology is presented in Figure 2.4, and a cut-off of a typical high-speed turbogenerator is shown in Figure 2.5.

The advantages in using high-speed turbogenerators are the compact size, when compared to turbines having a low rotational speed and a gear box; no need for external lubrication circuit; availability for hermetic design; and the reliability of the turbogenerator system (Larjola, 1988; Larjola, 1995; van Buijtenen et al., 2003). A separate pre-feed pump can be added to the system to prevent cavitation at the inlet of the main feed pump, which is connected to the turbogenerator shaft.

Few prototypes based on this concept have been built and tested for heat recovery applications (Larjola, 1988; Larjola, 1995; van Buijtenen et al., 2003) and for recharge station of deep sea submersibles (Jokinen, 1998), as well as considered for distributed biomass power plants (Heinimö, 2004). A heat recovery unit having a power output of 160 kW and using toluene as working fluid has been successfully commercialized (van Buijtenen, 2009).

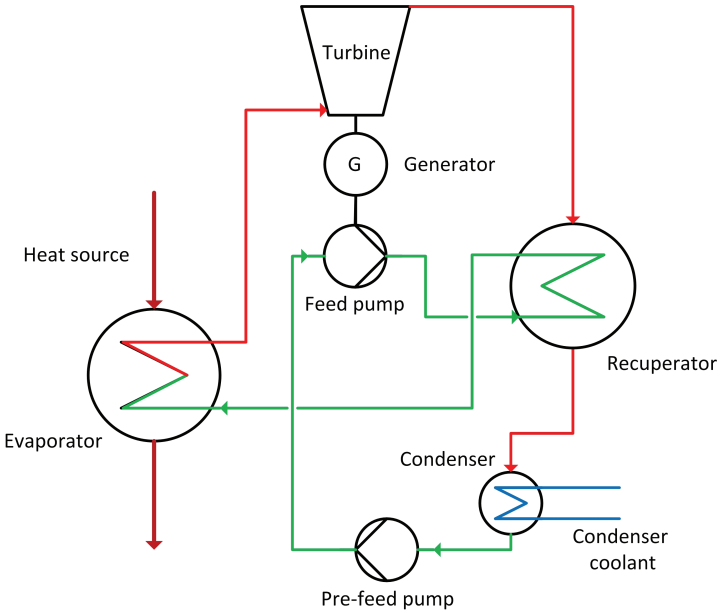

Figure 2.4: Schematic process flow diagram of an ORC process based on high-speed turbogenerator technology.

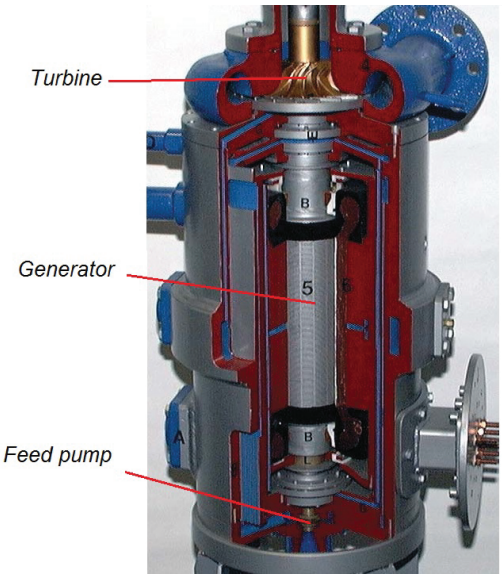

Figure 2.5: Cut-off of a typical high-speed turbogenerator.

3 Numerical methods

In this section, the numerical methods used in this thesis are presented. First, the methods and equations used in the process design and in the thermodynamic analysis are presented. Second, the turbine design method is described. Third, the numerical methods used in the computational fluid dynamics (CFD) are described.

3.1 Thermodynamic analysis and process design methods

The ORC process modelling and the thermodynamic analysis was based on the well-known calculation principles of a Rankine cycle. The thermodynamic and transport properties database Refprop (Lemmon et al., 2010) was used for determining the working fluid thermodynamic properties. The solved properties were temperature T, pressure p, specific enthalpy h, specific entropy s, density ρ, specific volume v, and speed of sound a. The process condensing temperature, heat source values, and the degree of superheating, as well as the process component efficiencies were used as an input for the computation. The evaporation pressure was used either as an input parameter or was optimized based on the heat source values. The saturated liquid and the saturated vapour thermodynamic state in the condenser and in the evaporator were determined based on the evaporation pressure and the condensing temperature. The parameters given as the input values in the process design are presented in Table 3.1. The unknown thermodynamic states were solved by using the equations of states implemented in Refprop in which two input properties are used to determine other thermodynamic properties in the same process node. The cycle power output, efficiency, thermodynamic states of the working fluid at the inlet and outlet of each component, and the saturated states inside process components, as well as the working fluid mass flow rate were obtained as a result of the simulation by solving the continuity and energy equation for each process component. The calculation procedure for solving the unknown thermodynamic properties in different process nodes is presented in Table 3.2.

Processes having subcritical evaporation pressures were studied, and thus, a limit for the evaporation pressure compared to the fluids critical pressure $p_{\mathrm{ev}}/p_{\mathrm{crit}}$ was used in the thermodynamic analysis. Another constraint used for optimizing the evaporation pressure was based on the minimum pinch-point temperature difference in the evaporator, ΔT_{pp}, which is the smallest temperature difference between the heat source and the working fluid. An example of the evaporator temperature diagram, presenting the definition and the location of a typical pinch-point temperature difference in the evaporator, is presented in Figure 3.1. In some of the simulations, the minimum temperature difference between the heat source and the working fluid occurred at the cold end of the evaporator, where the heat source exits the evaporator. A feature was added to the process design tool by using a simple linear search algorithm to optimize the evaporation pressure to reach the target minimum temperature difference in the evaporator with the given heat source values and given working fluid. A small degree of superheating was used in the simulations because a flow-through type evaporator was considered which requires superheating in the process

Table 3.1: Input parameters used in the process design.

Working fluid side	
working fluid	
evaporation pressure	p_{ev}
degree of superheating	ΔT_{sh}
condensing temperature	T_{c}
recuperator effectiveness	ε
pressure losses	
Heat source side	
heat source mass flow rate	$q_{\mathrm{m,hs}}$
heat source inlet temperature	$T_{\mathrm{hs,in}}$
heat source outlet temperature	$T_{\mathrm{hs,out}}$
heat source isobaric heat capacity	$\bar{c}_{\mathrm{p,hs}}$
Components	
turbine efficiency	η_{t}
generator and mechanical efficiency	η_{gm}
feed pump efficiency	η_{fp}
feed pump motor efficiency	$\eta_{\mathrm{fp,m}}$
miscalleneous power consumption	$P_{\mathrm{mis}}/P_{\mathrm{e}}$

Table 3.2: Calculation procedure for solving the unknown thermodynamic properties.

Process node	input	solved
Turbine inlet	p,T	h,s,v
Turbine outlet, isentropic	p,s	T,h
Turbine outlet	p,h	T,s,v
Recuperator inlet (vapor side)	p,T	h,s,v
Condenser inlet	p,T	h,s,v
Condenser (saturated vapor)	T	p,h,v
Condenser (saturated liquid)	T	p,h,v
Pump outlet	p,h	v
Evaporator inlet	p,h	T
Evaporator (saturated liquid)	p	T,h
Evaporator (saturated vapor)	p	T,h

to prevent liquid droplets entering the turbine (Talonpoika, 1996).

The heat rate extracted from the heat source to the ORC process was defined as

$$\phi_{\mathrm{ev}} = q_{\mathrm{m,hs}}(h_{\mathrm{hs,in}} - h_{\mathrm{hs,out}}) \approx q_{\mathrm{m,hs}}\bar{c}_{p,hs}(T_{\mathrm{hs,in}} - T_{\mathrm{hs,out}}). \tag{3.1}$$

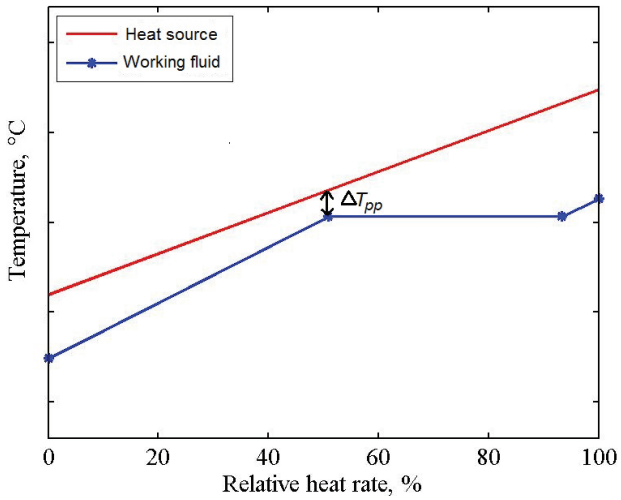

Figure 3.1: Example of an evaporator temperature diagram and the pinch-point temperature difference.

The working fluid mass flow rate is calculated by using the heat rate to the evaporator and the working fluid enthalpy at the evaporator inlet and outlet, and is defined as

$$q_{\mathrm{m,wf}} = \frac{\phi_{\mathrm{ev}}}{h_{\mathrm{ev,out}} - h_{\mathrm{ev,in}}}. \tag{3.2}$$

The turbine outlet state was defined by calculating the enthalpy after isentropic expansion and solving the enthalpy after the turbine $h_{\mathrm{t,out}}$ from the definition of turbine isentropic efficiency. The turbine isentropic efficiency is defined as

$$\eta_{\mathrm{t}} = \frac{h_{\mathrm{t,in}} - h_{\mathrm{t,out}}}{h_{\mathrm{t,in}} - h_{\mathrm{t,s,out}}}. \tag{3.3}$$

The turbine power is calculated as

$$P_{\mathrm{t}} = q_{\mathrm{m,wf}}(h_{\mathrm{t,in}} - h_{\mathrm{t,out}}). \tag{3.4}$$

A parameter recuperator effectiveness was used in evaluating the vapor temperature at the recuperator outlet. The recuperator effectiveness is defined as

$$\varepsilon = \frac{T_{\mathrm{v,in}} - T_{\mathrm{v,out}}}{T_{\mathrm{v,in}} - T_{\mathrm{l,in}}}. \tag{3.5}$$

When the vapor temperature at the recuperator outlet was solved, the liquid state at the recuperator outlet was calculated by using the energy balance of the recuperator. It should

be noticed that this simplified calculation approach for the recuperator effectiveness is based only on the use of temperatures and does not take into account the possible significant changes in the heat capacity on the vapor side, which should be taken into account in a more detailed design of the recuperator.

The enthalpy change in the feed pump can be defined as

$$\Delta h_{\mathrm{fp}} = \frac{v(p_{\mathrm{fp,out}} - p_{\mathrm{fp,in}})}{\eta_{\mathrm{fp}}}. \tag{3.6}$$

The feed pump power is defined as

$$P_{\mathrm{fp}} = q_{\mathrm{m,wf}} \frac{v(p_{\mathrm{fp,out}} - p_{\mathrm{fp,in}})}{\eta_{\mathrm{fp}}}. \tag{3.7}$$

The temperature rise in the feed pump can be defined as

$$\Delta T_{\mathrm{fp}} = (1 - \eta_{\mathrm{fp}}) \frac{h_{\mathrm{fp,out}} - h_{\mathrm{fp,in}}}{c_{\mathrm{p}}}. \tag{3.8}$$

The net electric power from the system can be calculated as

$$P_{\mathrm{e,net}} = (P_{\mathrm{t}} - P_{\mathrm{fp}})\eta_{\mathrm{gm}} - P_{\mathrm{mis}}, \tag{3.9}$$

if the feed pump is located on a turbine shaft.

The net electric efficiency of the ORC process was defined by dividing the net electric power output by the evaporator heat rate

$$\eta_{\mathrm{e,net}} = \frac{P_{\mathrm{e,net}}}{\phi_{\mathrm{ev}}}. \tag{3.10}$$

The pressure losses between the turbine and condenser were estimated in the simulations presented in Chapter 5. The pressure loss was estimated based on the turbine outlet velocity and working fluid density at the turbine outlet. The pressure loss after the turbine depends mostly on the flow velocity. The pressure loss between the turbine outlet and the condenser is estimated by

$$\Delta p_{\mathrm{pl}} = 0.5 \rho_{\mathrm{t,out}} c_{\mathrm{t,out}}^2 C_{\mathrm{d}}. \tag{3.11}$$

The drag coefficient C_{d} in Equation 3.11, is estimated based on the experience gained from measurements in a larger-scale commercial ORC power plant. It should be noted that an accurate estimation for the pressure losses would require detailed information about the geometry of the components, pipeline lengths, and the size of the flow passages.

In the simulations presented in Section 7.1, the obtained electric power output from the ORC was compared to the theoretical heat transfer areas needed in the processes by using a ratio $A_{tot}/P_{e,net}$ to make a simplified evaluation on the feasibility of the process with different fluids and operational parameters. The theoretical heat transfer areas required in different processes were evaluated based on the temperature profiles of the heat exchangers. The evaluation of theoretical heat transfer areas were based on the log mean temperature difference in the heat exchangers and estimated overall heat transfer coefficients. The overall heat transfer coefficients used in the analysis for organic fluids were evaluated either based on reference (VDI, 1988) or values obtained from heat exchanger manufacturers. The theoretical heat transfer area was defined as

$$A = \frac{\phi}{U \Delta T_{\mathrm{LMTD}}}. \tag{3.12}$$

The logarithmic temperature difference can be defined as

$$\Delta T_{\mathrm{LMTD}} = \frac{\Delta T_{\mathrm{in}} - \Delta T_{\mathrm{out}}}{ln \frac{\Delta T_{\mathrm{in}}}{\Delta T_{\mathrm{out}}}}. \tag{3.13}$$

The total theoretical heat transfer area is defined as

$$A_{\mathrm{tot}} = A_{\mathrm{ev}} + A_{\mathrm{co}} + A_{\mathrm{re}}. \tag{3.14}$$

The used heat tranfer coefficients are presented in Table 3.3.

Table 3.3: Overall heat transfer coefficients.

Heat exchanger	U [W/m^{2}K]
evaporator:	
organic fluid - heat source	20
recuperator:	
organic vapor - organic liquid	40
condenser:	
organic vapor - liquid cooling fluid (desuperheating)	60
condensing organic vapor - liquid cooling fluid	900

3.2 Turbine design methods

The turbine design method used in this thesis is presented in the following. The turbine 1-D design was performed with an ORC turbine design tool developed at LUT. The calculation application calculates the main dimensions and velocity triangles of the turbine. The turbine type selected in this work is a radial inflow turbine because radial inflow turbines represent a relatively simple geometry with single stage and can be designed to

operate with high pressure ratios over a single turbine stage. In addition, radial turbines have been proven successful in small-scale high speed ORC turbogenerator prototypes, designed and tested at LUT. The turbine inlet and the outlet conditions were obtained as a result from the process design, presented more in detail in the previous section. The preliminary evaluation of the turbine rotational speed, n is carried out by using the nondimensional parameter, turbine specific speed N_s defined as

$$N_s = \frac{\omega {q_{v,out}}^{0.5}}{{\Delta h_s}^{0.75}} \tag{3.15}$$

where the ω is the angular speed. The angular speed is defined as,

$$\omega = 2\pi n. \tag{3.16}$$

According to the performance diagram for radial turbines operating with compressible fluids, presented by Balje (1981), the highest efficiencies are obtained with a specific speed in the range from 0.4 to 0.8. Another nondimensional design parameter, specific diameter D_s, defined as

$$D_s = \frac{D{\Delta h_s}^{1/4}}{{q_{v,out}}^{0.5}} \tag{3.17}$$

, was used in evaluating the turbine rotor diameter. According to the diagram by Balje (1981), the highest efficiencies are obtained with a specific diameter in the range from 2 to 6.

The input parameters used in the turbine design are presented in Table 3.4. The ratio of

Table 3.4: Input parameters used in the turbine design.

total inlet pressure	$p_{\mathrm{tot,in}}$
total inlet temperature	$T_{\mathrm{tot,in}}$
working fluid mass flow rate	$q_{\mathrm{m,wf}}$
static pressure at stator outlet	$p_{\mathrm{st,out}}$
total pressure at rotor outlet	$p_{\mathrm{rot,out}}$
ratio of rotor diameters	$D_{2,\mathrm{t}}/D_1$
ratio of rotor outlet diameters	$D_{2,\mathrm{h}}/D_{2,\mathrm{t}}$
stator efficiency prediction	η_{st}
turbine efficiency prediction	η_{t}
stator exit flow angle or blade height	α_1 or t_1
specific speed or turbine rotational speed	N_s or n

diameters at the rotor inlet and rotor outlet D_{2t}/D_1, the ratio of the blade tip and hub diameters D_{2h}/D_{2tip} at the rotor outlet, as well as the suitable stator exit flow angle α_1 were determined by following the design guidelines presented by Rohlik (1975) and by monitoring the velocity triangles and blade heights at the inlet and at the outlet of the

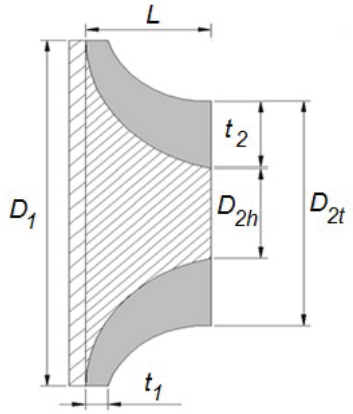

Figure 3.2: Schematic example of radial turbine rotor dimensions.

rotor. An example of radial turbine rotor dimensions and the used indexes are presented in Figure 3.2, while Figure 3.3 presents an example of a supersonic ORC stator, in which the flow channel consists of three main parts: a convergent section, a throat section, and a divergent section.

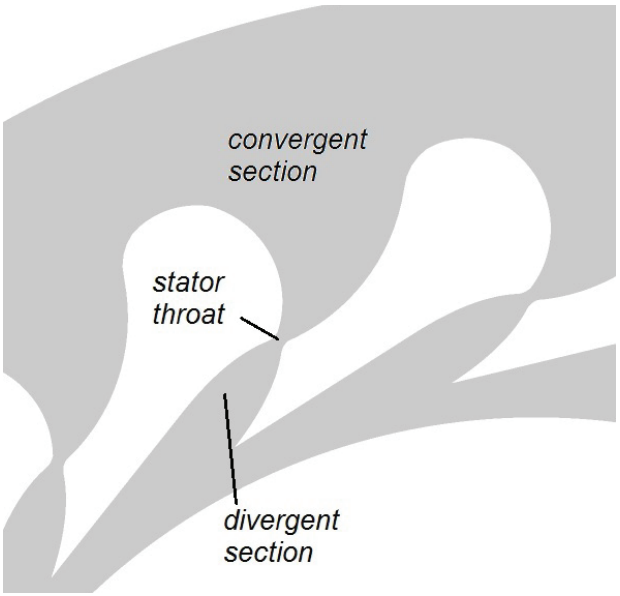

Figure 3.3: Example of a supersonic ORC turbine stator flow channel.

Velocity calculations were based on the continuity equation and on the Euler's equation. The velocity vectors were solved at the turbine stator outlet and at the rotor outlet. The

solved velocity vectors are the absolute velocity $\vec{c}$, relative velocity $\vec{w}$, and the peripheral velocity $\vec{u}$. The sum of velocity vectors $\vec{w}$ and $\vec{u}$ forms the absolute velocity vector $\vec{c}$

$$\vec{c} = \vec{w} + \vec{u}. \tag{3.18}$$

The tangential component of the absolute velocity $\vec{c_u}$ was used in monitoring the shape of the velocity triangle at the rotor inlet by using a velocity ratio c_u/u while the radial component of the absolute velocity $\vec{c_r}$ was used in the continuity equation. Examples of velocity triangles at the rotor inlet are presented in Figure 3.4a and Figure 3.4b and at the

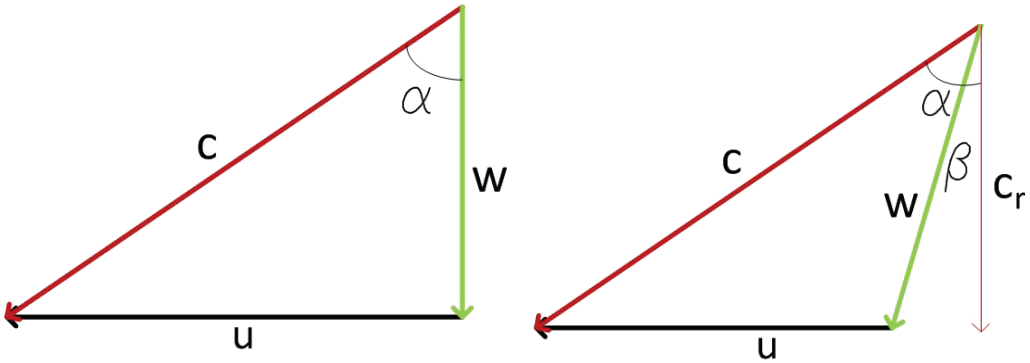

(a) (b)

Figure 3.4: Examples of velocity triangles at the turbine stator outlet (a) having a relative flow angle β_1=0 and (b) having a relative flow angle β_1 >0.

outlet of the turbine rotor in Figure 3.5. The velocity triangle at the outlet was calculated at the mean line of the blade and at the blade hub and shroud in order to determine the blade setting angles at the rotor outlet.

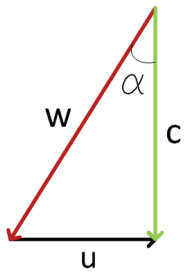

Figure 3.5: Example of a radial turbine rotor outlet velocity triangle.

If the velocity triangle at the turbine rotor inlet is as presented in Figure 3.4a, straight blades at the rotor inlet can be used because the angle of the relative velocity is β_1=0. If

the velocity at the rotor inlet is as presented in Figure 3.4b and the angle of relative velocity β_1 >0, curved blades can be considered at the rotor inlet to prevent flow separation at the rotor inlet caused by the high incidence angle. Examples of straight and curved rotor blades are presented in Figure 3.6a and Figure 3.6b.

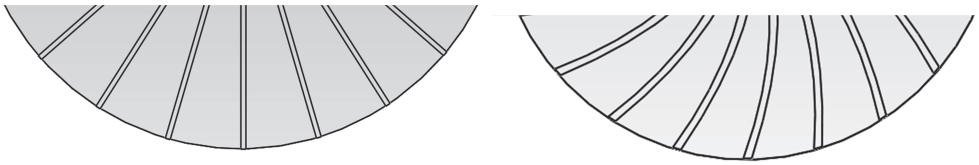

(a) (b)

Figure 3.6: Examples of turbine inlet (a) with straight blades and (b) with curved blades.

A suitable static pressure at the stator outlet was selected by using the definition of the degree of reaction, which can be defined by dividing the isentropic enthalpy change in the turbine rotor by the total isentropic enthalpy change in the turbine

$$r = \frac{\Delta h_{s,rot}}{\Delta h_{s,tot}}. \tag{3.19}$$

The absolute flow velocity c_1 at the stator outlet was solved from the estimated enthalpy change between the stator inlet and stator outlet by using the equation

$$c_1 = \sqrt{2(h_{\mathrm{tot,in}} - h_{1,\mathrm{st}})}. \tag{3.20}$$

The stator outlet enthalpy, $h_{1,st}$ was solved by using the turbine inlet enthalpy and the estimated total-to-static state efficiency of the stator

$$h_{1,\mathrm{st}} = h_{\mathrm{tot,in}} - \eta_{\mathrm{st}}(h_{\mathrm{tot,in}} - h_{1\mathrm{s,st}}). \tag{3.21}$$

The turbine power was determined from the velocity triangles based on the Euler's equation

$$P_{\mathrm{t}} = q_m(c_{\mathrm{u1}}u_1 - c_{\mathrm{u2}}u_2). \tag{3.22}$$

The turbines were designed to have the rotor outlet flow exiting in the axial direction, and thus, the velocity vector c_{u2} = 0. The peripheral velocity u_1 was calculated by using the equation

$$u_1 = \Delta h_t / c_{u1}. \tag{3.23}$$

The turbine diameter can be solved when the peripheral velocity and the rotational speed of the turbine are known by using the equation

$$D_1 = u_1/(\pi n). \tag{3.24}$$

The rotor inlet blade height was solved by using the equation

$$t_1 = \frac{q_{\mathrm{m,wf}}}{\rho_1 \pi D_1 c_{\mathrm{r1}}}. \tag{3.25}$$

Diameter ratios D_{2t}/D_1 and D_{2h}/D_{2t} were given as inputs, and the rotor outlet diameters at the blade hub and tip as well as the blade height at the rotor outlet were calculated by using the diameter ratios. The axial outlet velocity c_2 was solved as

$$c_2 = \frac{q_{\mathrm{m,wf}}}{\rho_2(\pi r_{2t}^2 - \pi r_{2h}^2)}. \tag{3.26}$$

In this thesis, two approaches to design the diverging section of the supersonic stator nozzles were used. Most of the studied stator nozzle diverging section geometries were designed by using the throat width and the exit flow area of the nozzle, based on the result of 1D-turbine design, and the method of characteristics was not used in these designs. One of the studied nozzle diverging section geometries was designed by using a nozzle design tool developed at Politecnico Di Milano employing the method of characteristics, which was extended to real gas flows according to Zucrow and Hoffman (1977). In this design method, the transonic potential equation was solved in the throat section by means of the approximate solution procedure of Sauer (1947), which is applicable to real gas flows without significant modifications. The transonic flow solution provides the initial data curve for the method of characteristic. The expansion through the divergent section to the designed exit pressure is achieved via an initial circular profile followed by the so-called turning region, in which the nozzle upper wall geometry is determined by imposing the conservation of the mass flow at each section.

When comparing the nozzle geometries obtained from a design based on a real gas model or ideal gas assumption, a large difference can be observed in the nozzle length and width, especially if the expansion process occurs in a thermodynamic region in which the fundamental derivative of gas dynamics Γ is always lower than the corresponding perfect gas value (Guardone, 2013). The perfect gas assumption leads to a shorter nozzle and smaller exit flow area when compared to the design based on real gas models. The nozzle length and the nozzle exit flow area are found to increase with the increasing molecular complexity of the fluid, due to the non-ideal dependence of the speed of sound on density along the isentropic expansion with organic fluids (Guardone, 2013). The nozzle design method has been used in previous works for designing an organic vapor wind tunnel (Guardone, 2013) and supercritical CO_2 nozzles (Guardone, 2010). The nozzle divergent section geometry is designed by giving the total state of the fluid at the turbine inlet and the nozzle throat width as the input values. The design method based on the method of characteristics results in a minimum-length nozzle, in which the desired nozzle outlet pressure and uniform Mach number distribution are achieved at the nozzle outlet.

The design of the turbine for the experimental ORC setup was an iterative process in which the turbine design, efficiency prediction, and the geometry were changed, based

on the flow field predicted by the CFD simulations as well as on the changes made in the process design. The constraints that were used in the radial turbine design for the experimental setup in evaluating feasible turbine dimensions and working parameters are listed in Table 3.5. The relative velocity at the turbine rotor inlet was limited to be subsonic to reduce the losses related to the supersonic flow as well as to simplify the rotor design. In addition, a subsonic absolute velocity was designed at the turbine rotor outlet to reduce the losses. The stator throat width was designed to be more than 1 mm and the blade height at the rotor inlet and in the stator flow channel was designed to be more than 1.5 mm because smaller dimension were estimated to lead in difficulties in manufacturing the turbine wheel and stator flow channels as well as to low turbine efficiency.

Table 3.5: Constraints used in the design of radial turbine for the ORC prototype.

$b_{st} > 1$ mm
$Ma_{\mathrm{w1}} < 1$
$t_1 > 1.5$ mm
$Ma_{c2} < 1$

3.3 Computational fluid dynamics

The turbine CFD simulations presented in this study were performed for a small-scale, high expansion ratio radial turbine that was designed for an experimental setup. The CFD simulations were carried out by using the Navier-Stokes flow solver Finflo, which is a multi-grid solver developed at the Aalto University School of Science and Technology, and some modifications and additions have been implemented to the code at the Lappeenranta University of Technology. More detailed information about Finflo and different numerical methods can be found for example in a paper of Siikonen (Siikonen, 1995).

Finflo has been used as a flow solver in the modelling of different types of turbomachinery flows, such as in the flow modelling of centrifugal compressors (Turunen-Saaresti, 2004; Tang, 2006; Jaatinen, 2009), ORC turbines (Hoffren et al., 2002; van Buijtenen et al., 2003), and supersonic axial turbines (Grönman, 2010; Grönman et al., 2013). Grönman et al. (2013) modelled a transonic turbine cascade and demonstrated the reliability of the modelling with Finflo in a case where shock waves occur. In addition, the results obtained by using Finflo were compared to the results obtained by two other flow solvers in modelling high-expansion ratio real-gas flows in supersonic ORC turbine stator (Harinck, 2010). In general, the results obtained with different flow solvers were in a good agreement showing small differences mainly in a predicted shock wave strength as well as on the wake dissipation. It should be noted, that due to the lack of available experimental data on real gas flows occurring in the so-called dense gas region, the used CFD code has not been validated with real gas flow measurements. Based on the experimental results obtained in the measurements for a commercial 160 kW ORC, a reasonably good performance prediction for the turbine was estimated by using Finflo in the turbine design (van

Buijtenen et al., 2003; van Buijtenen, 2009). However, detailed experimental results on the turbine flow field and performance are lacking in the literature and thus, no validation of the accuracy of the solver has been carried out. Finflo was selected as a flow solver since it has been extended to allow for real-gas simulations, by using a real gas models based on accurate polynomial fittings.

Finflo employs the finite-volume method for spatial discretization, and Roe's flux difference splitting (Roe, 1981) was used as an approximate Riemann solver. The second order upwind-method was used as a spatial discretization method in the presented simulations. The turbine simulations were performed by using the Chien's $k-\epsilon$ (Chien, 1982) and $k-\omega$ SST-turbulence model (Menter, 1993), and the results obtained by the different turbulence models were compared to discuss the effect of the turbulence model on the predicted flow field and losses. The turbine stator flow channel and the turbine rotor were modelled separately, and the used boundary conditions and the methods are presented in more detail in the section Stator and nozzle simulations as well as in the section Rotor simulations.

3.3.1 Real Gas Model

The accurate real gas model was implemented in a CFD-flow solver to predict the flow field in the designed turbine. The real gas model is based on the polynomial fitting of the fluid properties in a superheated gas region, and the method has been described previously by (Tang, 2006; Turunen-Saaresti et al., 2006). In the real-gas model used in this study, temperature and pressure are independent variables, and the model is based on the polynomial fitting of the fluid properties in the superheated gas region at subcritical pressure levels. Density, internal energy, dynamic viscosity, speed of sound, and thermal conductivity are functions of temperature and pressure.

The applied polynomial is of fourth order, and an example of fourth order polynomial for density, ρ, as a function of temperature, T, and pressure, p, is defined as

$$\begin{aligned}\rho(T,p) = a_1 + a_2T + a_3p + a_4T^2 + a_5Tp + a_6p^2 + a_7T^3 + a_8T^2p + a_9Tp^2 \\ +a_{10}p^3 + a_{11}T^4 + a_{12}T^3p + a_{13}T^2p^2 + a_{14}Tp^3 + a_{15}p^4.\end{aligned} \tag{3.27}$$

Multivariable non-linear regression was used in determining the coefficients a_1-a_{15} by using nonlinear least square fitting. The minimum sum of relative values was aimed in the regression instead of minimum sum of absolute values since the minimum sum of the relative difference provides more accurate polynomials in the studied superheated gas region. The objective function of minimizing the sum of relative difference between the values calculated by the polynomial fitting and the values calculated by Refprop can be defined as

$$min(f) = min\Sigma(\frac{\rho_{\text{polynomial}} - \rho_{\text{Refprop}}}{\rho_{\text{Refprop}}}). \tag{3.28}$$

The used polynomial reconstruction allows to implement accurate thermodynamic properties of the fluid for the solver. The relative difference between the results for speed

of sound, density, viscosity, and thermal conductivity, obtained with the polynomial and Refprop, are presented in Figure 3.7 showing the data points of the superheated gas re-

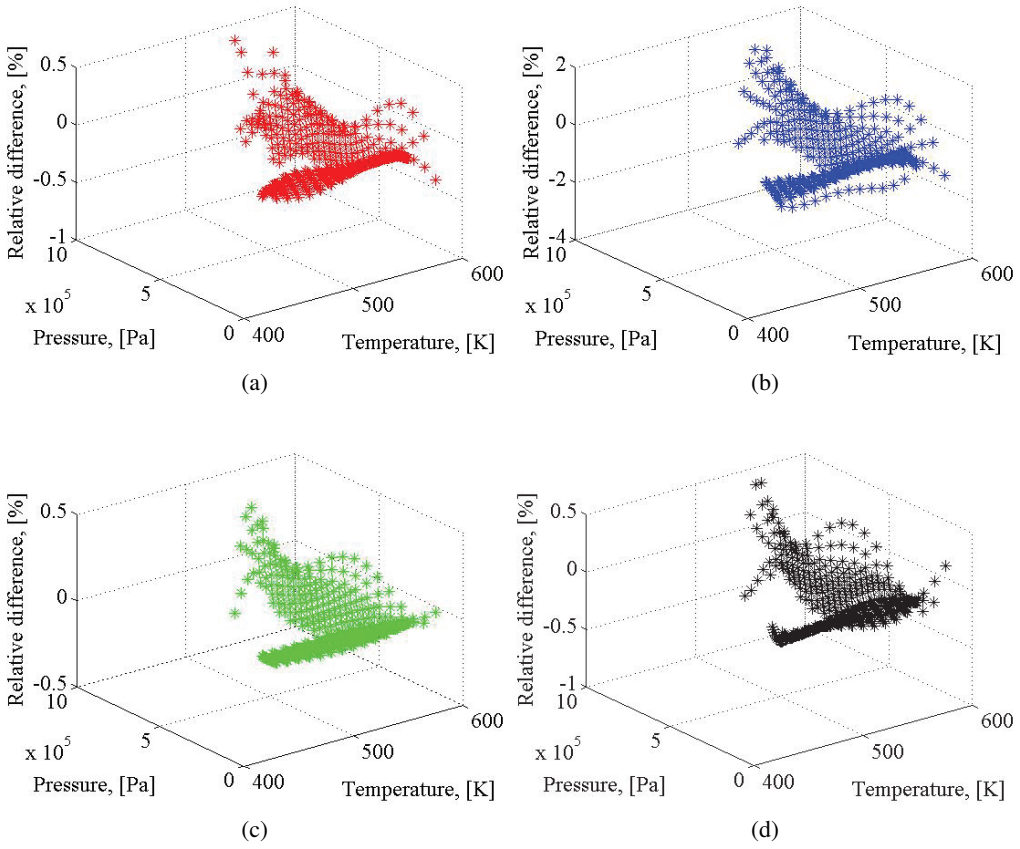

Figure 3.7: Relative difference on the results of speed of sound (a), density (b), viscosity (c), and thermal conductivity (d) between the polynomial and Refprop.

gion, into which the polynomial fitting is applied. The average relative difference in the speed of sound (a) is 0.02 %, in viscosity (μ) 0.04 %, in density (ρ) 0.03 %, and in thermal conductivity (k) 0.00009 %, when comparing the results of polynomial and results of Refprop in the studied superheated gas region. The equation of state of MDM implemented in Refprop is reported to predict superheated vapor density within 2% accuracy in respect to measurements (Colonna, 2008). Thus, the accuracy of the polynomial fittings is significantly higher than the reported accuracy between the results of Refprop and measurements.

3.3.2 Stator and nozzle simulations

The simulations were performed for a convergent-divergent nozzle and for different stator geometries. The studied geometries were 2D-geometries. In the nozzle simulations, the total enthalpy and momentum were used as the inlet boundary conditions, and the zero-gradient outlet boundary was used in the simulations since the outlet flow velocity, normal to the outlet boundary, is supersonic in the nozzle simulations. In the stator simulations, one 2D stator flow channel geometry was modelled, and the periodic boundary conditions were used in the inlet block and outlet block. Total enthalpy and momentum were used as the inlet boundary conditions, and uniform static pressure distribution was defined as the outlet boundary in the stator flow channel simulations, because the flow velocity, normal to the outlet boundary, is subsonic. The stator and nozzle blades were treated as solid walls. Structured grids were used in the modelling and the computational grids were generated to have the nondimesional wall distance y^+ close to unity at the cell adjacent to the solid walls, in order to solve the boundary layer accurately. An example of a 2D convergent-divergent nozzle geometry is presented in Figure 3.8, and a 2D stator flow channel presenting the used boundary conditions and an example computational grid are presented in Figure 3.9.

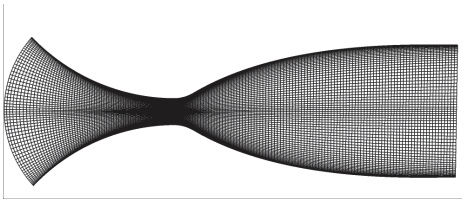

Figure 3.8: Example geometry and computational grid of a supersonic nozzle.

3.3.3 Rotor simulations

Rotor geometries were studied by modelling one 3D rotor flow channel by using the implemented real gas model. The rotor blades, hub, and shroud were treated as rotating solid walls and the grids were generated to have the nondimesional wall distance y^+ close to unity at the cell adjacent to the solid walls. Structured grids were used and no tip clearance was modelled in the rotor simulations. Periodic boundary conditions were used in the inlet and outlet blocks. An example of a structured computational grid and the boundary conditions used in the rotor flow channel simulations are presented in Figure 3.10.

The inlet conditions of the rotor simulations were based on the area averaged results of the stator simulations and by assuming an uniform flow distribution at the rotor inlet. The velocity vectors at the inlet block were turned into the same flow angle α_1 as obtained as the area averaged result in the stator flow channel simulations. It should be noted that the flow field at the stator outlet was predicted to be highly non-unifrom and thus, more accurate rotor inlet conditions would be achieved if the stator and rotor geometry would

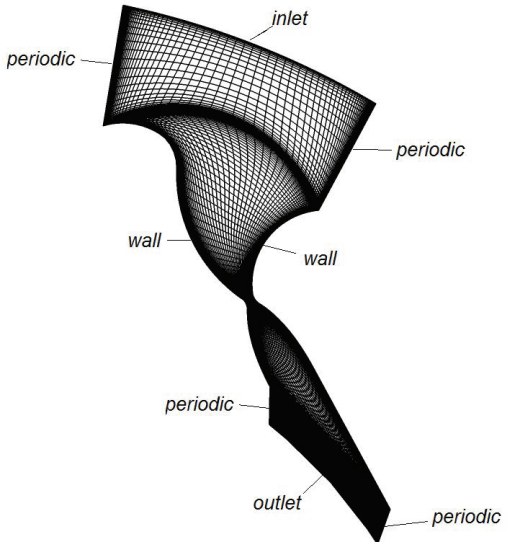

Figure 3.9: Example of 2D stator flow channel boundary conditions and example of a computational grid used in the stator simulations.

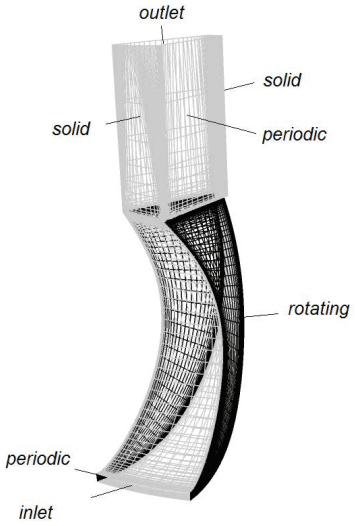

Figure 3.10: Example of a computational grid used in the turbine rotor simulations.

be simulated together. The static pressure was used as the outlet boundary condition in the simulations.

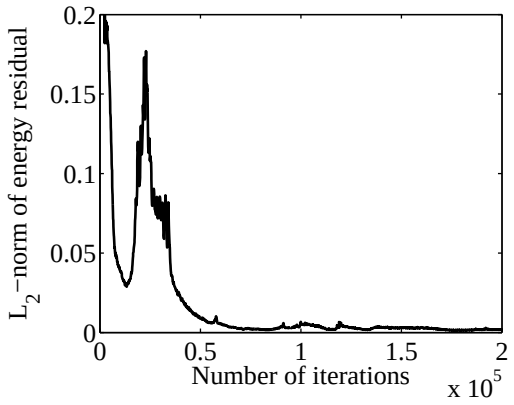

Figure 3.11: Example of simulation convergence monitoring in stator simulations.

3.3.4 Convergence monitoring

The convergence of the simulations was monitored by following the stabilization of inlet and outlet mass flow rates and the L_2-norm residuals. An example of the simulation convergence presenting the L_2-norm of energy residual in a stator simulation is presented in Figure 3.11. The simulations were considered to be converged when the inlet and outlet mass flows were stabilized and the relative difference was in the range from 0.5 % to 3 % in the stator simulations. The relative difference between the mass flow rate at the inlet and outlet was slightly higher in the rotor simulations when compared to the stator simulations. In addition to monitoring the inlet and outlet mass flow rates, the stabilization of L_2-norm density, momentum, and energy residuals were monitored in the simulations.

4 Study on dry ORC working fluids

The objective of this chapter is to perform a preliminary evaluation of suitable working fluid candidates for small-scale ORC systems adopting high-speed turbines. First, a thermodynamic analysis was carried out to highlight and discuss the special features related to the use of working fluids from different fluid groups, as well as to study the dependence of the critical temperature and molecular weight of the fluid on the most important process parameters. All the selected working fluids have a dry expansion to prevent droplets occurring in the turbine. In addition, the use of dry working fluids enables the use of a recuperator in the cycle. Second, a preliminary radial turbine design was carried out for several working fluids to evaluate and compare the availability for designing small-scale turbines with different fluids, as well as to investigate the main turbine dimensions and rotational speeds as a function of turbine power output. The selected turbine power output range is from 10 kW to 200 kW.

4.1 Thermodynamic analysis

A thermodynamic analysis of subcritical processes adopting evaporation pressure slightly lower than the critical pressure of the fluid were carried out with two different condensing temperatures of 50 ^{o}C and 100 ^{o}C. The results were obtained by using the evaporation pressure of $p_{\mathrm{ev}}/p_{\mathrm{cr}}$=0.9 for each fluid, in order to study processes having the evaporation pressure close to the critical pressure of the fluid and thus representing cycle efficiencies relatively close to the maximum efficiency that can be obtained with a subcritical process. It should be noted that this kind of approach was evaluated being suitable in the preliminary evaluation and in the comparison of working fluids, but in a more detailed design of ORC systems, the evaporation pressure of each fluid is highly dependent on the heat source temperature level as well as on the process optimization method. A more detailed thermodynamic analysis taking into account the temperature profiles in the heat exchangers is presented later in Chapter 5 and Chapter 7 for the studied applications.

The vapor was superheated by 10 ^{o}C with all the fluids because a flow through type of evaporator was considered, which requires a superheating in the process (Talonpoika, 1996). Recuperator effectiveness of 0.6 was used which, enables the use of a recuperator, where the flow arrangement can also differ from the pure countercurrent flow configuration; and a feed pump efficiency of 60 % was used in the simulations. The turbine isentropic efficiency of 75 % was used in the simulations, which was evaluated as a realistic value for the turbine efficiency when considering small-scale ORC turbines (Verneau, 1987; van Buijtenen et al., 2003; Kang, 2012).

The thermodynamic analysis is structured as follows. First, the relation between the molecular weight and the critical temperature and the critical pressure is studied. Second, the relation between the cycle efficiency and the critical temperature is studied and discussed. Third, the relation between the critical temperature and the condensing pressure, the expansion ratio, and the enthalpy drop over the turbine are studied and discussed.

Fourth, the relation between the critical temperature and the speed of sound at the turbine inlet is studied. The studied working fluids can generally be divided into three categories: i) hydrocarbons that consist of hydrogen and carbon atoms; ii) siloxanes that consist of silicon, hydrogen, carbon, and oxygen atoms; and iii) fluorocarbons that consist of carbon, fluorine, and hydrogen atoms. The studied working fluids and their classification, molecular weight, critical pressure, and critical temperature, as well as the literature reference used for the equations of state in Refprop are listed in Table 4.1.

Table 4.1: Studied working fluids

Fluid	Chemical formula	Classification	M [kg /kmol]	P_{crit} [bar]	T_{crit} [^{o}C]	Reference
Hydrocarbons						
dodecane	$C_{12}H_{26}$	linear alkane	170.3	18.2	385.0	(Lemmon and Huber, 2004)
decane	$C_{10}H_{22}$	linear alkane	142.3	21.0	344.6	(Lemmon and Span, 2006)
nonane	C_9H_{20}	linear alkane	128.3	22.8	321.4	(Lemmon and Span, 2006)
octane	C_8H_{18}	linear alkane	114.2	25.0	296.2	(Span and Wagner, 2003)
heptane	C_7H_{16}	linear alkane	100.2	27.4	267.0	(Span and Wagner, 2003)
toluene	C_7H_8	aromatic hydrocarbon	92.1	41.3	318.6	(Lemmon and Span, 2006)
hexane	C_6H_{14}	linear alkane	86.2	30.3	234.7	(Span and Wagner, 2003)
isohexane	C_6H_{14}	branched-chain alkane	86.2	30.4	224.6	(Lemmon and Span, 2006)
cyclohexane	C_6H_{12}	cycloalkane	84.2	40.8	280.5	(Penoncello et al., 1995)
benzene	C_6H_6	aromatic hydrocarbon	78.1	49.1	288.9	(Thol et al., 2012)
pentane	C_5H_{12}	linear alkane	72.1	33.7	196.6	(Span and Wagner, 2003)
isopentane	C_5H_{12}	branched-chain alkane	72.1	33.8	187.2	(Lemmon and Span, 2006)
neopentane	C_5H_{12}	branched-chain alkane	72.1	32.0	160.6	(Lemmon and Span, 2006)
cyclopentane	C_5H_{10}	cycloalkane	70.1	45.2	238.5	(unpublished)
butene	C_4H_8	linear alkene	56.1	40.1	146.1	(Lemmon and Ihmels, 2005)
isobutene	C_4H_8	branched-chain alkene	56.1	40.1	144.9	(Lemmon and Ihmels, 2005)
cis-butene	C_4H_8	acyclic alkene	56.1	42.3	162.6	(Lemmon and Ihmels, 2005)
trans-butene	C_4H_8	acyclic alkene	56.1	40.3	155.5	(Lemmon and Ihmels, 2005)
butane	C_4H_{10}	linear alkane	58.1	38.0	152.0	(Buecker and Wagner, 2006)
isobutane	C_4H_{10}	branched-chain alkane	58.1	36.3	134.7	(Buecker and Wagner, 2006
Siloxanes						
MD_4M	$C_{14}H_{42}O_5Si_6$	linear siloxane	459.0	8.8	380.1	(Colonna et al., 2006c)
D_6	$C_{12}H_{36}Si_6O_6$	cyclic siloxane	444.9	9.6	372.6	(Colonna et al., 2008)
MD_3M	$C_{12}H_{36}Si_5O_4$	linear siloxane	384.8	9.5	355.2	(Colonna et al., 2008)
D_5	$C_{10}H_{30}O_5Si_5$	cyclic siloxane	370.8	11.6	346.1	(Colonna et al., 2006c)
MD_2M	$C_{10}H_{30}Si_4O_3$	linear siloxane	310.7	12.3	326.3	(Colonna et al., 2008)
D_4	$C_8H_{24}O_4Si_4$	cyclic siloxane	296.6	13.3	313.3	(Colonna et al., 2006c)
MDM	$C_8H_{24}O_2Si_3$	linear siloxane	236.5	14.2	290.9	(Colonna et al., 2008)
MM	$C_6H_{18}OSi_2$	linear siloxane	162.4	19.4	245.5	(Colonna et al., 2006c)
Fluorocarbons						
R365mfc	$C_4H_5F_5$	hydrofluorocarbon	148.1	32.7	186.9	(unpublished)
RC318	C_4F_8	fluorocarbon	200.0	27.8	115.2	(Platzer et al., 1990)
R134a	$C_2H_2F_4$	hydrofluorocarbon	102.0	40.6	101.1	(Tillner-Roth and Baehr, 1994)
R227ea	C_3HF_7	hydrofluorocarbon	170.0	29.3	101.8	(unpublished)
R236ea	$C_3H_2F_6$	hydrofluorocarbon	152.0	35.0	139.3	(Huber and Ely, 1994)
R245ca	$C_3H_3F_5$	hydrofluorocarbon	134.0	39.3	174.4	(Huber and Ely, 1994)
R245fa	$C_3H_3F_5$	hydrofluorocarbon	134.0	36.5	154.0	(Lemmon and Span, 2006)

The following abbreviations are used for different working fluid groups in the figures presenting the results of the analysis: LA represents linear alkanes, AA acyclic alkenes, BCA branched-chain alkanes, AH aromatic hydrocarbons, CA cycloalkanes, CS cyclic siloxanes, LS linear siloxanes, and FC fluorocarbons.

4.1.1 The relation between the molecular weight and the critical temperature and critical pressure

The relation between the molecular weight of the fluid and the critical temperature, as well as the relation between the molecular weight and the critical pressure of the working fluid, are presented in Figure 4.1a and Figure 4.1b. There is a clear relation between the

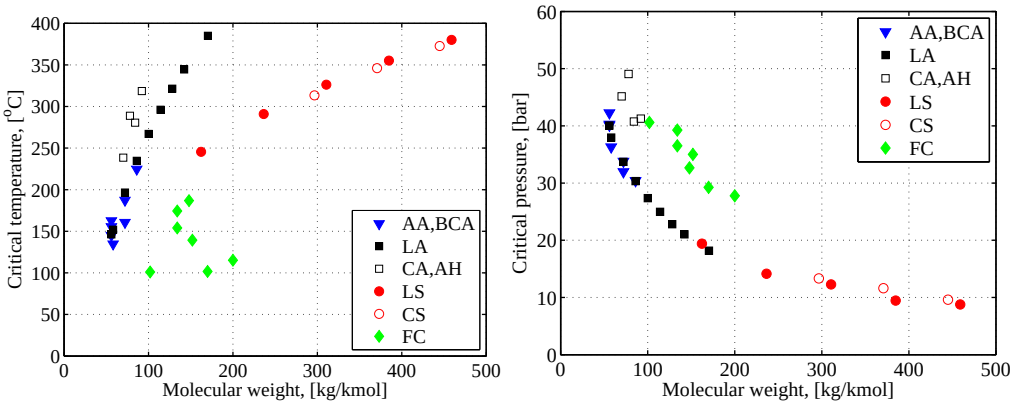

Figure 4.1: Relation between the molecular weight and the critical temperature (a) and critical pressure (b) with different fluids.

molecular weight and the critical temperature and critical pressure of the fluid, especially with the studied hydrocarbons and siloxanes. In general, when the molecular weight of the fluid increases, the critical temperature increases and the critical pressure decreases. In the hydrocarbon group, the fluids classified as linear alkanes, branched-chain alkanes, and acyclic alkenes represent lower critical temperatures and lower critical pressures with respect to the molecular weight of the fluid when compared to the studied cycloalkanes and aromatic hydrocarbons. With siloxanes, only slight differences in the relation of the molecular weight to the critical temperature or critical pressure can be observed when comparing a cyclic siloxane and a linear siloxane having the molecular weights relatively close to each other. With the studied fluorocarbons, a clear correlation between the molecular weight and the critical temperature cannot be identified. This can be mainly explained by the variation in the molecular structures of the studied fluorocarbons. However, a relation between the molecular weight and the critical pressure can also be observed with the studied fluorocarbons.

4.1.2 Cycle efficiency

The results for the relation between the critical temperature of the fluid and the obtained ORC process electric efficiencies for a subcritical process adopting the evaporation pressure of p_{ev}/p_{crit}=0.9 are presented in Figure 4.2a, Figure 4.2b, and Figure 4.2c. Figure

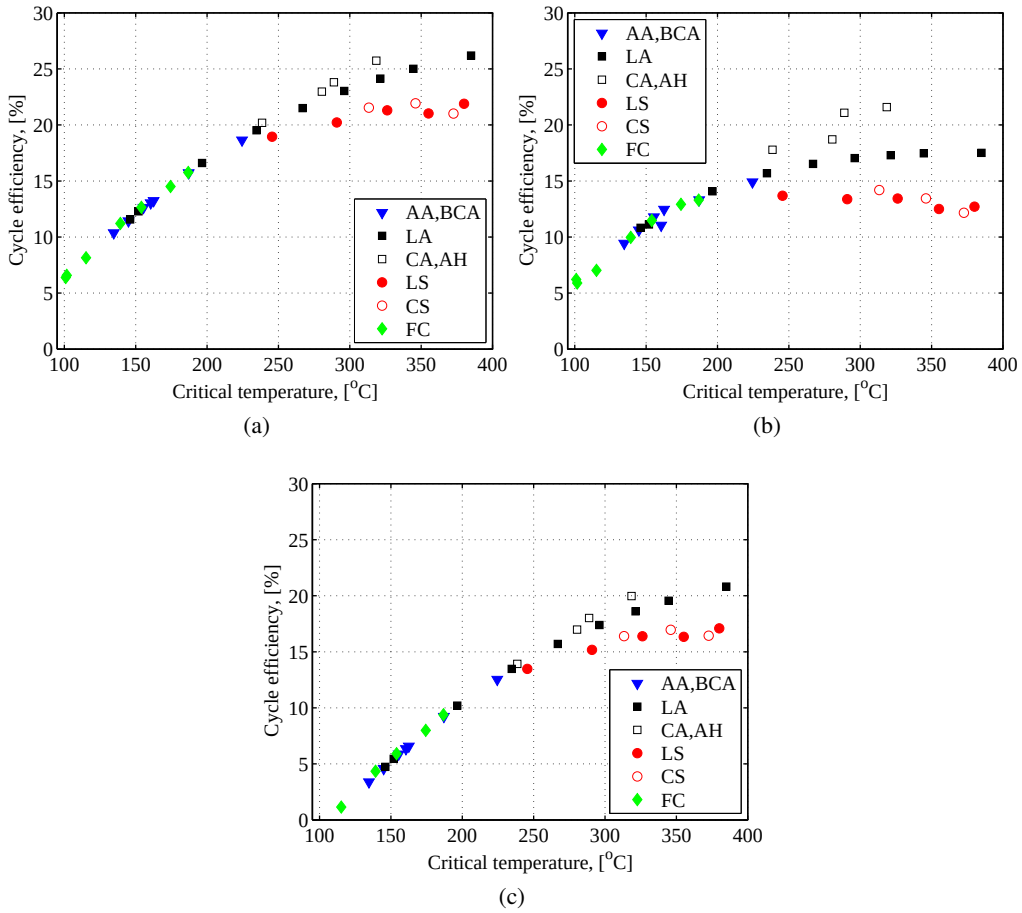

Figure 4.2: Relation between the critical temperature and the process electric efficiency with T_c=50 °C with a recuperator (a), T_c=50 °C without a recuperator (b), and T_c=100 °C with a recuperator (c).

4.2a represents the results for an ORC process with a recuperator and when the condensing temperature of 50 °C is used. Figure 4.2b represents an ORC process without a recuperator and when the condensing temperature of 50 °C is used. Figure 4.2c represents an ORC process with a recuperator and when the condensing temperature of 100 °C is used. In general, the results indicate that there is a relatively strong correlation between the obtained cycle efficiency and the critical temperature of the fluid. The fluids with a high critical temperature represent the highest cycle efficiencies in the range from about 20 % to 26 % in a case when the lower condensing temperature and recuperator are used while the fluids with lower critical temperature represents efficiencies in the range from about 5 % to 15 % for the same case. This can be mainly explained by the higher turbine inlet temperatures with fluids having a high critical temperature when compared to the

fluids having a lower critical temperature, and thus, the temperature difference between the turbine inlet and condenser is higher resulting to higher cycle efficiencies.

The low critical temperature hydrocarbons and fluorocarbons represent comparably similar efficiencies, and only slight differences can be observed between the different fluid groups. However, when using fluids with higher critical temperatures, more notable differences in the cycle efficiency can be observed when comparing fluids from different groups, namely the siloxanes, high critical temperature linear hydrocarbons, and aromatic hydrocarbons, as well as the cycloalkanes. The cycloalkanes and aromatic hydrocarbons represent higher cycle efficiencies when compared to the linear alkanes having a relatively similar critical temperature. With siloxanes, the cycle efficiency increases only slightly, or even slightly decreases with some fluids, when a siloxane with higher critical temperature is adopted to the cycle.

The results for a cycle without a recuperator indicate that the cycle efficiencies obtained with hydrocarbons and especially siloxanes are significantly lower when compared to the processes equipped with a recuperator, and the deviation in the cycle efficiencies of different fluid groups is more pronounced in the process without the recuperator. A significant reduction in the simulated cycle efficiency can be observed also with the fluorocarbons having the highest critical temperatures when comparing the results of the processes with and without a recuperator. The results presented in Figure 4.2a and Figure 4.2c show that the condensing temperature has a significant impact on the cycle efficiency and a higher cycle performance is achieved when adopting a lower condensing temperature.

4.1.3 Condensing pressure and expansion ratio over the turbine

The process condensing pressure, p_c, and the expansion ratio over the turbine, $v_{t,out}$/ $v_{t,in}$, were studied because these parameters were evaluated as important, especially when considering the turbine design and type, as well as in evaluating the size of the process heat exchangers. The relation between the critical temperature and the condensing pressure is presented in Figure 4.3a, Figure 4.3b, and Figure 4.3c.

The results indicate that a clear relation between the critical temperature and the condensing pressure can be identified. In general, the higher the critical temperature of the fluid, the lower the simulated condensing temperature when compared to another fluid of the same working fluid group. Siloxanes and high critical temperature hydrocarbons represent significantly low condensing pressures, having values well below the atmospheric pressure, especially in the case of a low condensing temperature of 50 ^{o}C. The studied fluorocarbons represent condensing pressures above the atmospheric pressure, both with the high condensing temperature and the low condensing temperature. The use of fluids representing the lowest condensing pressures might lead to technical difficulties in the condenser design when a low condensing temperature is used, and thus, these fluids can be considered to be more potential for ORC systems that have relatively high condensing temperatures.

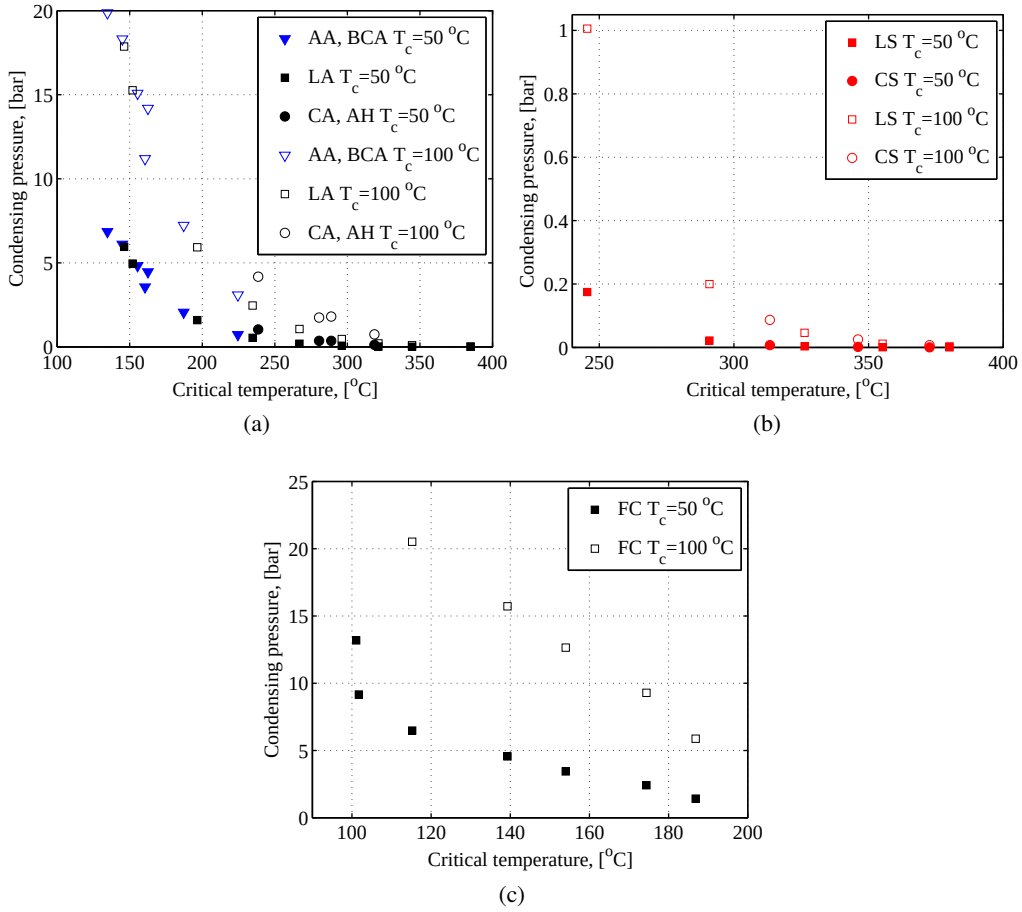

Figure 4.3: Relation between the critical temperature and the process condensing pressure with hydrocarbons (a), siloxanes (b), and fluorocarbons (c). Two different condensing temperatures of 50 °C and 100 °C were considered.

The results for the relation between the critical temperature and the expansion ratio, $v_{t,out}/v_{t,in}$, over the turbine are presented in Figure 4.4a, Figure 4.4b, and Figure 4.4c. The results indicate that the expansion ratio over the turbine is higher when a fluid with a higher critical temperature is used, compared to the use of a fluid from the same fluid group having a lower critical temperature. The high expansion ratios over the turbine are observed especially when adopting hydrocarbons with high critical temperatures or siloxanes as working fluids. The high expansion ratio over the turbine results in a configuration where a large change in the flow area between the turbine inlet and outlet is needed. In addition, the use of fluids having a high expansion ratio over the turbine and a low condensing pressure leads to a large volumetric flow rate at the turbine outlet caused

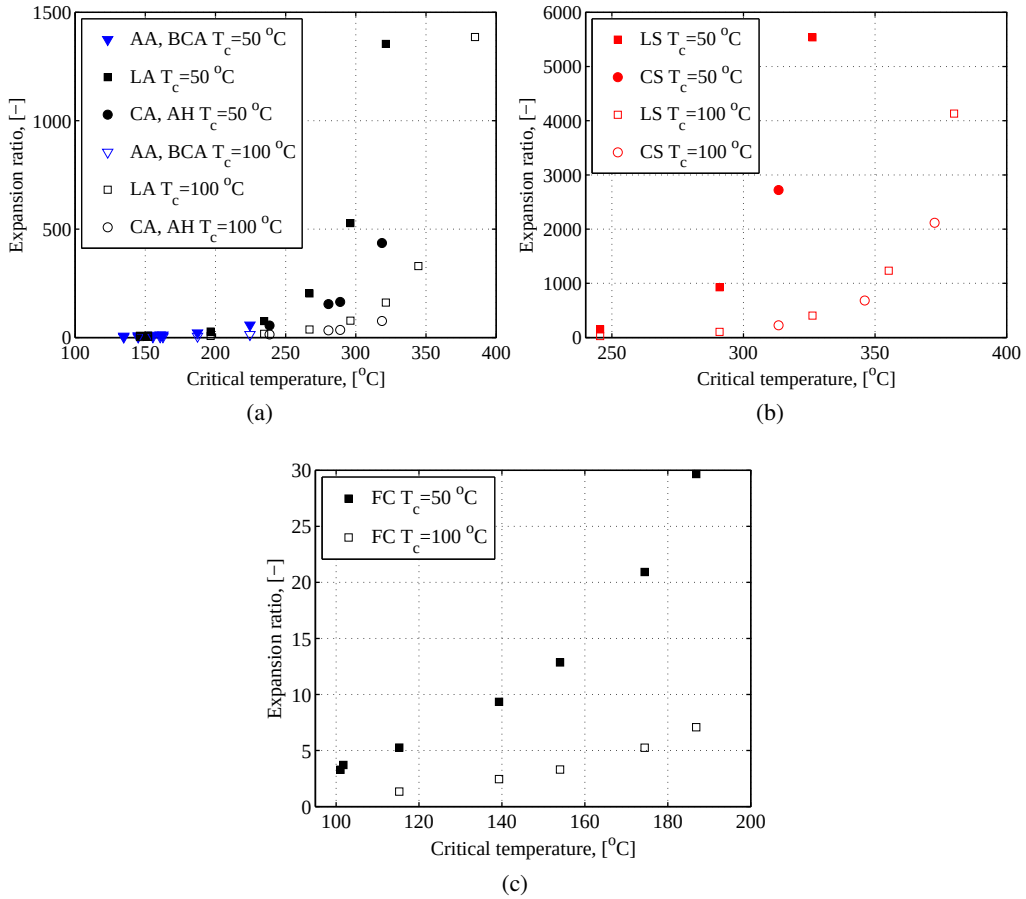

Figure 4.4: Relation between the critical temperature and the process expansion ratio with hydrocarbons (a), siloxanes (b), and fluorocarbons (c). Two different condensing temperatures of 50 °C and 100 °C were considered

by the low vapor density at the low pressure side of the process. The volumetric flow rate is closely connected to the sizing of the heat exchangers at the cycle low-pressure side, namely on the sizing of the recuperator and condenser. Therefore, a large volumetric flow rate is estimated to lead to the use of large-sized heat exchangers on the process low pressure side when compared to the fluids having a low volumetric flow rate.

4.1.4 Enthalpy change over the turbine

The results of the relation between the critical temperature and the enthalpy change over the turbine are presented in Figure 4.5a and Figure 4.5b. The enthalpy change over the turbine is important parameter because it has a large impact on the turbine design, mainly on the selection of the number of turbine stages and on the turbine rotational speed. The

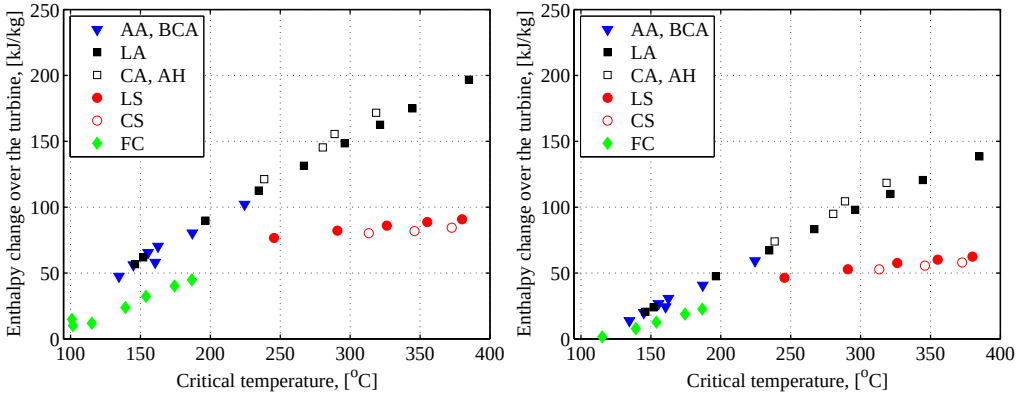

Figure 4.5: Relation between the critical temperature and the enthalpy change over the turbine, T_c=50 °C (a) and T_c=100 °C (b).

results presented in Figure 4.5a and in Figure 4.5b indicate that the relation between the critical temperature of the fluid with the enthalpy change over the turbine is almost linear inside each working fluid group, and the highest enthalpy changes in the range form about 100 kJ/kg to 200 kJ/kg can be observed with the hydrocarbons having a high critical temperature while the lowest enthalpy changes below 50 kJ/kg can be observed with the studied fluorocarbons and low critical temperature hydrocarbons. This can be mainly explained by the fact that the fluids having a high critical temperature have a higher turbine inlet temperature in the simulations when compared to the fluids having a lower critical temperature, and thus, the temperature difference between the turbine inlet and condenser is higher. However, the results indicate that the enthalpy change over the turbine is highly dependent not only on the temperature difference between the turbine inlet and condenser, but is highly affected by the group of the working fluid as well. The results show that the hydrocarbons represent a higher enthalpy change over the turbine when compared to a siloxane or a fluorocarbon having a comparably similar critical temperature.

4.1.5 Speed of sound

The results of the relation between the critical temperature of the fluid and the speed of sound at the turbine inlet are presented in Figure 4.6. The results indicate that all the studied fluids have a relatively low speed of sound ($<$ 170 m/s). The hydrocarbons represent slightly higher speed of sounds when compared to fluorocarbons and siloxanes. The results indicate that a relation between the critical temperature of the fluid and the speed of sound can be observed, and the high critical temperature leads into a low speed of sound, especially with linear hydrocarbons and siloxanes. The speed of sound of the fluid is an important feature to consider, especially when designing turbomachinery for ORC systems with the aim to decrease the losses related to the supersonic flows in ORC turbines.

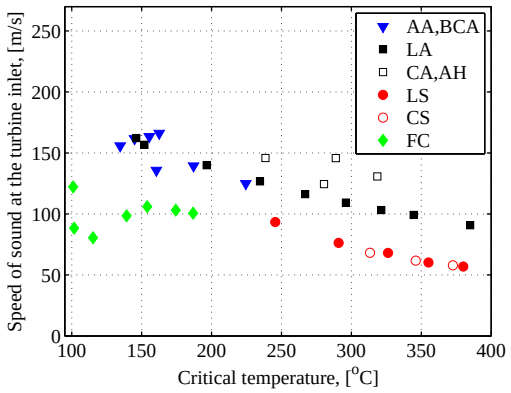

Figure 4.6: Relation between the critical temperature and the speed of sound at the turbine inlet.

When adopting fluids having a low speed of sound, rather complex turbine geometries have to be considered in a case when the flow velocity is limited to be subsonic, because the flow becomes supersonic even at low or moderate flow velocities.

4.2 Turbine design considerations with different working fluids

Preliminary evaluation of turbine dimensions and rotational speeds with different working fluids as a function of turbine power output was carried out to evaluate the suitability of different fluids in small-scale ORCs adopting turbine technology. The studied turbine type is a full admission radial inflow turbine, and the studied turbine power is ranging from 10 kW to 200 kW. The results for the turbine geometries with different fluids were obtained by using the non-dimensional design parameter specific speed N_s. The specific speed was set to 0.5 in the cases because this value enables the design of radial inflow turbines with relatively high efficiency according to the design charts by Balje (1981) and design guidelines by Rohlik (1975). The turbine isentropic efficiency of 75% and a turbine stator isentropic efficiency of 85 % were used for each fluid. The turbine efficiencies used in the simulations were estimated based on the previous studies on small ORC turbines by Verneau (1987), van Buijtenen et al. (2003), and Kang (2012). The absolute flow angle at the rotor inlet (α_1) was set to 75^o based on the optimum flow angle corresponding to the selected specific speeds according to Rohlik (1975). The design method results in a radial turbine having the non-dimensional parameter specific diameter of about 3.2, which enables high efficiency according to the N_s/D_s design charts by Balje (1981). The use of N_s and D_s can be used in the preliminary evaluation of suitable rotational speed and geometry of the turbine and in comparing different fluids. However it should be noted, that the use of N_s and D_s do not take into account the significantly large expansion ratios over the turbines when organic fluids are adopted. Thus, more accurate design of the turbine geometry and turbine efficiency predictions should be carried out by using accurate numerical methods, such as CFD simulations.

First, the turbine designs were carried out by using six hydrocarbons, three fluorocarbons, and two siloxanes to evaluate the turbine dimensions and rotational speed with different working fluids and turbine power levels. The fluids representing the highest expansion ratios over the turbine, mainly the siloxanes and hydrocarbons with the highest critical temperatures, were excluded from this analysis because a single stage turbine is considered. A slightly lower reduced pressure of $p_{t,in}/p_{crit}$=0.8 was adopted at the turbine inlet in this assessment when compared to the previous section in order to reduce the expansion ratio over the turbine. The condensing temperature of 50 ^oC was used, and the vapor was superheated by 10 ^oC in this comparison. The pressure at the rotor inlet was set to $p_{rot,in}$=($p_{t,in}$·$p_{t,out}$)$^{0.5}$ to have an equal pressure ratio over the stator and rotor, leading to the degree of reaction close to 0.5. Diameter ratios D_{2t}/D_1=0.6 and D_{2h}/D_{2t}=0.35 were used to estimate the blade height at the rotor outlet. Second, the results on the effect of degree of reaction and the effect of the turbine inlet pressure on the turbine design are presented and discussed.

4.2.1 Turbine design as a function of turbine power output

The results of the turbine design with different working fluids are presented in the following. The design results that are independent from the turbine power are presented in Table 4.2, and the results for the cycle mass flow rate and volumetric flow rate as a function of turbine power are presented in Figure 4.7a, Figure 4.7b, and Figure 4.7c and in Figure 4.8a, Figure 4.8b, and Figure 4.8c.

Table 4.2: Input data from the process design used as input values in the turbine design and the main results of the turbine design that are independent from the turbine power scale.

Working fluid	$p_{t,in}$ [bar]	$T_{t,in}$ [^oC]	η_e [%]	Δh [kJ/kg]	$v_{t,out}/v_{t,in}$,[-]	Ma_1 [-]	c_1 [m/s]	u_1 [m/s]	t_2/t_1 [-]
toluene	33.0	310.6	23.6	167.9	364.9	2.1	436.0	398.8	25.6
octane	20.0	290.1	21.2	144.9	439.3	2.1	400.7	374.4	28.1
cyclohexane	32.6	272.7	21.02	141.3	128.0	1.9	395.3	370.1	15.5
cyclopentane	36.1	231.6	18.4	117.5	46.6	1.7	359.9	338.0	9.8
isohexane	24.3	219.5	17.0	98.8	48.2	1.7	327.0	312.8	9.9
pentane	27.0	192.1	15.0	86.46	23.3	1.5	305.6	292.9	7.2
R365mfc	26.1	184.0	14.3	43.2	25.2	1.5	215.8	207.3	7.5
R245ca	31.4	171.5	13.1	38.8	17.7	1.4	204.2	196.5	6.4
R245fa	29.2	151.7	11.4	30.8	10.9	1.3	182.8	174.7	5.2
MDM	11.3	286.1	18.6	80.2	776.0	2.2	297.1	279.3	37.5
MM	15.5	241.2	17.3	74.3	126.9	1.9	285.0	270.1	15.8

The results presented in Table 4.2 show that the designed turbines have a supersonic flow at the rotor inlet. The highest absolute Mach numbers can be found when using siloxanes

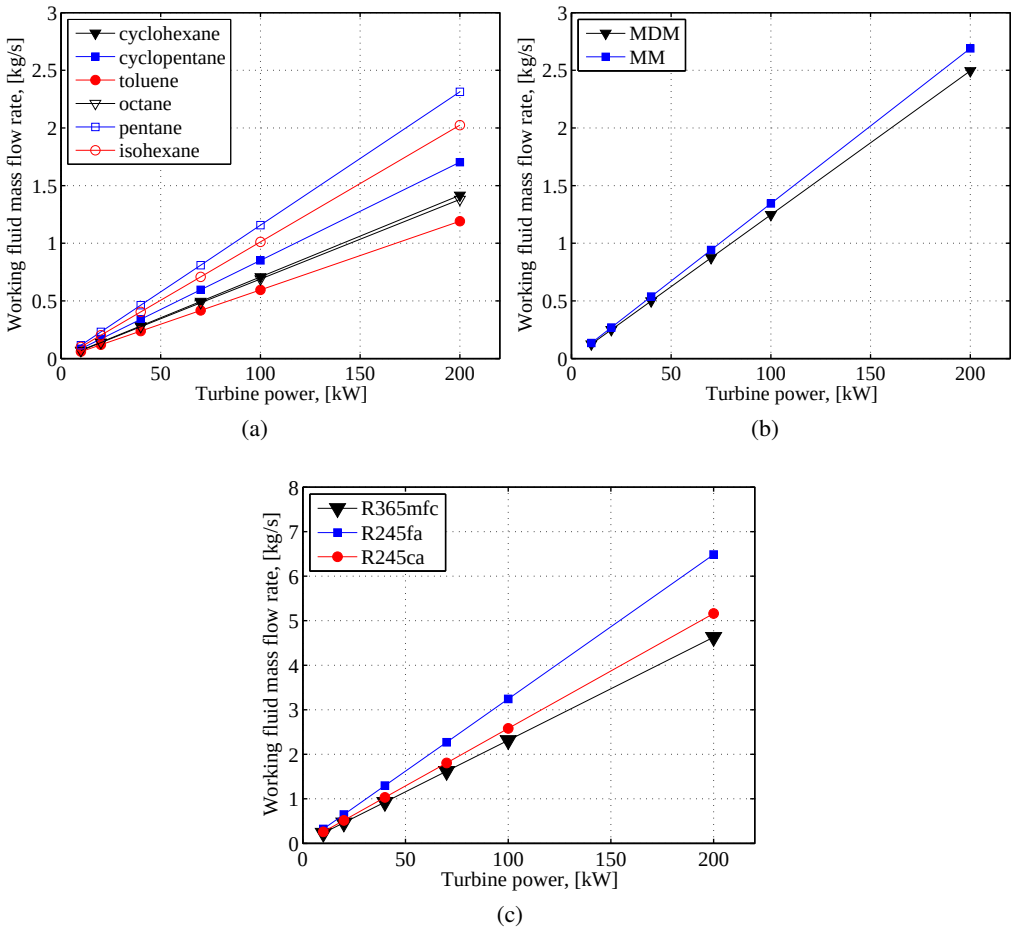

Figure 4.7: Working fluid mass flow rate as a function of turbine power with different (a) hydrocarbons, (b) siloxanes, and (c) fluorocarbons.

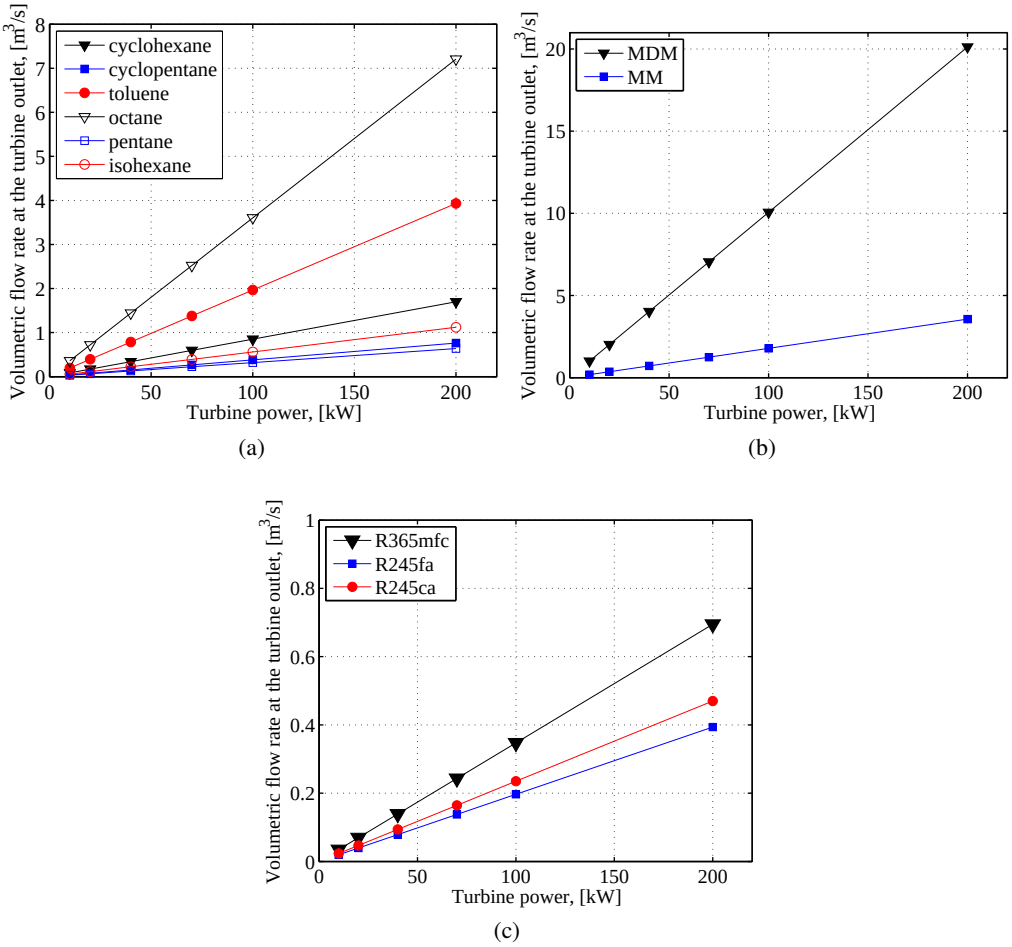

Figure 4.8: Volumetric flow rate at the turbine outlet as a function of turbine power with different (a) hydrocarbons, (b) siloxanes, and (c) fluorocarbons.

or hydrocarbons having the highest critical temperatures while the lowest Mach numbers are obtained with the studied fluorocarbons. In addition, the high critical temperature hydrocarbons and siloxanes represent the highest expansion ratios over the turbine and the largest variation in the turbine blade height between the rotor inlet and outlet. The large variation in the blade height between the inlet and outlet might cause flow separation in the rotor, which will have a negative impact on the turbine efficiency. The highest flow velocities and the highest peripheral speed can be found with turbines operating with hydrocarbons, and the lowest velocities can be found in turbines operating with fluorocarbons. The results presented in Figure 4.7a, Figure 4.7b, and Figure 4.7c show that the fluids with a high critical temperature have a lower mass flow rate through the turbine when compared to fluids having a lower critical temperature. The highest mass flow rates

were simulated with fluorocarbons and the lowest mass flow rates with hydrocarbons. According to the results presented in Figure 4.8a, Figure 4.8b, and Figure 4.8c, the high critical temperature fluids represent the highest volumetric flow rates at the turbine outlet, and the lowest volumetric flow rates were obtained with fluorocarbons and low critical temperature hydrocarbons.

The results of the turbine rotational speed are presented in Figure 4.9a, Figure 4.9b, and Figure 4.9c. Based on the results, the studied hydrocarbons represent the highest tur-

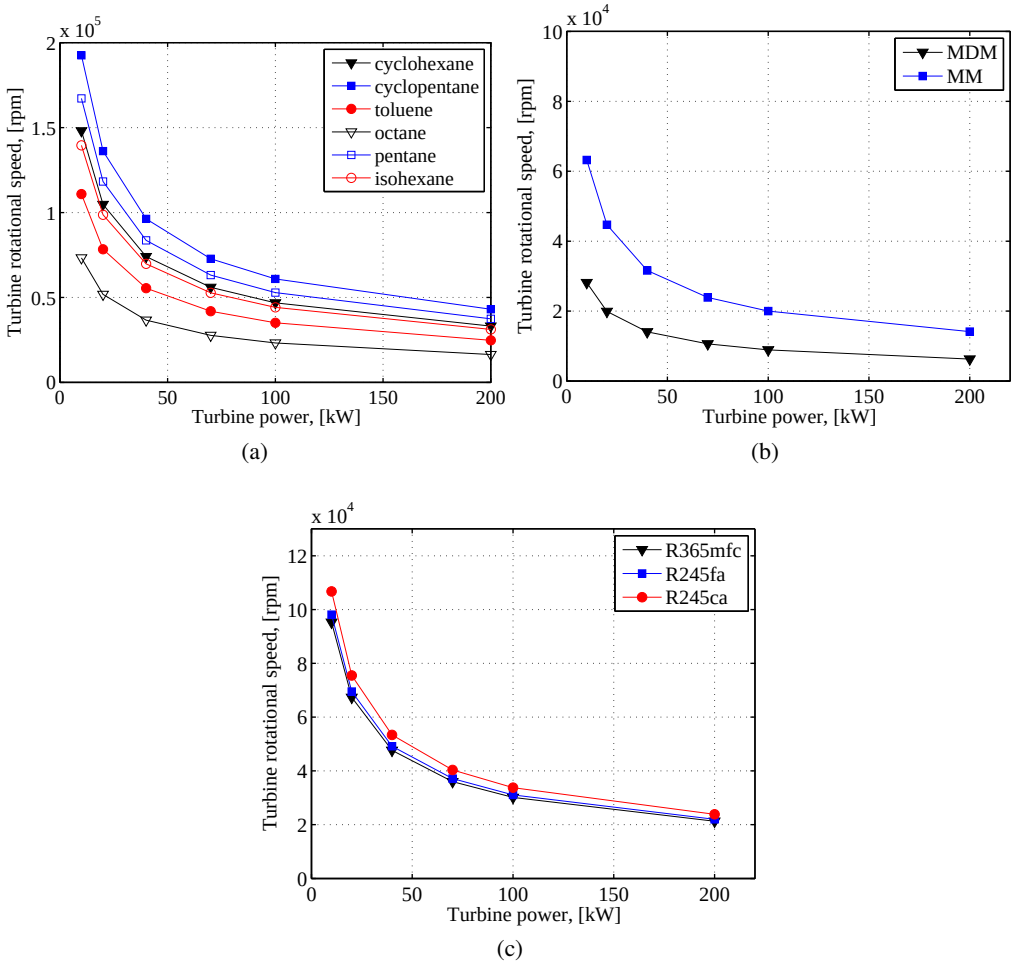

Figure 4.9: Turbine rotational speed as a function of turbine power with different (a) hydrocarbons, (b) siloxanes, and (c) fluorocarbons.

bine rotational speeds, and the studied siloxanes represent the lowest turbine rotational speeds. The calculated rotational speed is above 100 000 rpm with most of the studied

hydrocarbons when the turbine power is in the range from 10 to 20 kW and the studied fluorocarbons represent only slightly lower rotational speeds. The turbine rotational speed decreases significantly when a higher turbine power level is considered. The lowest rotational speeds were calculated for turbines operating with siloxane MDM and the highest rotational speeds with hydrocarbon cyclopentane.

The results of the blade height at the rotor inlet are presented in Figure 4.10a, Figure 4.10b, and Figure 4.10c. The studied siloxanes and fluorocarbons represent turbines with

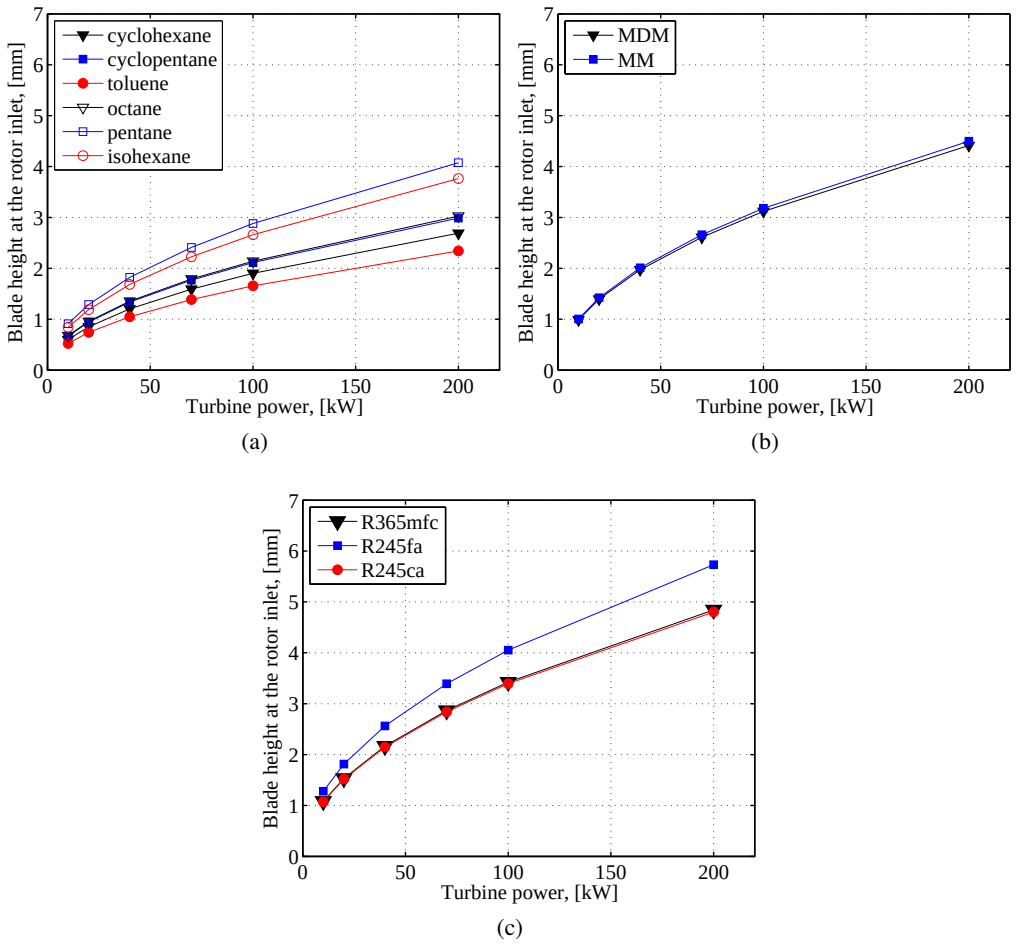

Figure 4.10: Turbine blade height at the rotor inlet as a function of turbine power with different (a) hydrocarbons, (b) siloxanes, and (c) fluorocarbons.

higher blade heights at the rotor inlet when compared to the studied hydrocarbons, especially when compared to the hydrocarbons with the highest critical temperature, namely toluene or octane. The hydrocarbons represent blade heights below 1 mm at the low-

est turbine power range, and only slightly higher blade heights were obtained with the siloxanes and fluorocarbons. Significantly higher blade heights at the rotor inlet can be observed when turbines having a power output in the range from 50 kW to 200 kW are designed. The largest blade heights were calculated for turbines operating with fluorocarbon R245fa, and the smallest blade heights were calculated for turbines operating with hydrocarbon toluene. The small blade heights at the rotor inlet are estimated to lead to difficulties in manufacturing the turbine flow channels, as well as to reductions in the turbine efficiency, caused by the tip clearance loss and relatively thick boundary layers when compared to the height of the flow channel. Shrouded impellers could be considered to reduce the tip clearance losses related to the small blade height. On the other hand, the effect of the tip clearance at the rotor inlet on the radial turbine efficiency has been reported to be smaller when compared to the axial turbines(Dambach et al., 1999).

The results of the turbine rotor diameters are presented in Figure 4.11a, Figure 4.11b, and Figure 4.11c as a function of turbine power. The largest turbine wheels are obtained with the studied siloxanes and with high critical temperature hydrocarbons, representing the highest volumetric flow rates at the turbine outlet, while the smallest turbine wheels are obtained with fluorocarbons and with low molecular weight hydrocarbons, representing the lowest volumetric flow rates at the turbine outlet. The largest turbine wheels were calculated for turbines operating with siloxane MDM, and the smallest turbine wheels were calculated for turbines operating with hydrocarbon cyclopentane and fluorocarbon R245fa.

4.2.2 Effect of the degree of reaction on the turbine design

The results on the effect of the degree of reaction on the turbine blade height at the rotor inlet are presented Figure 4.12a, the effect on the blade height ratio t_2/t_1 in Figure 4.12b, the effect on the velocity ratio c_{u1}/u_1 in Figure 4.12c, and the effect on the absolute Mach number at the rotor inlet in Figure 4.12d. These turbine designs were carried out by using toluene, MDM, and R245fa as working fluids and a turbine power output of 100 kW was used. The degree of reaction was varied by changing the static pressure between the turbine rotor and stator. Based on the results a low degree of reaction allows to have a larger blade height at the rotor inlet when compared to a higher degree of reaction. In addition, lower variations between the rotor inlet and outlet blade height were observed based on the rotor blade height ratio t_2/t_1 when a low degree of reaction was adopted. However, the low degree of reaction changes the velocity ratio c_{u1}/u_1 at the rotor inlet and leads to higher Mach number at the stator outlet as well as results in higher relative velocities at the rotor inlet. If the velocity ratio c_{u1}/u_1=1, the velocity triangle is as presented in Figure 3.4a and is typical for radial turbines in which straight blades are used at the rotor inlet. If the velocity ratio is higher, the velocity tringle at the rotor inlet is as presented in Figure 3.4b, and if straight blades are used at the turbine inlet, the incidence angle of the relative velocity increases and might cause flow separation at the rotor inlet. Thus, curved blades could be considered at the rotor inlet in this case. In addition, the higher Mach number at low degrees of reaction introduces additional losses related to highly supersonic flow at

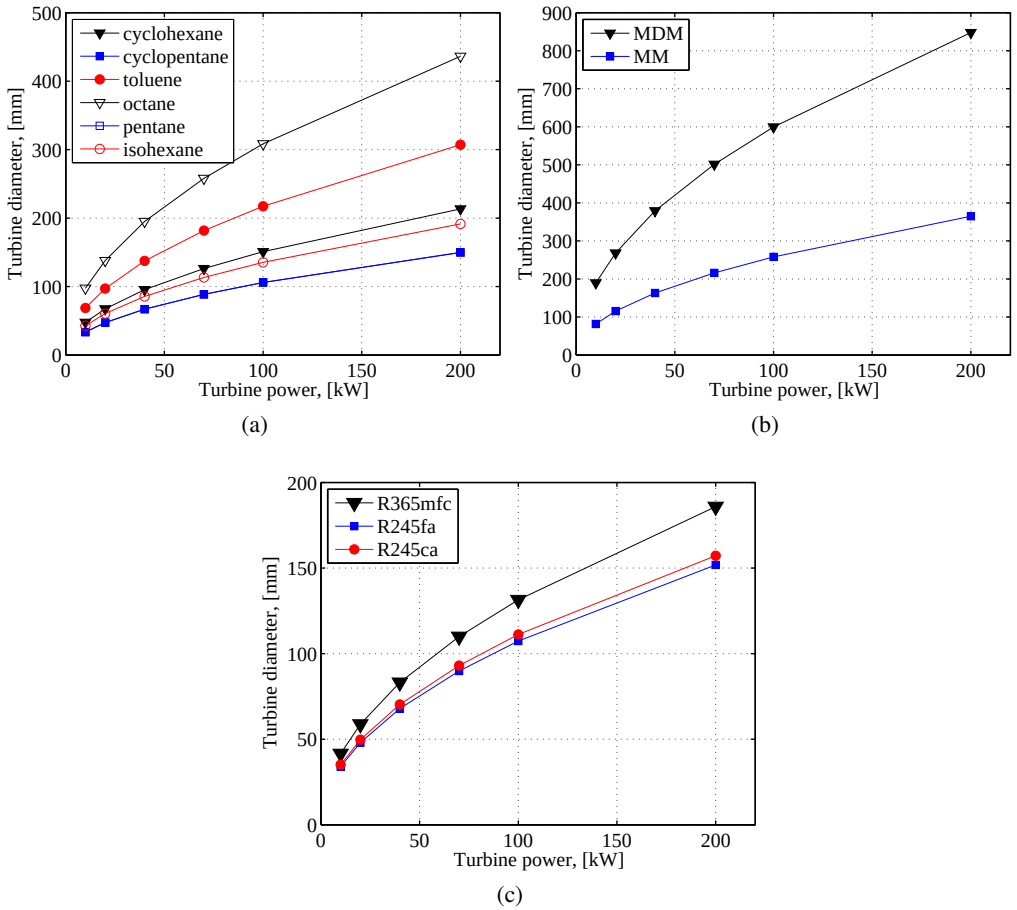

Figure 4.11: Turbine diameter as a function of turbine power with different (a) hydrocarbons, (b) siloxanes, and (c) fluorocarbons.

the stator outlet.

4.2.3 Effect of the turbine inlet pressure on the cycle efficiency and on the turbine design

The turbine inlet pressure of $p_{t,in}/p_{crit}$=0.8 was used to obtain the turbine design results presented in the previous sections and was evaluated to be a suitable method in the preliminary comparison of different working fluids in terms of a turbine design. The effect of the turbine inlet pressure on the turbine design is studied and discussed in this section because the turbine inlet pressure highly influences the expansion ratio and enthalpy change over the turbine, as well as the cycle mass flow rate. The turbine inlet pressure has also a singnificant effect on the cycle efficiency. The effect of turbine inlet pressure

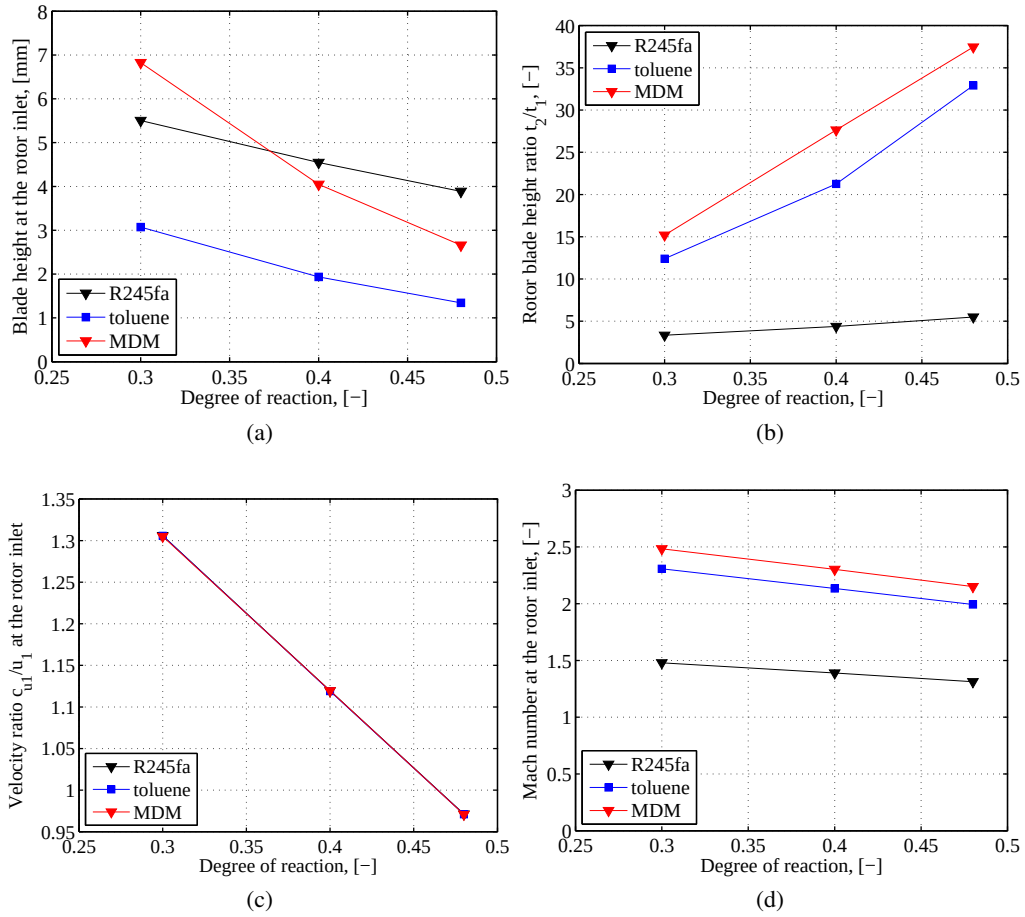

Figure 4.12: Effect of the degree of reaction on the turbine blade height at the rotor inlet (a), blade height ratio t_2/t_1 (b), velocity ratio c_{u1}/u_1 (c), and Mach number at the stator outlet (d). The turbine power is 100 kW in the calculated cases.

on the cycle efficiency with working fluids toluene, MDM, and R245fa is presented in Figure 4.13 showing that the higher the turbine inlet pressure, the higher the simulated cycle effciency.

The results of turbine diameter are presented in Figure 4.14a, the results of the blade height at the rotor inlet are presented Figure 4.14b, the results of the blade height ratio t_2/t_1 in Figure 4.14c, and the results of the rotational speed in Figure 4.14d. The turbine power is 100 kW in all the calculated cases. The results indicate that the lower the turbine inlet pressure, the higher the blade height at the rotor inlet, the larger the turbine wheel, and the lower the rotational speed of the turbine. In addition, when a lower turbine inlet pressure is selected, the rotor blade height ratio t_2/t_1 is lower. Thus, it can be estimated

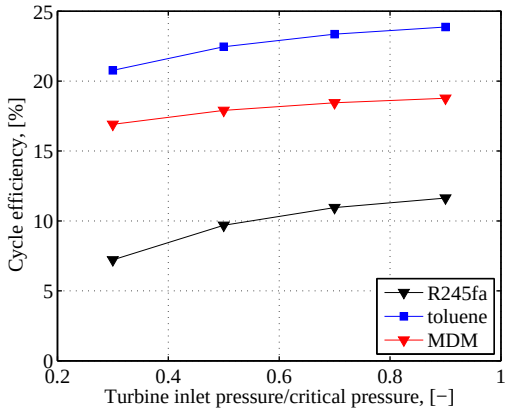

Figure 4.13: Cycle efficiency as a function of turbine inlet pressure.

that higher turbine efficiency could be achieved with radial turbines when a lower pressure ratio is adopted over the turbine when compared to higher pressure ratios. On the other hand, the increase in the turbine efficiency should justify the lower cycle efficiency caused by the use of lower turbine inlet pressure. It is recommended to take into account both the thermodynamic cycle performance and the turbine design considerations when selecting the operational parameters and working fluid for the cycle.

4.3 Conclusions and discussion

The aim of this chapter was to investigate and highlight the specific features related to the selection of the working fluids for ORC power systems from different working fluid groups that have been identified as suitable candidates for ORC systems and to study the preliminary design of small-scale turbines with different working fluids. The results show that the most important working fluid properties and ORC process parameters, namely the evaporating and condensing pressure, cycle efficiency, enthalpy change, and the expansion ratio over the turbine, are closely related to the group of the working fluid as well as to the critical temperature of the fluid. In general, when comparing different fluids of the same working fluid group, the higher the critical temperature of the fluid, the higher the obtainable process efficiency. On the contrary, the high critical temperature leads to a high expansion ratio over the turbine and to low condensing pressures, especially with siloxanes and heavy hydrocarbons, which are influential parameters on the process heat exchanger and expander design. The following conclusions were made based on the thermodynamic analysis.

-Hydrocarbons: 1) High cycle efficiency can be obtained with the high critical temperature and high molecular weight fluids. 2) Higher condensing pressures and lower expansion ratios over the turbine are obtained when adopting lower critical temperature fluids, compared to the higher critical temperature hydrocarbons. 3) Higher enthalpy drop over the turbine is obtained when compared to a siloxane or a fluorocarbon having a compa-

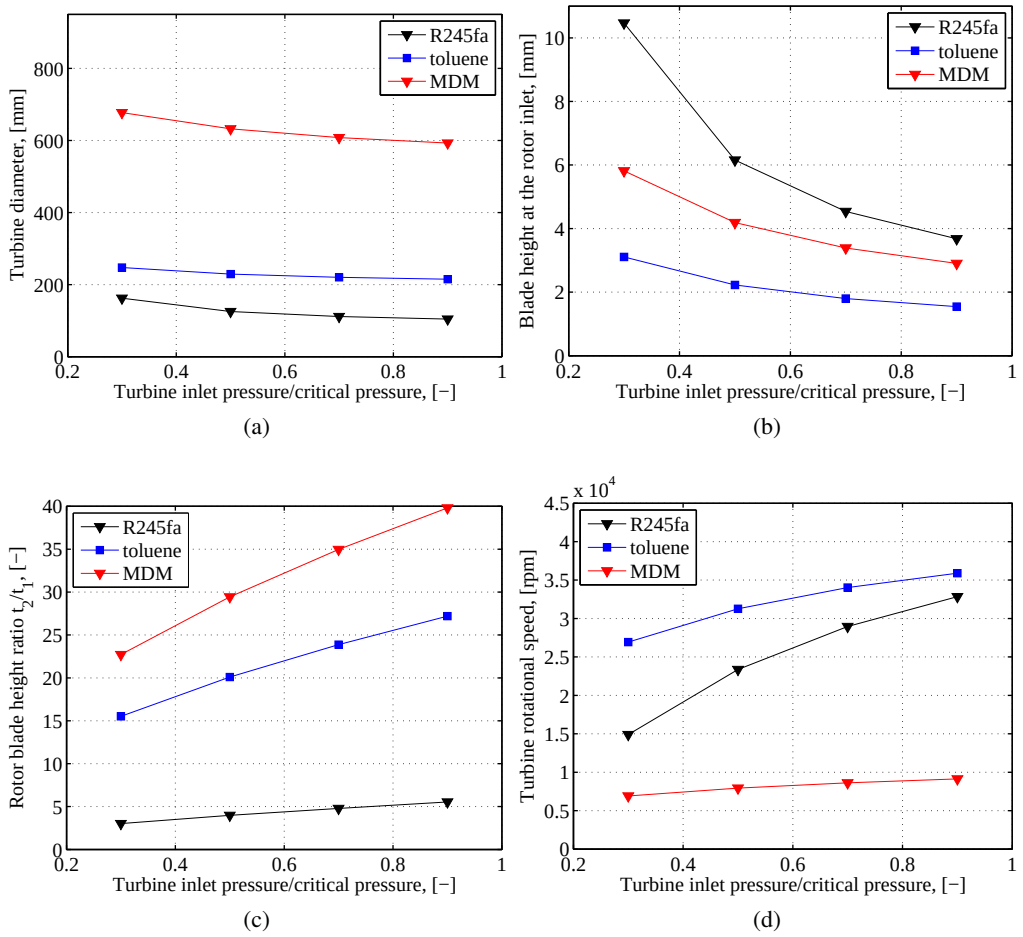

Figure 4.14: Effect of the turbine inlet pressure on the turbine diameter (a), blade height at the rotor inlet (b), blade height ratio t_2/t_1 (c), and turbine rotational speed (d). The turbine power is 100 kW in the calculated cases.

rably similar critical temperature. 4) Cycloalkanes and aromatic hydrocarbons represent higher efficiencies when compared to a linear hydrocarbon having a relatively similar critical temperature.

-Siloxanes: 1) High cycle efficiencies can be achieved when a fluid with a high critical temperature and recuperated cycle is used. 2) High expansion ratios and low condensing pressures are obtained in applications having a relatively low condensing temperature. 3) The enthalpy drop over the turbine is lower when compared to hydrocarbons. 4) Relatively small differences in the cycle performance and process design parameters were observed when comparing a cyclic and a linear siloxane with a comparably similar criti-

cal temperature.

-Fluorocarbons: 1) Comparably similar cycle efficiencies are obtained when comparing a fluorocarbon and hydrocarbon having comparably similar critical temperature. 2) A higher condensing pressure and a lower expansion ratio over the turbine is obtained when comparing a fluorocarbon and hydrocarbon having comparably similar critical temperature. 3) A lower enthalpy drop over the turbine is obtained when compared to the hydrocarbons.

The turbine design calculations were coupled together with the thermodynamic process design tool. As a result, a preliminary assessment on the design of supersonic radial turbines for the power level from 10 kW to 200 kW was carried out with six hydrocarbons, two siloxanes, and three fluorocarbons. The turbine main dimension and rotational speed as a function of turbine power level were solved by using a comprehensive comparison based on the use of nondimensional parameter specific speed. The studied siloxanes represented larger turbine wheels and lower rotational speeds than the fluids from other fluid groups. The largest blade heights are obtained with the studied fluorocarbons and siloxanes. In general, the results indicate that the design of ORC turbines with a very low power output is difficult, because the turbine wheels tend to be small and fast rotating and especially due to the small blade height at the turbine rotor inlet. The small blade height at the rotor inlet is estimated to lead to difficulties in manufacturing the turbine flow channels, as well as is estimated to lead to reductions in the turbine efficiency, caused by a tip clearance loss and relatively thick boundary layers when compared to the height of the flow channel. In addition, with fluids having the highest expansion ratios a significantly large blade height ratio between the rotor inlet and outlet was observed and might lead to efficiency reductions due to flow separation in the rotor. Thus, the use of multistage turbines could be considered with these fluids. The high rotational speeds over about 100 000 rpm are estimated to lead to practical difficulties in the design of the turbogenerator shaft, generator, and bearings.

The results indicated that by selecting a low degree of reaction or low turbine inlet pressure, larger blade heights were obtained at the turbine inlet. However, the low degree of reaction leads to higher Mach number at the stator outlet, which increases losses, and the reduction in the turbine inlet pressure leads to lower cycle efficiency. As a conclusion, the selection of the working fluid highly influences not only the thermodynamic performance of the cycle, but in addition it has a significant impact on the turbine dimensions and rotational speed. Thus, it is recommended to take into account both the thermodynamic cycle performance and the turbine design considerations when selecting the operational parameters and working fluid for the cycle.

5 Siloxanes as working fluids in mini ORC systems

This chapter presents a study aimed at evaluating the use of siloxanes as the working fluid of a small-capacity (approximately 10 kW_e) ORC turbogenerator based on the "high-speed technology" concept, combining the turbine, pump, and electrical generator on one shaft, whereby the whole assembly is hermetically sealed, and the bearings are lubricated by the working fluid. The selected application for the ORC in this chapter is the exhaust gas heat from a turbocharged diesel engine having a shaft power output of approximately 120 kW. The application was identified as an interesting one for mini-scale ORC based on the literature and when taking into account the large number of small diesel engines installed in stationary and mobile applications worldwide. Siloxanes were identifed as potential candidates for mini-scale ORCs based on the results presented in Chapter 4 when both the thermodynamic process design and the turbine design were considered. The effects of adopting different siloxane working fluids on the thermodynamic cycle configuration, power output, and on the turbine and component design are studied by means of simulations. Toluene is included in the analysis as a reference fluid in order to make comparisons between siloxanes and a suitable hydrocarbon.

As was concluded based on the results presented in Chapter 4, one of the most challenging features when designing small-capacity ORC systems is the design of an efficient turbine. The turbine efficiency can vary widely, and it is affected by many factors, like the operational point, size, and turbine type. The maximum efficiency of the turbine is usually obtained using complex design techniques and turbine configurations, such as multistage turbines. From the economic point of view, it might be beneficial if the turbine had a relatively simple geometry especially in mini-scale ORC systems. However, the choice of the configuration is highly dependent on production economy and market conditions, as well as on the selected application. The sensitivity of the net power output to the turbine efficiency is therefore included in the analysis. A preliminary study on realizing a relatively efficient, simple, single-stage radial turbine with different working fluids and the preliminary design of turbine geometries for the selected application are presented and discussed in this chapter.

The diesel engine and exhaust gas parameters are presented in Table 5.1. The exhaust gas enters the evaporator at the temperature of $T_{\mathrm{hs,in}}$ = 431 °C, and it is cooled down to $T_{\mathrm{hs,out}}$ = 210 °C. The outlet exhaust gas temperature is selected based on the assumption that the sulfur content of the exhaust gas is high and that the acid dew point of sulfur occurs at the temperature of about 180 °C. A safety margin of 30 °C is adopted.

For the preliminary thermodynamic cycle analysis of the ORC system, the component efficiencies were set to specified fixed values for all selected working fluids in order to compare the thermodynamic cycle performance associated with the considered fluids. The main component efficiencies and process values used in the thermodynamic analysis are presented in Table5.2

Table 5.1: Diesel engine and exhaust gas parameters.

P_{sp} [kW]	$q_{\mathrm{m,hs}}$ [kg/s]	$T_{\mathrm{hs,in}}$ [°C]	$T_{\mathrm{hs,out}}$ [°C]	ϕ_{ev} [kW]	T_{ad} [°C]
120	0.227	431	210	55.4	180

Table 5.2: Component efficiencies and process specifications.

η_{t} [%]	η_{mg} [%]	η_{inv} [%]	η_{fp} [%]	$c_{\mathrm{t,out}}$ [m/s]	C_{d} [-]	T_{c}, Case1/Case2 [°C]	$T_{\mathrm{t,max}}$ [°C]	ΔT_{sh} [°C]	$\varepsilon_{\mathrm{max}}$ [-]
80	92	96.5	50	60	3.2	50/90	325	20	0.68

The cycle calculations were carried out by constraining the working fluid maximum temperature at the turbine inlet with $T_{\mathrm{t,max}} \leq 325$ °C, well below the fluids' thermal stability threshold (Colonna, 1991; Angelino and Invernizzi, 1993; Angelino and Colonna, 1998). The selected maximum temperature at the turbine inlet allows for the optimal coupling of the thermodynamic cycle and the heat source. Another constraint adopted in the calculations is that the temperature difference between the heat source fluid and the working fluid within the evaporator is not smaller than 20 °C. In most of the considered cases, the minimum temperature difference between the heat source and the working fluid occurs at the cold end of the evaporator. Here, the evaporator is assumed to feature countercurrent flow arrangement, and therefore, the cold end of the heat exchanger refers to the heat source fluid outlet and working fluid inlet. A small degree of superheating (ΔT_{sh} = 20 °C) is also specified as a safety margin to prevent liquid droplets from entering the turbine. An example of an evaporator temperature–transferred thermal power diagram is shown in Figure 5.1.

The thermodynamic cycle calculations are performed with the two condensing temperatures of T_{c} = 50 °C (Case1) and T_{c} = 90 °C (Case2). The ORC system is considered as a power-only application in Case1, and as a combined heat and power (CHP) application in Case2. A recuperator is employed to preheat the liquid working fluid entering the evaporator. The working fluid temperature at the recuperator outlet is calculated based on the turbine outlet temperature, feed-pump outlet temperature, and recuperator effectiveness. In this study, the maximum value of the recuperator effectiveness is limited to $\varepsilon_{\mathrm{max}} \leq$ 0.68, which enables the use of a recuperator, where the flow arrangement can also differ from the pure countercurrent flow configuration. However, lower recuperator effectiveness is specified in case of some of the working fluids considered here if the temperature difference at the evaporator cold end, between the heat source and working fluid, does not allow to obtain the maximum recuperator effectiveness. By varying the recuperator effectiveness, the heat rate to the ORC evaporator can be kept the same for each fluid. It would also be possible to set the maximum recuperator effectiveness for each fluid and vary the outlet temperature of the heat source. This approach would lead to slightly different

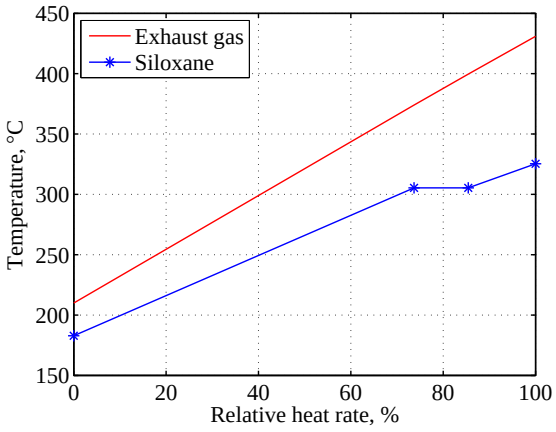

Figure 5.1: Temperature diagram of the evaporator. The working fluid is siloxane D_4.

results, especially for those fluids having the highest turbine outlet temperatures.

5.1 Results

5.1.1 Design point results

The values of the net electric power outputs, $P_{\mathrm{e,net}}$, and net electric efficiencies, $\eta_{\mathrm{e,net}}$, resulting from the cycle calculations are presented in Figure 5.2 and Figure 5.3. The results are presented for calculations with pressure losses(PL) and without pressure losses. Based on the results, the electric power output calculated with siloxanes as working fluid, and by considering also the pressure losses, varies from 9.5 kW - 10.9 kW for Case1 (power-only application) and from 6.5 kW - 7.7 kW for Case2 (CHP application). In Case1, the lowest power output and efficiency are achieved with siloxane MM and the highest power output and efficiency with siloxane D_4. In Case2, the highest cycle performance is also achieved with siloxane D_4 while D_6 gives the lowest cycle performance. Relatively high cycle performance is achieved also with siloxanes D_5 and MD_2M. In both Case1 and Case2, the toluene process provides a higher power output (Case1 13.1 kW, Case2 10.5 kW) and efficiency (Case1 23.6 %, Case2 19.0 %) than the siloxane processes.

The results of Case1 and Case2 indicate that the condensation temperature has a significant impact on the cycle performance. Also the pressure losses between the turbine outlet and the condenser should be taken into account because the pressure losses raise the turbine outlet pressure and thus decrease the performance of the cycle. In turn, the pressure losses reduce the volume and pressure ratio over the turbine, which might have a positive impact on the turbine design. In these calculations, the turbine outlet velocity $w_{\mathrm{t,out}}$ was assumed to be 60 m/s in each case. A more accurate pressure loss evaluation can be performed after the turbine outlet velocity and component geometries are known.

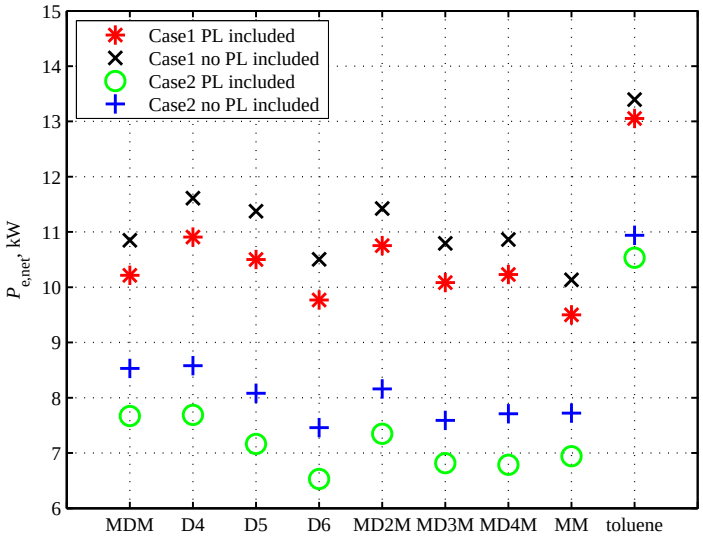

Figure 5.2: ORC process net electric power, $P_{\mathrm{e,net}}$.

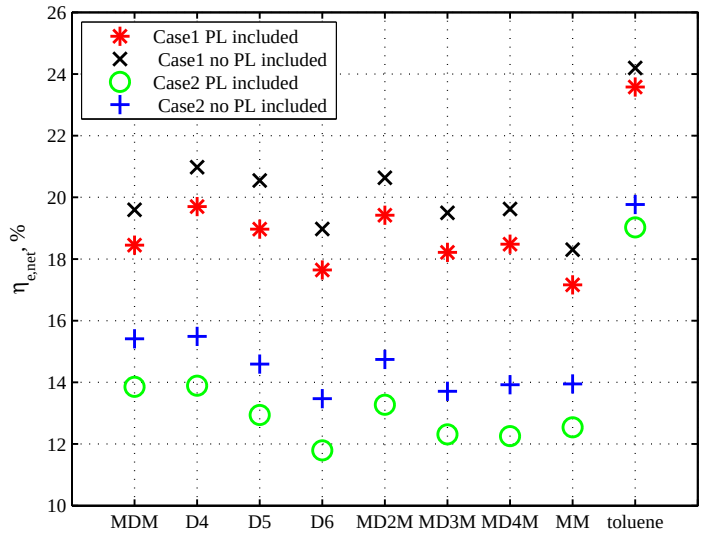

Figure 5.3: ORC process net electric efficiency, $\eta_{\mathrm{e,net}}$.

The enthalpy drop over the turbine, working fluid mass flow rate, volume flow at the turbine outlet, and recuperator effectiveness associated with the various working fluids are presented in Table 5.3. The fluid state at the turbine inlet and the condensation pressure at the corresponding condensation temperature of 50 °C (Case1) and 90 °C (Case2) are shown in Table 5.4.

Table 5.3: Working fluid mass flow rate, volumetric flow rate, specific enthalpy drop over the expansion, and recuperator effectiveness, for the studied working fluids.

	Case1				Case2			
	$q_{\mathrm{m,wf}}$ [kg/s]	$q_{\mathrm{v,out}}$ [m^3/s]	Δh_{t} [kJ/kg]	ε [-]	$q_{\mathrm{m,wf}}$ [kg/s]	$q_{\mathrm{v,out}}$ [m^3/s]	Δh_{t} [kJ/kg]	ε [-]
MM	0.148	0.16	81.1	0.68	0.174	0.04	53.5	0.68
MDM	0.149	0.84	83.6	0.68	0.169	0.16	57.3	0.66
MD_2M	0.152	4.07	84.5	0.68	0.152	0.47	59.3	0.54
MD_3M	0.147	18.84	80.6	0.64	0.147	1.38	55.6	0.51
MD_4M	0.154	88.95	77.6	0.62	0.154	3.84	52.3	0.49
D_4	0.161	2.10	82.0	0.68	0.167	0.28	57.3	0.57
D_5	0.165	7.20	75.3	0.65	0.165	0.71	52.5	0.51
D_6	0.158	30.57	72.6	0.62	0.158	1.89	49.4	0.49
toluene	0.087	0.25	183.2	0.68	0.099	0.07	135.2	0.68

Table 5.4: Working fluid state at the turbine inlet, and condensation pressures for Case1 and Case2.

				Case1		Case2	
	$p_{\mathrm{t,in}}$ [bar]	$T_{\mathrm{t,in}}$ [°C]	$p_{\mathrm{t,in}}/p_{\mathrm{cr}}$ [-]	p_{c} [bar]	$p_{\mathrm{t,in}}/p_{\mathrm{c}}$ [-]	p_{c} [bar]	$p_{\mathrm{t,in}}/p_{\mathrm{c}}$ [-]
MM	18.50	263	0.95	0.175	106	0.743	25
MDM	12.00	300	0.85	0.022	548	0.137	88
MD_2M	8.75	325	0.71	0.003	2674	0.029	299
MD_3M	4.40	325	0.46	0.0005	8395	0.007	641
MD_4M	2.55	325	0.29	0.0001	26410	0.002	1425
D_4	11.85	325	0.89	0.007	1695	0.056	210
D_5	6.20	325	0.53	0.002	4050	0.016	396
D_6	3.30	325	0.34	0.0003	11698	0.004	820
toluene	34.7	325	0.84	0.123	282.4	0.543	64

For siloxanes, the enthalpy drop over the turbine is comparably small, and varies from 73 kJ/kg to 85 kJ/kg for Case1 and from 49 kJ/kg to 59 kJ/kg for Case2. The enthalpy drop over the expansion affects the turbine design, leading to lower rotational speeds. A single-stage turbine can be considered, if the enthalpy drop over the turbine is small. For siloxanes, the mass flow rates vary from 0.14 kg/s to 0.17 kg/s. The enthalpy drop over the turbine is significantly higher with toluene (183 kJ/kg for Case1 and 135 kJ/kg for Case2) and the mass flow rate is lower than in the siloxane processes. MM, MDM, D_4 and toluene feature pressures relatively close to the critical pressure at the turbine inlet,

while MD_4M and D_6 provide relatively low pressures compared to the critical pressure.

The recuperator effectiveness varies from 0.49 to 0.68, in order to maintain sufficient temperature difference between the heat source and the working fluid. Siloxanes MD_4M and D_6, the fluids featuring the highest molecular weight, imply cycles with the smallest recuperator effectiveness, while fluids with low molecular weight, toluene and MM, entail cycles with the maximum recuperator effectiveness of 0.68, both for Case1 and Case2.

The volume flow rate at the turbine outlet is significantly high with siloxanes D_6, MD_3M, and MD_4M, having high molecular weights and critical temperatures, especially in Case1, where low condensation temperature is adopted. In order to achieve subsonic flow at the turbine outlet, a relatively large flow area would be needed. As can be noticed from the results, most of the selected working fluids demand for low values of the condensation pressures in both Case1 and Case2. The lowest practical limit for the pressure in the condenser is considered to be 0.03 bar - 0.05 bar, according to some previous studies concerning larger scale ORC systems (Angelino and Colonna, 1998; Fernàndez et.al, 2011; Drescher and Brüggemann, 2007). MM and toluene exhibit feasible condensation pressures, both in Case1 and Case2. Also MDM and D_4 processes feature feasible condenser pressures, with condensing temperatures typical of CHP applications. The use of the other siloxanes implies significantly lower condensing pressures and higher pressure ratios $p_\mathrm{t}/p_\mathrm{c}$ between the turbine inlet and the condenser. The high pressure ratio might have a negative impact on the design of efficient turbines if a single-stage turbine is considered. Low condensing pressure and high pressure ratio would lead to a complex turbine with multiple stages due to the large change in the flow area between the turbine inlet and outlet.

Based on the results from Case1 and Case2, toluene and siloxanes MDM and D_4 are considered as the most suitable fluids due to the high cycle efficiency and power output, and comparably high condensing pressure. Also siloxane MM can be considered as a suitable candidate due to the high condensing pressure and low process pressure ratio, but the efficiency and power output of the cycle is rather low compared to that obtained with other siloxanes, especially for Case1. It should be noted that these results are obtained based on the assumption that the turbine operates at a relatively high efficiency of 80 % with each selected fluid.

Siloxanes D_5, D_6, MD_2M, MD_3M, and MD_4M, with a high molecular weight and high critical temperature, have significantly low condensing pressures and high volume flow rates at the turbine outlet. These issues might lead to practical problems in the turbine and condenser design. These fluids can be considered more suitable in applications needing higher condensing temperatures than those selected in this study. In addition, the use of multistage turbines must be considered.

5.1.2 Effect of the condensing temperature on the cycle performance and process design

As shown by the results of Case1 and Case2, the low condensation temperature gives better cycle performance but leads to practical problems in the turbine and condenser design, due to the needed high degree of vacuum in the condenser and the high volume ratio over the turbine expansion. It is therefore essential to study the effect of different condensing temperatures on the previously mentioned parameters. The effect of the condensing temperature, ranging from 45 °C to 95 °C, on the cycle performance and component design with fluids MM, MDM, D_4, and toluene is studied and discussed in the following. The results presented in this section help in evaluating the suitable condenser temperature and comparing the cycle performance depending on various condensation temperatures. It should be noted that pressure losses are not included in the calculations. The effect of the condensation temperature, T_c, on the net electric power output, $P_{e,net}$ is presented in Figure 5.4a and on the net electric efficiency in Figure 5.4b.

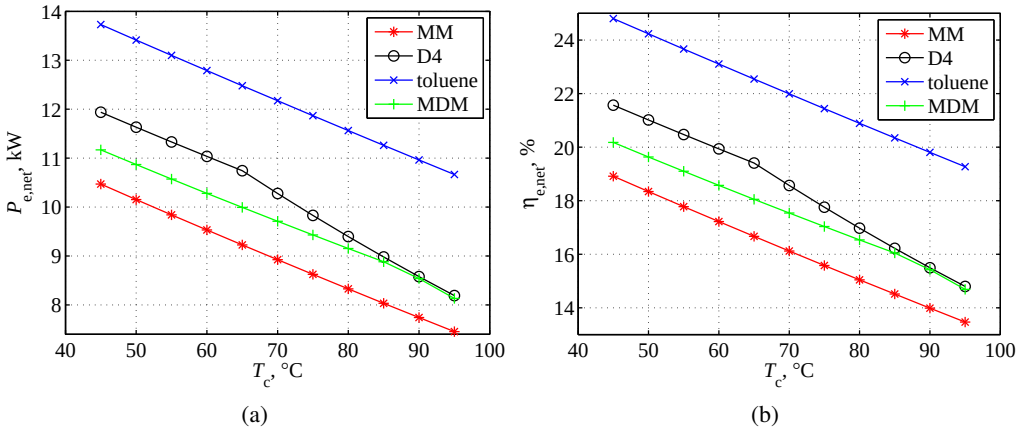

Figure 5.4: The effect of the condensation temperature, T_c, on the net electric power output, $P_{e,net}$ (a) and on the net electric efficiency, $\eta_{e,net}$ (b) (pressure losses are neglected).

Based on the results presented in Figure 5.4a and in Figure 5.4b, toluene gives the highest and MM the lowest power output and efficiency, with both high and low condensing temperatures. D_4 provides a higher performance than MDM with low temperatures in the condenser, but similar power outputs with high condensing temperatures. The net electric power output and efficiency display a linear trend as a function of the condensation temperature, if other process parameters are kept constant. In ORC processes with D_4 and MDM as working fluid, the increase in condensing temperature lowers the recuperator effectiveness, so that a sufficient temperature difference at the evaporator cold end is maintained. This causes a reduction in the system power output, especially with D_4, if high condensing temperatures are imposed. Figure 5.4a and Figure 5.4b show this effect,

resulting in the slope change, visible for the lines associated with siloxanes D_4 and MDM.

The effects of the condensing temperature on the volume ratio over the turbine expansion $v_{t,out}/v_{t,in}$, process pressure ratio p_t/p_c, and the condensing pressure are presented in Figure 5.5, a, b, and c.

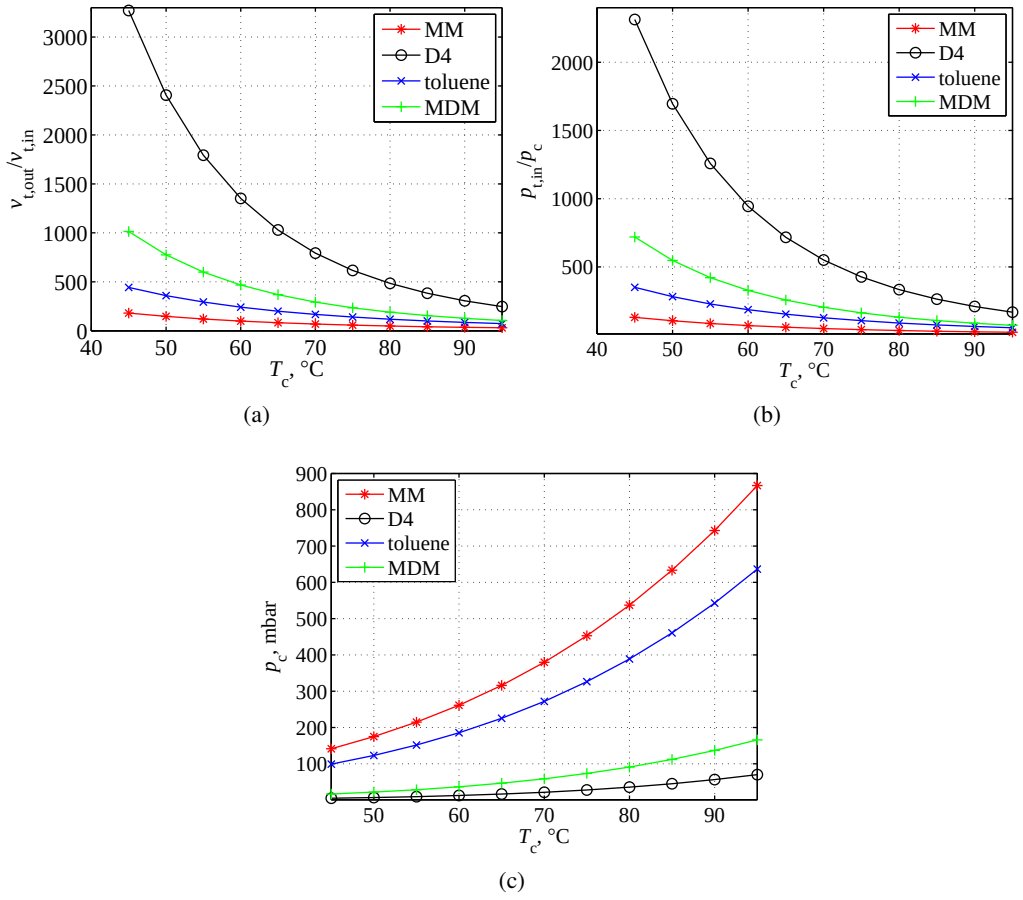

Figure 5.5: The effect of the condensing temperature, T_c on the turbine volume ratio $v_{t,out}/v_{t,in}$ (a), on the pressure ratio p_t/p_c (b), and on the condensing pressure, p_c (c).

As can be noticed from Figure 5.5a, Figure 5.5b and Figure 5.5c, the condensing temperature has a significant impact on the process volume ratio, pressure ratio, and condensing pressure. MM and toluene processes lead to relatively low volume and pressure ratios compared to D_4 and MDM at both high and low condensing temperatures. High volume ratio over the turbine might have a negative impact on the turbine design due to large change in the flow area needed between turbine inlet and outlet.

The condensing pressure calculated for the toluene and MM processes is above the considered minimum practical limit of 0.03 bar - 0.05 bar, at both high and low condensing temperatures. The condensing pressures are slightly below the mentioned technological limit if D_4 and MDM with low condensing temperatures are considered. High condensing temperature should therefore be selected with these two fluids. However, in small-capacity applications, it might be possible to adopt a slightly lower condenser pressure, due to smaller surfaces exposed to the pressure difference with the environment.

5.1.3 Turbine design considerations

In all the process calculations (Case1 and Case2), the turbine efficiency was assumed to be 80 %, independently of the working fluid. It should be noted that an isentropic turbine efficiency of 80 % might not be achievable with small-capacity turbomachinery, and that achieving high turbine efficiency with some of the selected fluids would require complex turbine geometries with multiple stages. It is therefore relevant to study the sensitivity of overall conversion efficiency depending on turbine efficiency. The effect of the turbine efficiency on the net electric power output for Case1 is presented in Figure 5.6.

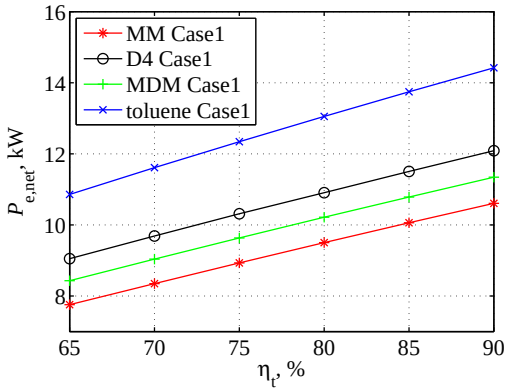

Figure 5.6: The effect of the turbine efficiency, η_{t} on the electric power output, $P_{\mathrm{e,net}}$.

As can be noticed from Figure 5.6, the net power output varies linearly with the turbine efficiency, if other process parameters are kept constant. High power outputs are achieved with toluene even with relatively low turbine efficiencies when compared to the selected siloxanes. The selection of the working fluid should be based on the overall performance, rather than solely on the optimization of the turbine efficiency. Small improvement in the turbine efficiency might not be economically feasible if more complex turbine geometry is required to achieve the increase in the turbine efficiency. Thus, the use of a simple turbine geometry might be well justified since the power output seems to be rather insensitive to small reductions in the turbine efficiency. However, it should be noted that with lower

turbine efficiencies the working fluid mass flow rate and the heat rate to the condenser is slightly higher, leading to larger heat transfer areas for the heat exchangers.

Preliminary and simplified single-stage radial turbine designs were performed, using the values from the process design calculations (Case1 and Case2) for MDM, D4, MM, and toluene. The main results are presented in Table 5.5. The turbine geometry was determined by assuming full-admission, by setting the turbine specific speed equal to 0.6 and by assuming the same isentropic enthalpy change over the rotor and stator leading to turbine design having a degree of reaction of about 0.5. The turbine diffuser was not accounted for in this preliminary turbine assessment.

Table 5.5: Main results of the preliminary radial turbine rotor design.

	MDM		D_4		MM		toluene	
	Case1	Case2	Case1	Case2	Case1	Case2	Case1	Case2
n [rpm]	36400	63400	22700	47200	82500	114000	119000	182300
D_{in} [mm]	156	74	243	99	67	40	71	40
$D_{\mathrm{out,tip}}$ [mm]	109	52	170	69	47	28	50	28
$t_{\mathrm{in,rot}}$ [mm]	1.2	1.4	1.1	1.3	1.1	1.3	0.7	0.8
$t_{\mathrm{out,rot}}$ [mm]	37.1	17.6	57.8	23.6	15.9	9.4	16.9	9.5
P_{t} [kW]	12.4	9.7	13.2	9.6	12.0	9.3	16.0	13.3

As was shown in Table 5.5, comparably larger rotor wheel diameters, larger blade heights at the rotor outlet, and lower rotational speeds are achieved with fluids MDM and D_4, which have a high molecular weight. Comparably smaller wheel diameters and higher rotational speeds are required with toluene and MM, having lower molecular weights than D_4 and MDM.

As can be noticed from Table5.5, the blade heights at the rotor inlet are significantly small with all the selected fluids. Toluene requires the smallest blade height, between 0.7 mm - 0.8 mm, while MDM allows for the largest blade height, between 1.2 mm - 1.4 mm. A small blade height in the turbine stator and rotor inlet might lead to low turbine efficiencies and practical problems in turbine manufacturing and operation. To increase the blade height at the rotor inlet and in the stator, lower turbine inlet pressures, lower degree of reaction, or partial admission turbines could be considered. However, the lower turbine inlet pressure would lead to lower cycle efficiency, lower degree of reaction would lead to higher Mach number at the rotor inlet, which would lower the efficiency, and in general, partial admission turbines represent lower effciency when compared to full admission turbines. The evaluation of the achievable turbine efficiency would require a more detailed analysis, due to the lack of practical experience with this type of small-capacity ORC turbomachinery.

A significant difference in the turbine geometry can be observed between the results of Case1 and Case2. Larger wheel diameters and lower rotational speeds are achieved in Case1, where low condensing temperature of 50 °C is used. In Case2, where the higher condensing temperature of 90 °C is imposed, the turbine wheels are smaller and the rotational speeds are higher. The higher condensing temperature also results in a slight increase of the blade height at the rotor inlet.

5.2 Conclusions and discussion

The suitability of eight siloxanes as working fluids for a small-capacity ORC system based on high-speed turbogenerator technology is presented and analyzed. Toluene is included in the analysis as a reference fluid to make comparisons between siloxanes and a suitable hydrocarbon having a lower molecular weight than siloxanes. The considered application is the heat recovery from the high-temperature exhaust of a 120 kW turbocharged diesel engine. The thermodynamic process calculations were performed assuming a condensation temperature of 50 °C and also with an higher condensing temperature of 90 °C. The most suitable fluids were evaluated based on the net power output, condensing pressure, volume flow rate at the turbine outlet, and pressure ratio between the turbine inlet and condenser. Preliminary radial turbine designs were presented and analyzed for four selected fluids.

The highest simulated power output of 13.1 kW was achieved with toluene. Among the siloxanes, D_4 gives the highest simulated power output of 10.9 kW. Comparably high conversion performances were achieved also with siloxanes D_5 and MD_2M. It should be noted that these results were obtained based on the assumption that the turbine operates at a relatively high efficiency of 80 % with each considered working fluid.

One remarkable feature is that siloxanes MD_2M, MD_3M, MD_4M, D_5, and D_6, having a high molecular weight, and therefore high values of critical temperature and low values of the critical pressure, demand for significantly low condensing pressures, which leads to high pressure and volume ratios over the turbine and to large volume flows at the turbine outlet. Based on the process calculations and on the turbine preliminary designs, as well as on the feasibility evaluation, D_4, MM, MDM, and toluene were considered as the most suitable working fluids.

The results show that the net electric power output of the analyzed small-capacity ORC systems is rather insensitive to small changes of the turbine isentropic efficiency. Therefore, the selection of the working fluid should be based on the optimization of the overall performance of the ORC system, rather than only on the optimal design of the turbine. The turbine type considered in this study was a single-stage full-admission radial turbine. The results from the preliminary radial turbine design calculations show that a larger wheel diameter, larger blade heights at the rotor outlet, and lower rotational speeds are achieved with fluids MDM and D_4, having relatively high molecular complexity. The use of toluene and MM as working fluids would require smaller turbines with high rotation

speeds (80 000 rpm-180 000 rpm). The blade heights at the rotor inlet are significantly small, 0.7 mm-1.4 mm with all the selected fluids, which might have a negative impact on the turbine efficiency, manufacturing, and operation. Lower turbine inlet pressures, lower degree of reaction, or partial-admission turbines should be considered in order to increase the blade height at the rotor inlet.

It should be noticed that the aim of this study was to provide preliminary information concerning the use of siloxanes as working fluids in small-capacity ORC turbogenerators. The evaluation of the achievable turbine efficiency and thus of the achievable power output of the ORC system would require experimental information on small ORC turbines, which is lacking at the moment.

6 Radial turbine design for a micro-ORC test setup

In this chapter, the design of a small-scale radial turbine designed for an ORC experimental setup based on high speed turbogenerator technology is presented and discussed. Based on the turbine design consideration and on the thermodynamic analysis for different fluids presented in the previous chapters, MDM was selected as the working fluid for an experimental setup, designed to recover exhaust gas heat from a diesel engine. The estimated power output of the turbine is about 13 kW and a high speed turbogenerator is used in the system. The selection of the working fluid was a compromise taking into account the cycle efficiency, process design, and turbine design. MDM was selected since it allows to design a turbine with a significantly lower rotational speed and larger turbine wheel, when compared to the hydrocarbons and fluorocarbons and siloxane MM. In addition, the blade height at the rotor inlet is higher with MDM when compared to the hydrocarbons. The disadvantages of using MDM as the working fluid are the relatively high expansion ratio over the turbine, which leads to a large variation on the rotor blade height between the rotor inlet and outlet; the high volumetric flow rate at the turbine outlet, which leads to the use of large sized heat exchangers and process piping at the low pressure side of the process; low speed of sound; and moderate cycle efficiency when compared to more complex siloxanes, such as D_4 or hydrocarbons, with a high critical temperature.

6.1 Design and flow analysis of the turbine

In this section, the design and CFD-simulation results for the turbine are presented. The simulations were performed for different stator and rotor geometries. The design data used as an input in the turbine design are presented in Table 6.1 and the main specifications of the designed turbine in Table 6.2. The velocity triangles obtained in the 1D turbine design at the turbine rotor inlet and rotor outlet are presented in Figure 6.1. The design was an iterative process in which several changes were made into the process design according to the changes made in the turbine design and the input data used in the turbine design was changed according to the changes made in the process design and mechanical design. The final turbine geometry was a compromise between the aerodynamic design and mechanical design, taking into account the limitation for mechanical stresses and vibrations, as well as the limitations for the axial force caused by the pressure difference over the turbine wheel. In addition, the process design set limitations, such as the condensing pressure, was limited to be above 0.03 bar. Thus, the turbine outlet pressure of 0.07 bar is used in the turbine design because slightly higher condensing temperature is adopted in the experimental setup when compared to the condensing temperature used in the Case1 in Chapter 5. In addition, the pressure losses between the turbine and the condenser increase the turbine outlet pressure and were taken into account in the turbine design. The degree of reaction lower than 0.5 and the turbine inlet pressure significantly lower than the fluids critical pressure were used in the final turbine design to increase the blade height at the rotor inlet and in the stator flow channels. In additon, the turbine rotor have curved blades at the rotor inlet instead of straight blades. The used turbine design

methods and the methods used in the CFD simulations are presented in more detail in Section 3.2 and Section 3.3.

Table 6.1: Design data used as an input in the turbine design.

Working fluid	MDM	
Working fluid mass flow rate	0.2 kg/s	
Estimated turbine power	13.0 kW	
	p [bar]	T [^{o}C]
Turbine inlet	7.9	265.3
Turbine outlet	0.07	218.7

Table 6.2: Main specifications of the designed turbine.

Evaluated turbine efficiency	76 %
Degree of reaction	0.39
Specific speed	0.49
Specific diameter	3.45
Rotational speed	31455 rpm
Rotor diameter	144 mm
Stator blade height	2 mm
Blade height at the rotor outlet	28.5 mm
Mach number at the rotor inlet	2.18
Relative Mach number at the rotor inlet	0.81
Flow angle at the rotor inlet	69.4 deg
Mach number at the rotor outlet	0.78

First, a working fluid expansion in a converging-diverging nozzle was studied in design and off-design conditions in order to study the design and fluid expansion in the converging-diverging part of the stator flow channel. In addition, these simulations were performed to test the implemented real gas model with supersonic flow and with a relatively simple geometry. Second, flow analyses of supersonic ORC stators are presented, and the results obtained by using different stator geometries are compared. The simulation results are presented for five different stator geometries having small variations in the nozzle setting angle as well as in the nozzle diverging part geometry and in the distance between the stator trailing edge and rotor blade leading edge. The flow field in one stator geometry was also simulated and studied in off-design conditions. The selected off-design conditions correspond to the cases where a lower heat rate is introduced to the ORC process. In off-design conditions adopting lower turbine inlet pressures, the working fluid mass flow rate is lower than in the design condition because of chocked flow conditions at the stator throat restrict the mass flow rate. Third, CFD-simulation results for

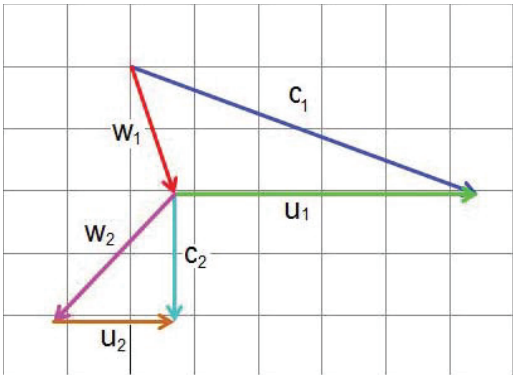

Figure 6.1: Velocity triangles of the designed turbine.

three slightly different turbine rotor geometries at the turbine design working condition are presented and discussed.

6.1.1 Expansion in a converging-diverging nozzle

The fluid expansion in one of the designed converging-diverging nozzles was studied by using turbine design and off-design conditions. These simulations were performed in order to study the expansion ratio over the convergent-divergent nozzle as well as the Mach number and the flow velocity at the nozzle outlet. The nozzle simulations were performed by using the $k-\omega$ SST-turbulence model. The velocity contours in the nozzle flow channel are presented in Figure 6.2. The main results obtained in the nozzle simulations are presented in Table 6.3. The pressure change and flow velocity in the mean line of the nozzle flow channel from the nozzle throat to the nozzle outlet are presented in Figure 6.3a and Figure 6.3b.

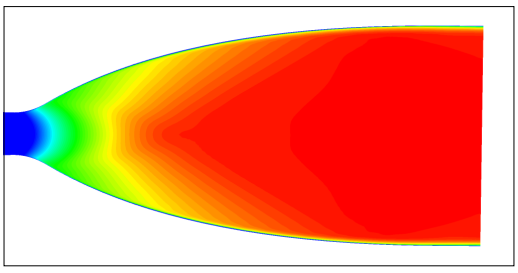

Figure 6.2: Velocity magnitude contours in the throat and in the diverging part of the supersonic nozzle.

As presented in Table 6.3 and in Figure 6.3a and Figure 6.3b, the pressure ratio over the nozzle and the outlet Mach number are slightly higher in off-design conditions than in the

Table 6.3: Nozzle simulation results.

Case	p_{in}, [bar]	p_{in}/p_{out}, [-]	$q_m/q_{m,des}$, [-]	c_{out}, [m/s]	Ma, [-]
design point	7.6	19.5	1.00	312.0	2.36
80 % off-design	6.0	19.9	0.79	311.3	2.37
60 % off-design	4.6	20.2	0.61	309.3	2.39

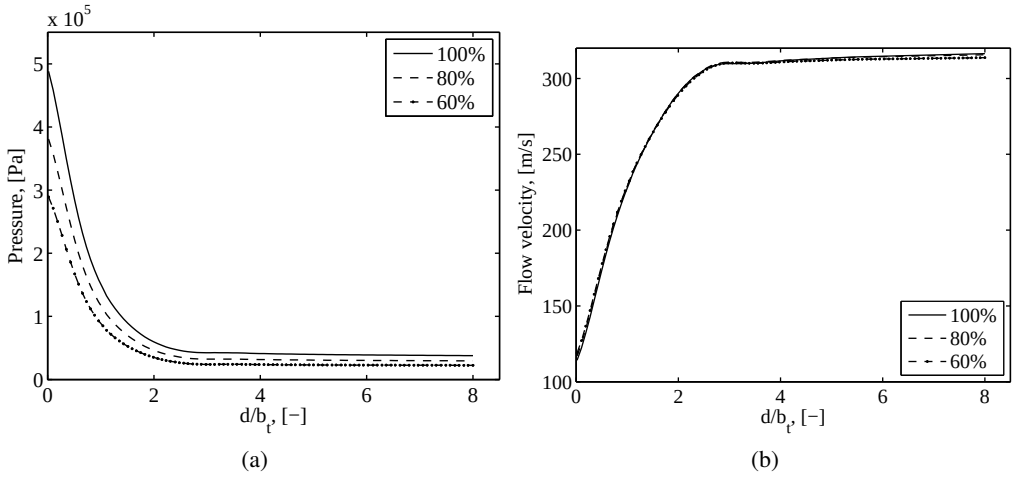

Figure 6.3: Static pressure change (a) and velocity magnitude (b) along the mean line of the nozzle divergent section at design conditions and at 80% and 60% off-design conditions.

design condition. The simulated nozzle outlet velocity is slightly lower in the off-design conditions compared to the simulated result of design point. In general, the simulation results indicated that the real gas model was successfully implemented in the flow solver and uniform velocity and Mach number distribution were achieved at the nozzle outlet.

6.1.2 Stator simulations

Different supersonic stator geometries were designed and simulated at the turbine design conditions and the results obtained with different geometries were compared to the results of 1D-turbine design values. The simulations were performed by using Chien's $k-\epsilon$ and $k-\omega$ SST-turbulence models. The results obtained with the two different turbulence models were presented and compared. In addition, one of the designed stator geometry was studied at off-design working conditions by using $k-\omega$ SST-turbulence model in the simulations.

The computational grid dependency was studied with one of the designed stator geometries in order to minimize the error in the simulation results due to grid spacing. The solutions were computed for the stator flow channel geometry with three different struc-

tured grids: coarse grid having 6 480 cells, medium grid having 27 648 cells, and dense grid having 55 728 cells. The simulations were performed by using $k-\omega$ SST-turbulence model. The grid dependency is assessed by monitoring two parameters: the flow velocity in the mean line of the flow channel and the pressure distribution on the longer wall of the nozzle. Figure 6.4a presents the results of flow velocity in the mean line of the flow channel and Figure 6.4b the results of pressure distribution on the longer wall of the nozzle.

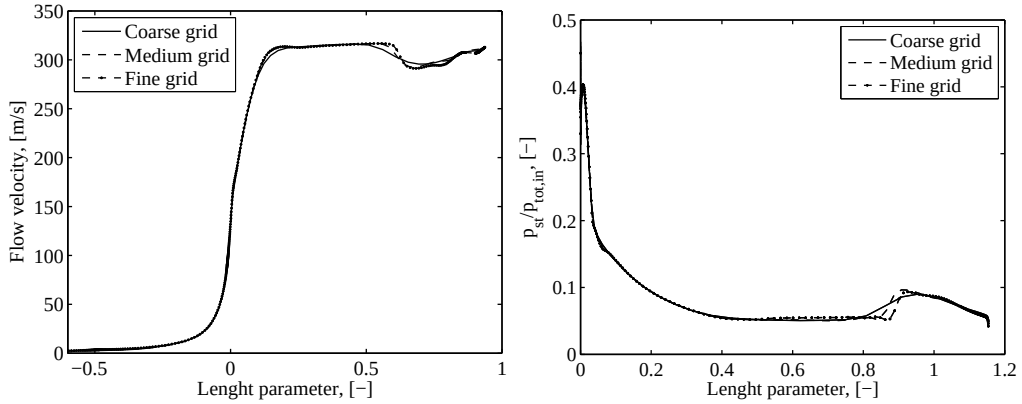

Figure 6.4: Grid dependency study. Flow velocity in the mean line of the flow channel (a) and pressure distribution on the longer wall of the nozzle (b).

The results show that the velocity magnitude and pressure distribution agree reasonably well when using medium and fine grid, and the solution is close to grid independency when using medium and fine grid. The general shape of the pressure peak, in a location where an oblique shock wave from blade trailing edge hits the longer wall, is similar between the two densest grids even if the position is slightly different. This difference is considered to be acceptable, and hence, results calculated with the same grid but at different operating conditions can be compared. Therefore, computational grids having the number of cells comparable to the number off cells used in the medium grid were used in the simulations for the studied stator geometries presented in the following sections.

Different stator geometries having a similar throat width and blade height were simulated in turbine design operation conditions. The studied geometries represent slightly different nozzle setting angles, distances between the stator and rotor, and slightly different shapes of the diverging part of the nozzle. The design condition results for the studied stator geometries are presented in Table 6.4. In general, the simulated results show reasonably good agreement with the results obtained in the 1D turbine stator design. The stator outlet velocity and the Mach number predicted in the CFD simulations are slightly higher than the values used in the turbine 1D design. Based on the results presented in Table 6.4, the $k-\omega$ SST-turbulence model predicts higher flow outlet velocities when

Table 6.4: Stator simulation results with different stator geometries

Case		p_{in} [bar]	p_t [bar]	p_{out} [bar]	c_{out} [m/s]	Ma [-]	α_{out} [deg]	η_{tot-st} -η_{rel}, [%]
1D design		7.9	5.1	0.4	289.7	2.18	69.4	0
Geometry 1	$k-\omega$ SST	7.6	4.5	0.38	309.3	2.33	71.1	+ 11.1
Geometry 1	$k-\epsilon$	7.6	4.5	0.38	292.6	2.17	69.8	+ 0.7
Geometry 2	$k-\omega$ SST	7.6	4.5	0.40	304.5	2.30	71.7	+ 9.8
Geometry 2	$k-\epsilon$	7.6	4.5	0.41	297.9	2.23	71.8	+ 6.6
Geometry 3	$k-\omega$ SST	7.6	5.0	0.41	300.9	2.27	71.7	+ 8.1
Geometry 3	$k-\epsilon$	7.6	5.0	0.41	295.9	2.22	71.6	+ 5.4
Geometry 4	$k-\omega$ SST	7.7	4.5	0.40	306.8	2.32	71.9	+ 11.1
Geometry 4	$k-\epsilon$	7.7	4.5	0.40	298.1	2.24	71.2	+ 5.7
Geometry 5	$k-\omega$ SST	7.8	5.0	0.43	305.7	2.31	73.1	+12.3
Geometry 5	$k-\epsilon$	7.8	5.0	0.43	300.8	2.27	73.1	+ 9.6

compared to the results obtained by using $k-\epsilon$-turbulence model. The inlet pressure ranges from 7.6 bar to 7.8 bar in the simulations while the inlet pressure used in the 1D turbine design was 7.9 bar. The CFD simulations predict slightly larger flow angles at the stator outlet when compared to the 1D design. The total-to-static state efficiency of the stator was calculated by using the area averaged velocity at the stator outlet, and the results shows that a higher effciciency is predicted by the CFD-simulations with all the studied geometries when compared to the estimation in the preliminary turbine design. The $k-\omega$-turbulence model predicts higher total-to-static efficiencies with all the studied geometries when compared to the results obtained by using the $k-\epsilon$-turbulence model. Experimental results are needed in order to further evaluate the accuracy of the used turbulence models. In general, only small differences in the obtained results can be observed when comparing the results obtained with stators in which the divergent section of the nozzle is not designed by using MOC (Geometry 1-Geometry 4) and the results obtained with a stator Geometry 5 adoptiong the nozzle divergent section designed by using MOC. It should be noted that the stator simulations do not take into account the losses related to the stator-rotor interaction(Rinaldi et al., 2013) and to the reflection of shock waves from the rotor blades, and thus, the actual efficiency of the stator is estimated to be slightly lower than the one predicted with steady CFD-simulations.

The studied stator geometries and the velocity contours obtained by using $k-\omega$ SST-Turbulence model are presented in Figures 6.5a-6.5e. Based on the results, all the studied geometries have a relatively similar flow field upstream the stator trailing edge. The most significant differences between the studied geometries can be obsereved in the direction of the shock waves and the viscous wake leaving from the trailing edge. The wakes and the oblique shock waves results in non-uniformity in the pressure, velocity magnitude, and flow angle at the stator outlet with all the studied geometries.

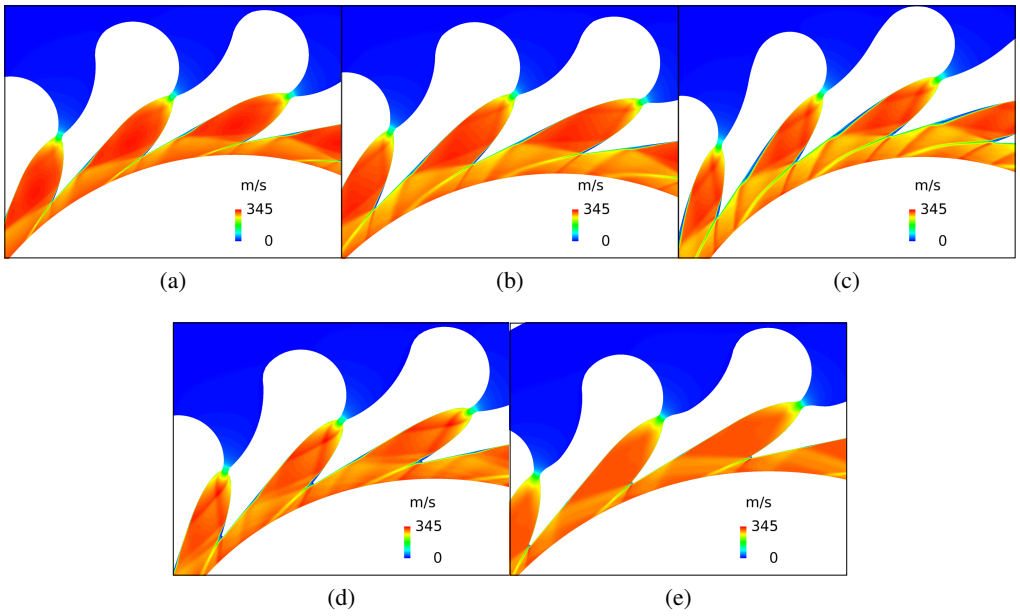

Figure 6.5: The studied stator geometries and the velocity magnitude contours predicted by using $k-\omega$ SST-Turbulence model: (a) Geometry 1, (b) Geometry 2, (c) Geometry 3, (d) Geometry 4, and (e) Geometry 5.

The simulation results for Geometry 5 are presented and discussed in more detail in the following. The pressure distribution on the long wall of the stator nozzle of Geometry 5 predicted by the two turbulence models are presented in Figure 6.6. The predicted velocity and pressure contours of Geometry 5 are presented in Figure 6.7 and Figure 6.8. The results of pressure distribution on the nozzle long wall indicate that both turbulence models predict similar shock wave locations, but slight differences can be noticed on the pressure peak presented in Figure 6.6. As it can be noticed from the velocity magnitude and pressure contours presented in Figure 6.7 and Figure 6.8, the stator blade trailing edge has a significant effect on the flow field at the stator outlet because of the occurrence of oblique shock waves and the presence of a viscous wake leaving the trailing edge. The oblique shock wave from the blade trailing edge is reflected from the nozzle longer wall further disturbing the flow. The $k-\epsilon$ turbulence model predicts slightly wider wake from the blade trailing edge and thicker boundary layer on the long wall of the nozzle, caused by the oblique shock wave from the blade trailing edge.

The velocity magnitude, speed of sound, and Mach number of the flow during the expansion of stator Geometry 5 are presented in Figure 6.9a and Figure 6.9b. As it can be observed from the results presented in Figure 6.9a and Figure 6.9b, the flow velocity increases rapidly after the nozzle throat section and decreases in a section where the oblique

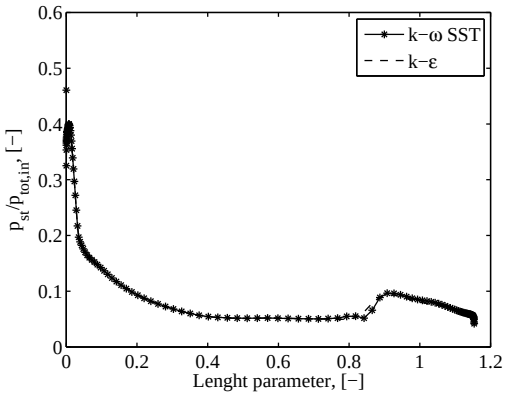

Figure 6.6: The results of pressure distribution on the nozzle long wall by using $k-\varepsilon$-turbulence model and $k-\omega$ SST-Turbulence model.

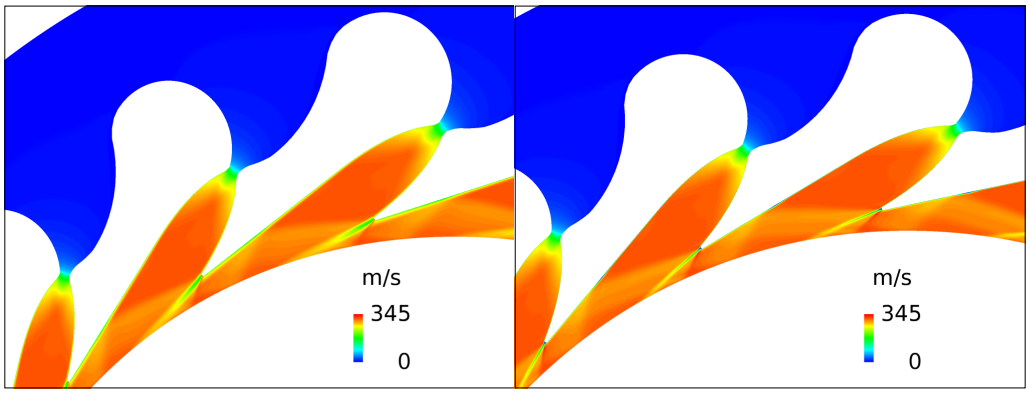

(a) (b)

Figure 6.7: Velocity magnitude in the stator:(a) $k-\varepsilon$-turbulence model and (b) $k-\omega$ SST-turbulence model.

shock waves and the viscous wake from the blade trailing edge affect the flow. The speed of sound of MDM increases near the throat section from 96 m/s to 132 m/s during the expansion. The increase in the speed of sound during the expansion, representing opposite behavior compared to an expansion when adopting ideal gas laws, can occur only for fluids having a high molecular complexity and if the expansion occurs in a certain thermodynamic region representing pressure or temperature relatively close to the fluids critical values (Harinck et al., 2009; Colonna and Guardone, 2006b). Similar results for the increase of the speed of sound of MDM were obtained by Colonna et al. (2006a) for expansion in a supersonic axial turbine stator with comparably similar turbine inlet state.

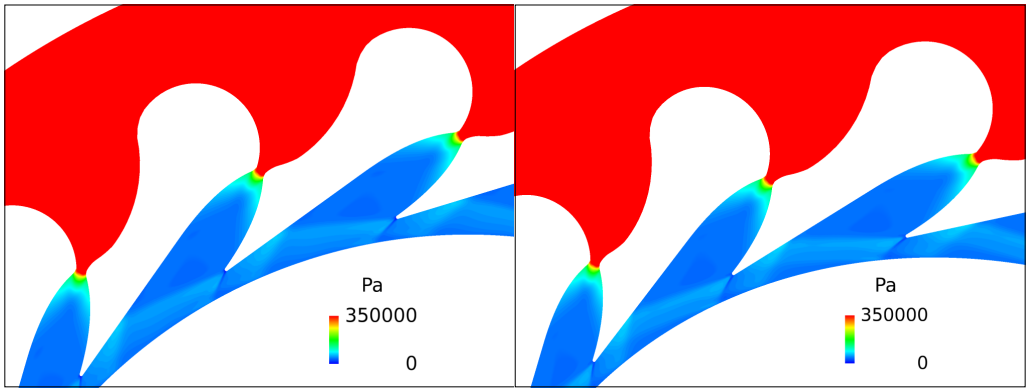

(a) (b)

Figure 6.8: Pressure distribution in the stator: (a) $k-\varepsilon$-turbulence model and (b) $k-\omega$ SST-turbulence model.

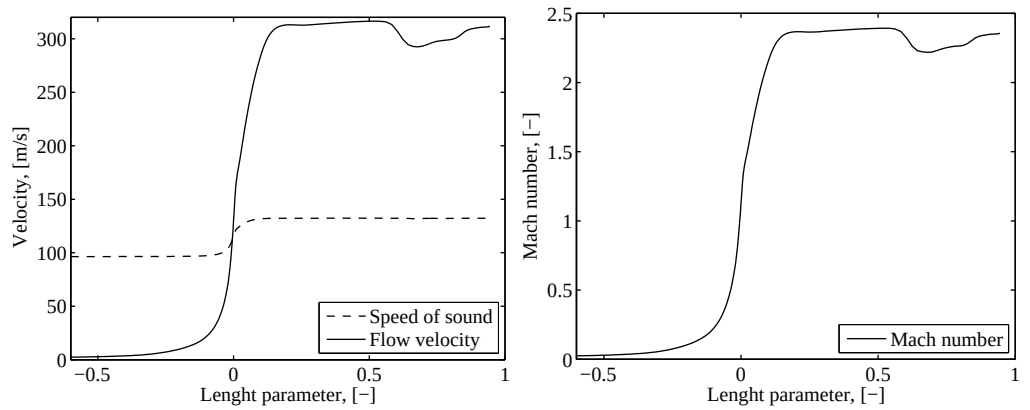

(a) (b)

Figure 6.9: Speed of sound and flow velocity (a) and Mach number (b) in the mean line of the stator flow channel, $k-\omega$ SST-turbulence model.

The flow field of the stator Geometry 5 was studied in off-design conditions by using $k-\omega$ SST-turbulence model. The area averaged results for flow field in the stator in 80 % and 60 % off-design conditions are presented in Table 6.5 and the contours of velocity magnitudes in Figure 6.10a and Figure 6.10b.

The pressure and velocity at the stator outlet and the pressure ratio of the stator are lower in the off-design conditions than in the design condition. It should be noted that the pressure ratio over the stator and the stator outlet velocity are lower when compared to the

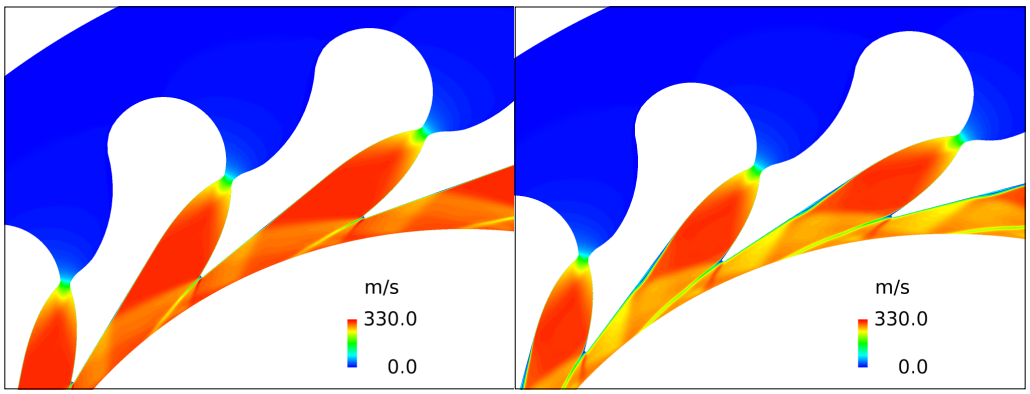

(a) (b)

Figure 6.10: Velocity magnitude at 80 % (a) and 60 % (b) off-design condition with $k-\omega$ SST-turbulence model.

Table 6.5: Stator off-design condition results.

Case	p_{in}, [bar]	p_{in}/p_{out}, [-]	$q_m/q_{m,des}$, [-]	c_{out}, [m/s]	Ma, [-]
80 % off-design	6.1	16.5	0.79	298.5	2.28
60 % off-design	4.5	12.4	0.61	274.8	2.12

results obtained in the nozzle simulations or in stator design condition simulations. This can be mainly explained by the occurrence of shock waves and by the presence of the viscous wake from the blade trailing edge as well as by the stator outlet pressure restricted by the turbine rotor. As it can be noticed from the velocity magnitude contours presented in Figure 6.10a and Figure 6.10b the viscous wake turns into more tangential direction in the off-design conditions. The results also indicate that the location of the shock wave hitting the long wall of the nozzle moves upstream in off-design conditions. This can be seen as a pressure rise on a nozzle long wall presented in Figure 6.11 presenting the pressure distribution on the nozzle long wall. In 60 % off-design condition, a flow separation is predicted to occur on the nozzle long wall and can be seen in the velocity magnitude distribution presented in Figure 6.10b. In Figure 6.10a and Figure 6.10b, a weak shock wave reflection from the outlet boundary can be seen, which has an effect on the predicted flow field near the stator outlet boundary.

The flow angle distribution at the stator outlet in design and off-design conditions is presented in Figure 6.12. Based on the results for flow angle distribution at the stator outlet, the stator exit flow angle is higher in off-design conditions and the fluctuation caused mainly by the two oblique shock waves in the flow angle increases in off-design conditions. This is important due to the large incidence and the large fluctuation of a flow angle

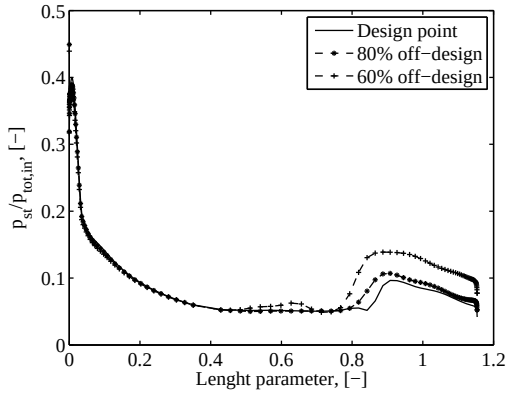

Figure 6.11: Pressure distribution on the long wall of the nozzle at 60 % and 80 % off-design conditions and at the design condition.

at rotor inlet might cause flow separation and low loading at the turbine rotor blades. The non-uniform flow field and high flow angles at off-design conditions should be taken into account when designing supersonic ORC turbines for applications having a non-constant heat rate to the process. The stator geometry could be improved in the future by bending and turning the stator blades as suggested by Harinck et al. (2013) to reach more uniform flow angle and velocity distribution at the stator outlet in design and off-design conditions.

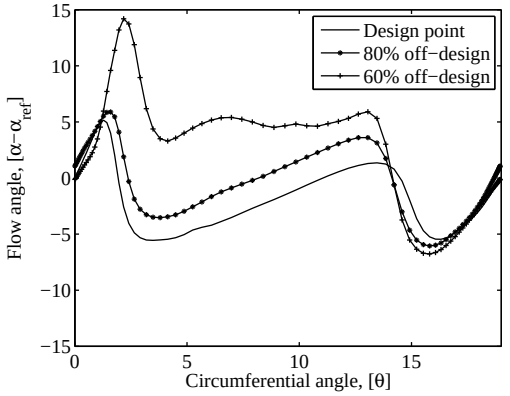

Figure 6.12: Flow angle (α) distribution at the stator outlet at 60 % and 80 % off-design conditions and at the design condition.

As discussed in the previous, the occurrence of oblique shock waves from stator blade trailing edge has a significant influence on the flow field. The position of the oblique shock wave was calculated analytically by using the theory from Anderson (1991) and compared to the results obtained in the CFD simulations. The CFD results of flow static

pressure, temperature, flow velocity, and Mach number in the nozzle before the oblique shock wave as well as the angle of the wake θ were used as the pre-shock state for the Hugoniot jump conditions for oblique shocks. CFD quantities are averaged over the nozzle section at the trailing edge. The shock wave angle β_1 from the trailing edge and the shock wave angle of the reflection from the long wall of the nozzle β_2 were obtained analytically and are presented in Table 6.6. The analytically solved shock wave and the wake positions are illustrated in Figure 6.13, and a comparison of the analytically solved shock wave directions and CFD results, for the stator design condition is presented in Figure 6.14.

Table 6.6: Wake angles and analytically solved shock wave angles.

Case	θ	β_1	β_2
design condition	8.5	30.3	23.9
80 % off-design	12.1	32.9	24.0
60 % off-design	16.2	35.9	24.7

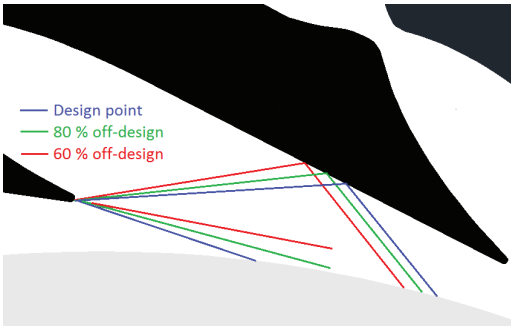

Figure 6.13: Analytically solved oblique shock wave directions and wake directions at 60 % and 80 % off-design conditions and at design condition.

The results obtained by using the analytical method for solving the direction of the oblique shock waves, agrees well with the results obtained by CFD showing similar behavior of the shock wave location hitting the longer wall of the nozzle moving upstream in off-design conditions. The difference between the results of the shock wave angles were estimated to be in the order of magnitude of 1-3 degrees when comparing the analytically solved results and the results obtained with CFD.

6.1.3 Rotor simulations

Three different rotor geometries with different blade angle distributions representing different meridional lengths of the flow passages but similar diameters, blade angles at the

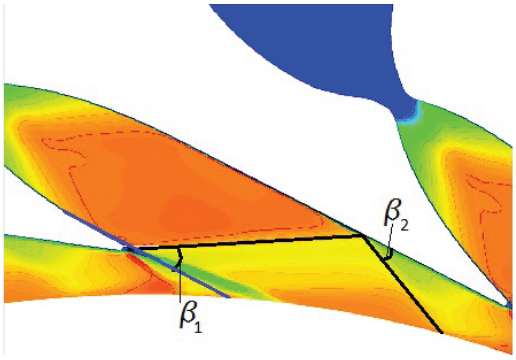

Figure 6.14: Analytically solved oblique shock wave directions compared to the CFD results at design condition.

rotor inlet and outlet, and blade heights were studied by means of CFD. The studied rotor geometries are presented in Figure 6.15, and the 3D geometries were generated by using a design tool for centrifugal impellers developed at LUT. The blade angle at the rotor inlet and the blade angles at the hub and shroud of the rotor outlet were determined based on the velocity triangles by using the angle of relative velocity. The blade angles, blade heights and rotor diameters were given as an input to generate the 3D geometries. The rotor simulations were performed by using the $k - \epsilon$ turbulence model. One rotor blade channel was modelled and grids having about 1 200 000 cells were used in these simulations for each geometry.

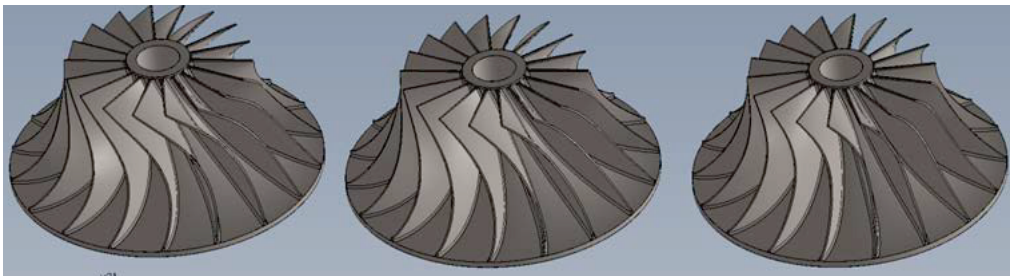

Figure 6.15: The studied rotor geometries: Geometry 1 is presented on the left, Geometry 2 is presented in the middle, and Geometry 3 is presented on the right.

The main CFD results for the different geometries are presented in Table 6.7. In general, there is a reasonably good agreement between the results obtained in the CFD simulations when compared to 1D turbine design values. Based on the results, the CFD simulations predict slightly higher pressure ratio over the rotor with all the studied geometries when compared to the pressure ratio evaluated in the turbine 1D design. In addition, the temperature drop in the turbine rotor is predicted to be higher in the CFD simulations when

Table 6.7: Rotor simulation results

Case	p_{in} [bar]	p_{in}/p_{out} [-]	ΔT_{rot} [^{o}C]	c_{in} [m/s]	Ma_c [-]	w_{in} [m/s]	Ma_w [-]	η_{st-st} -η_{rel}, [%]
1D design	0.40	6.2	12.7	289.7	2.18	107.4	0.81	0
CFD Geometry 1	0.42	8.6	19.4	240.4	1.81	98.4	0.74	+ 4.1
CFD Geometry 2	0.38	7.9	18.1	255.9	1.93	110.7	0.83	+ 1.4
CFD Geometry 3	0.37	7.0	16.2	253.8	1.91	114.16	0.86	+ 1.6

compared to the prediction of 1D turbine design. It should be noted that based on the simulated results, the rotor inlet velocity is lower at the rotor inlet when compared to the results obtained in the stator simulations as well as in the rotor 1D design. This has an effect on the predicted rotor flow field mainly due to the slight differences in flow angle and velocity triangle at the rotor inlet, when compared to 1D design and to the results obtained in the stator simulations. In addition, as presented in the stator simulations the flow angle distribution is non-uniform at the rotor inlet unlike the one that was used in the rotor simulations. The results indicate that the relative Mach number and relative velocity at the rotor inlet predicted in the CFD simulations agrees well with the 1D turbine design. A slightly higher rotor static to static state efficiency is predicted by the CFD-simulations when compared to the efficiency prediction used in the 1D turbine design. The CFD simulations do not take into account the rotor tip clearance loss or the losses related to the shock waves from the stator trailing edge causing flow separation at the rotor blades(Rinaldi et al., 2013) and thus, the rotor efficiency is estimated to be slightly lower than the one predicted in the CFD simulations.

The pressure distribution in the mean line of the rotor blade pressure and suction side are presented in Figure 6.16a, Figure 6.16b and Figure 6.16c. Based on the results, the location of the flow separation on the blade pressure and suction side can be observed as the increase in the static pressure in Figure 6.16a, Figure 6.16b and Figure 6.16c. An example of the simulated rotor static pressure, static temperature, and velocity contours of rotor Geometry 3 is presented in Figure 6.17a, Figure 6.17b and Figure 6.17c. Based on the simulated contours, a flow separation occurs at both the pressure side of the blade near the rotor inlet and especially at the blade suction side. The flow separation in the rotor flow channel can be clearly observed in Figure 6.17b as a region of higher temperature and in Figure 6.17c as a region of low flow velocity especially at the suction side of the blade. According to Rohlik (1975), the flow separation on the blade suction side can be prevented by increasing the number of blades and by optimizing the angle of the relative velocity. The flow separation on the pressure side of the rotor blade is estimated to be caused by the slightly incorrect flow velocity and absolute flow angle at the rotor inlet in the simulations, and thus, the relative flow angle differs from the 1D design as well. Based on the obtained results, it is recommended to make simulations in which the stator and rotor are coupled together to study the rotor inlet conditions in more detail. In addition,

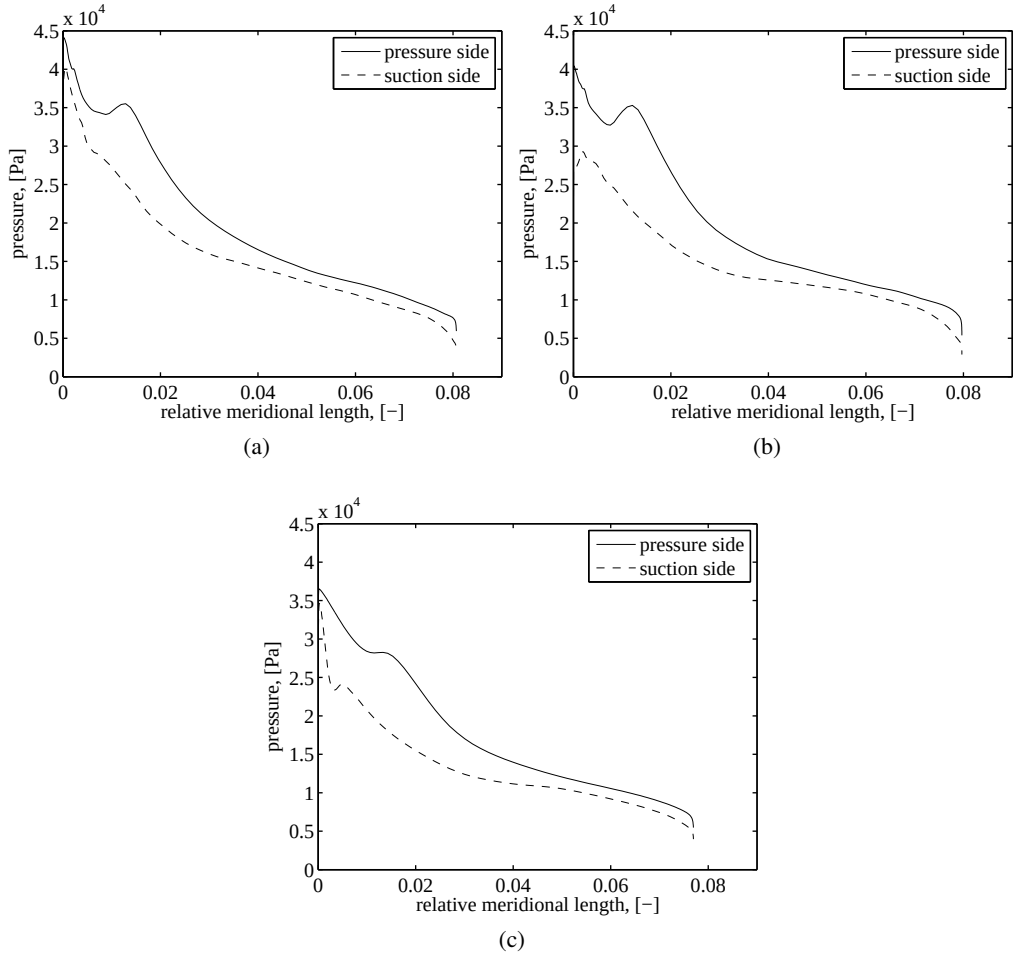

Figure 6.16: Simulated wall pressure on pressure and suction side with the studied rotor geometries, a) Geometry 1, b) Geometry 2, and c) Geometry 3.

the effect of the number of rotor blades and the effect of relative flow angle on the flow separation on the blade suction side should be studied in the future.

In general, there were difficulties in the rotor simulations mainly related to the convergence of the simulations and despite several efforts the rotor inlet conditions equal to the ones gained as a results in the stator simulations and used in the turbine 1D design were not reached. The rotor Geometry 2 was later selected for the experimental setup because it was evaluated as the most suitable geometry when evaluating the issues related to the mechanical design, such as vibrations and stresses.

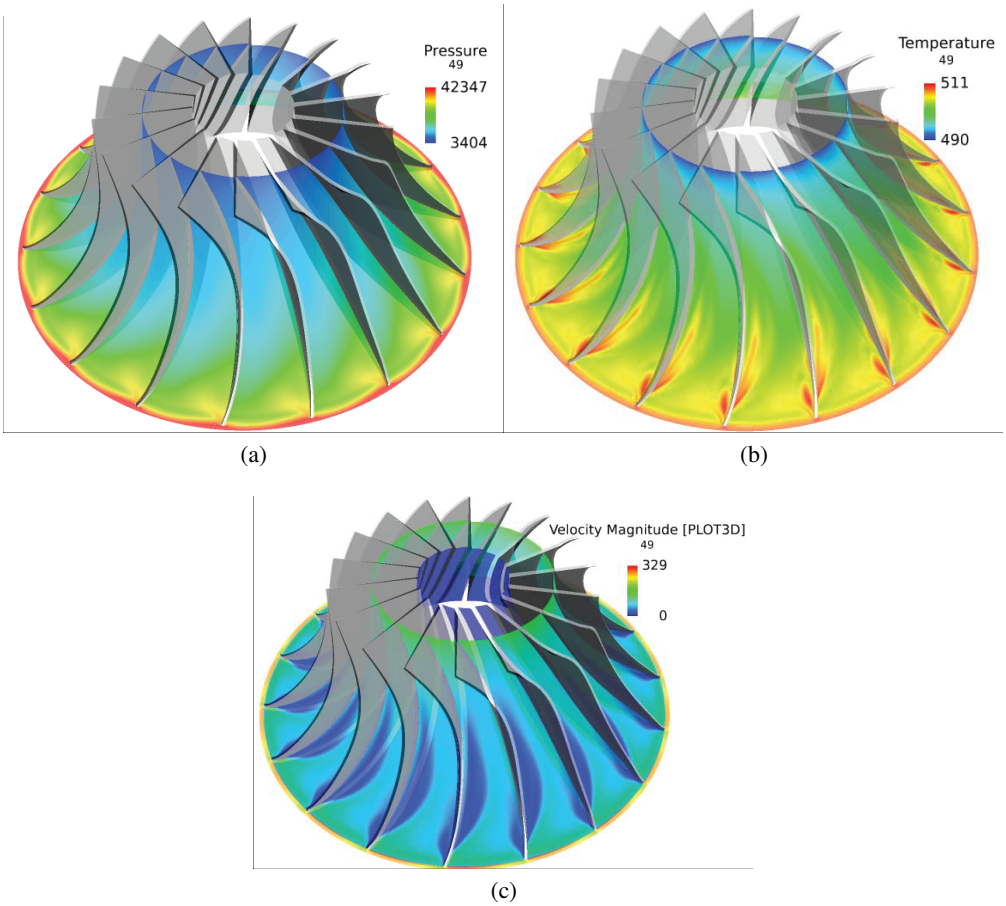

Figure 6.17: Example of simulation results of static pressure contours (a), static temperature contours (b) and velocity contours (c) of rotor Geometry 3.

6.2 Conclusions and discussion

The main results of the design and flow analysis of a turbine having a power output of about 13 kW and designed for an experimental setup adopting siloxane MDM as the working fluid was presented in more detail. The flow field in different stator geometries representing slightly different nozzle setting angles, distances between the stator and rotor, and slightly different shapes of the diverging part of the nozzle were predicted. In general, the results indicated that the designed stator geometries represented comparably similar results for pressure ratio, outlet velocity, and flow angle when compared to the results estimated in the 1D design. The results show that convergent divergent nozzles introduce uniform flow at the straight part of the nozzle in a region before the stator trailing edge. However, the stator blade trailing edge has a significant effect on the flow after the two oblique shock waves, their reflections, and the viscous wake. The shock waves

and viscous wake cause a non-uniform flow field and fluctuations on the flow angle at the stator exit. The flow expansion in one of the designed stator geometries was studied in off-design conditions corresponding to the cases when lower heat rate is introduced to the ORC process. The results show that the flow is more tangential in the off-design conditions and the fluctuation in the flow angle increases due to non-uniform flow field. This might cause flow separation and low loading at the turbine rotor blades in off-design conditions and is an important feature when designing supersonic ORC turbines for applications having a non-constant heat rate to the process.

Three different turbine rotor geometries were studied by means of CFD simulations. In general the results agreed relatively well with the results obtained in the 1D turbine design. The CFD simulations predicted slightly higher pressure ratio over the turbine and slightly higher efficinecy for all the studied geometries when compared to the rotor 1D design. In addition to the higher pressure ratios, the temperature drop in the turbine rotor is predicted to be higher by the CFD simulations when compared to estimation of 1D turbine design. A flow separation region at the rotor blade suction side was predicted with all the studied geometries. In addition, the angle of relative velocity at the rotor inlet and the flow velocity at the rotor inlet were slightly different when compared to the 1D design and the results obtained in stator simulations, causing flow separation at the blade pressure side at the rotor blade leading edge.

It is recommended to perform additional simulations in the future in which the stator and rotor are coupled together to study the rotor inlet conditions in more details. The turbine stator could be improved in the future by bending and turning the stator blades to reach more uniform flow angle and velocity distribution at the stator outlet in design and off-design conditions. In addition, the effect of the number of rotor blades and the effect of relative flow angle on the flow separation on the suction side of the rotor blade should be studied in the future. The flow field in the turbine rotor should be studied in off-design conditions as well. Unsteady simulations for similar turbines should be carried out in the future to study the loss mechanisms related to the interaction between the turbine stator and rotor blades. The performance of the designed turbine will be measured with experiments that will take place in 2014-2015 and the used design method will be validated based on the experimental results.

7 Waste heat recovery of large scale reciprocating engine

In this chapter, waste heat utilization in large-scale reciprocating engines is studied by means of thermodynamic analysis. In large reciprocating engines, the most significant waste heat stream can be identified as exhaust gas heat. There are also lower temperature waste heat streams, mainly heat in the pressurized charge air after the turbocharger, as well as heat in engine jacket cooling water and lubrication oil cooling circuit. The aim of this computational study is to investigate the potential of waste heat recovery from exhaust gases (EG) and charge air (CA) by means of ORC. Despite previous studies related to the utilization of waste heat of large-scale reciprocating engines, studies analyzing the possibility of utilizing the charge air heat are lacking at the moment. This study represents and discusses the possibility of replacing the charge air cooler (CAC) of a large turbocharged engine with an ORC evaporator, utilizing the heat from about 180 °C to 220 °C charge air in additional power production. Additionally, the aim is to study the overall power production improvement potential by means of heat recovery. The studied engine combined cycle is presented in Figure 7.1. The utilization of the heat from engine jacket water cooling and lubrication oil cooling was excluded from this study, due to the low temperature level of about 90 °C.

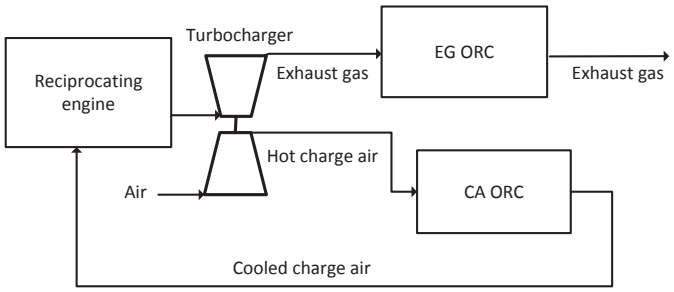

Figure 7.1: The principle of the studied engine combined cycle. Exhaust gases (EG) and charge air (CA) heat are utilized by means of ORC.

The ORC simulations were performed with several heat source temperatures, and the minimum pinch-point temperature difference in the ORC evaporator was limited to 15 °C, and a condensing temperature of 50 °C was used in most of the simulations. In addition, the effect of minimum pinch-point temperature difference in the evaporator, as well as the effect of condensing temperature on the process performance was included in the analysis. The evaporation pressure of the process was optimized based on the criteria that the minimum allowed pinch-point temperature difference in the evaporator was reached, or in case the temperature difference in the evaporator remained sufficient, the limit of $p_{\mathrm{ev}}/p_{\mathrm{cr}}$=0.95 was used for the evaporation pressure. The main process specifications and component efficiencies used in the thermodynamic analysis are shown in Table 7.1. Pressure losses were excluded from the thermodynamic analysis.

Table 7.1: Component efficiencies and process specifications used in the process calculations.

turbine isentropic efficiency	80	%
generator and mechanical efficiency	90	%
feed pump efficiency	60	%
feed pump motor efficiency	85	%
degree of superheating	10	°C
recuperator effectiveness	0.6	-
miscellaneous power consumption	2	%

Toluene, n-pentane, R245fa, and cyclohexane were selected as the working fluids. The fluid selection was based on the suitable thermodynamic characteristics of the fluids, including dry expansion in the turbine, relatively high cycle performance, and the critical temperature close to the studied waste heat source temperatures. A simplified feasibility evaluation was included by comparing the ratio of the theoretical heat transfer areas needed and the obtained power output of ORC processes, as suggested by Madhava Hettiarachchi et al. (2007). A case study of waste heat utilization for a 16.6 MW gas-fired engine was carried out. Finally, experimental results of charge air heat utilization are presented.

7.1 Results of thermodynamic analysis

7.1.1 Exhaust gas heat utilization

The exhaust gas heat utilization analysis was performed using exhaust gas temperatures of 300 °C, 350 °C, and 400 °C, typical for large-scale turbocharged engines. The results of the ORC process power outputs are presented in Figure 7.2a, Figure 7.2b and Figure 7.2c. The results indicate that the fluids with higher critical temperature, namely toluene and cyclohexane, represent a significantly higher performance than lower critical temperature fluids, n-pentane and R245fa. The highest power output $P_{\mathrm{e,net}}/q_{\mathrm{m,EG}}$ = 71.6 $kW/kg/s$ was achieved with toluene for EG inlet temperature of 400 °C and $P_{\mathrm{e,net}}/q_{\mathrm{m,EG}}$ = 51.8 $kW/kg/s$ and 34.8 $kW/kg/s$ with cyclohexane for EG inlet temperatures of 350 °C and 300 °C. As can be observed from the results, the obtained power output increases as the exhaust gas outlet temperature decreases or exhaust gas inlet temperature increases. This can be explained by a larger amount of heat utilized in the evaporator. The power outputs for the selected fluids represent a linear behavior with different exhaust gas outlet temperatures if a sufficient temperature difference is maintained in the evaporator with the highest allowed pressure $p_{\mathrm{ev}}/p_{\mathrm{cr}}$=0.95 of the fluid. With the exhaust gas inlet temperature of 300 °C or low exhaust gas outlet temperatures, the evaporation pressure has to be lowered with fluids toluene and cyclohexane, to maintain a sufficient temperature difference in the evaporator. This can be observed as a change in the slope of the curve in Figure 7.2a, Figure 7.2b and Figure 7.2c. The fluids with a high critical point, toluene and cyclohexane, can be better matched to the exhaust gas temperature than the fluids R245fa

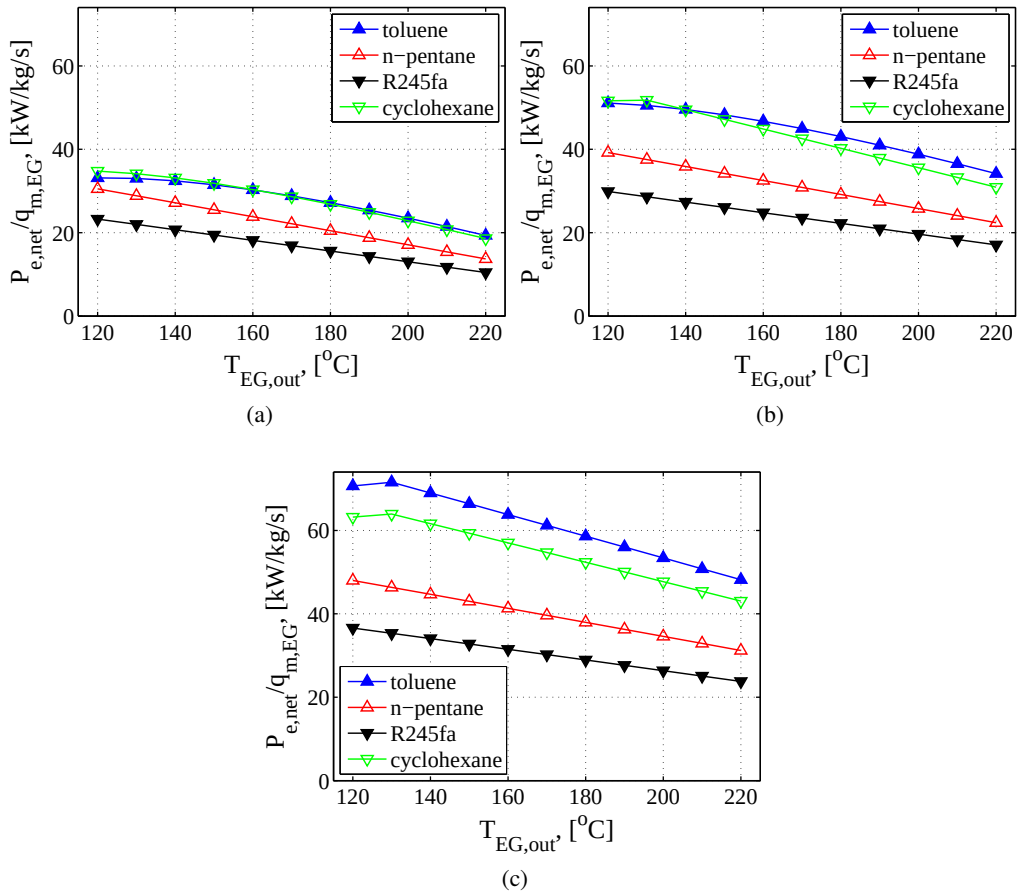

Figure 7.2: The effect of exhaust gas temperature at the outlet of the evaporator on the ratio of net power output to exhaust gas mass flow rate for different organic working fluids with exhaust gas inlet temperatures of (a) 300 °C, (b) 350 °C, and (c) 400 °C.

and n-pentane, which are restricted by the lower critical point. With reference to this, an example of the temperature profiles of the selected working fluids in the evaporator are shown in Figure 7.3.

The results for the ratios of theoretical heat transfer area compared to the net electric power output are shown in Figure 7.4a, Figure 7.4b and Figure 7.4c. The higher the exhaust gas inlet temperature or the exhaust gas outlet temperature, the more economically feasible processes are obtained based on this ratio, due to larger temperature differences between the working fluid and exhaust gas. The lowest exhaust gas outlet temperatures lead to the highest power output of the cycle, but rather large heat transfer areas are needed, especially with fluids cyclohexane and toluene. This can be explained by smaller temperature differences in the evaporator and larger heat rate in the evaporator, if the

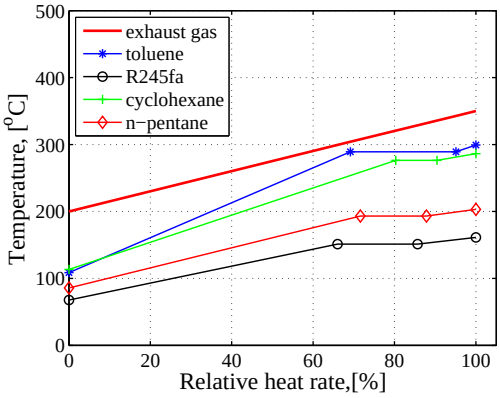

Figure 7.3: An example of temperature profiles in the evaporator in 350 °C exhaust gas utilization.

maximum power output is desired. The working fluids with lower critical point, namely R245fa and n-pentane, introduce smaller ratios with low EG inlet temperatures and low EG outlet temperatures when compared to toluene and cyclohexane.

It should be noted that if a fuel with relatively high sulfur content is used in the reciprocating engine, the exhaust outlet temperature should be limited above the acid dew point of the exhaust gases, to prevent the corrosive effects from occurring in the ORC evaporator and in the exhaust smoke stack.

7.1.2 Charge air heat utilization

In modern industrial diesel and gas engines, high pressure ratios are typically adopted for the turbocharger to improve the engine efficiency and increase the power output. The turbocharger pressure ratio highly affects the charge air outlet temperature after the turbocharger compressor, and thus, the turbocharger pressure ratio has a major impact on waste heat recovery potential from the charge air. The charge air temperature range used in this study is 180 °C-220 °C, which corresponds to the engine turbocharger pressure ratios in the range from 3.5 to 4.5. The results for ORC net power outputs are presented in Figure 7.5a, Figure 7.5b, and Figure 7.5c. The highest power outputs of $P_{\mathrm{e,net}}/q_{\mathrm{m,CA}}$ = 16.2 $kW/kg/s$, 11.6 $kW/kg/s$, and 7.7 $kW/kg/s$ with CA inlet temperatures of 220 °C, 200 °C, and 180 °C were obtained with working fluid R245fa. Based on the results, R245fa and n-pentane introduce the highest performance with low CA outlet temperatures and toluene and cyclohexane with high CA outlet temperatures. The peak value for the power output can be found for different working fluids with different charge air outlet temperatures. The working fluid R245fa reaches the pressure limit of $p_{\mathrm{ev}}/p_{\mathrm{cr}}$=0.95 with high charge air outlet temperatures. With low charge air outlet temperatures the evaporator pressure level is lower to maintain a sufficient pinch-point temperature difference in the evaporator. This can be observed as a change in the slope of the curve with R245fa in Figure 7.5a, Figure 7.5b, and Figure 7.5c.

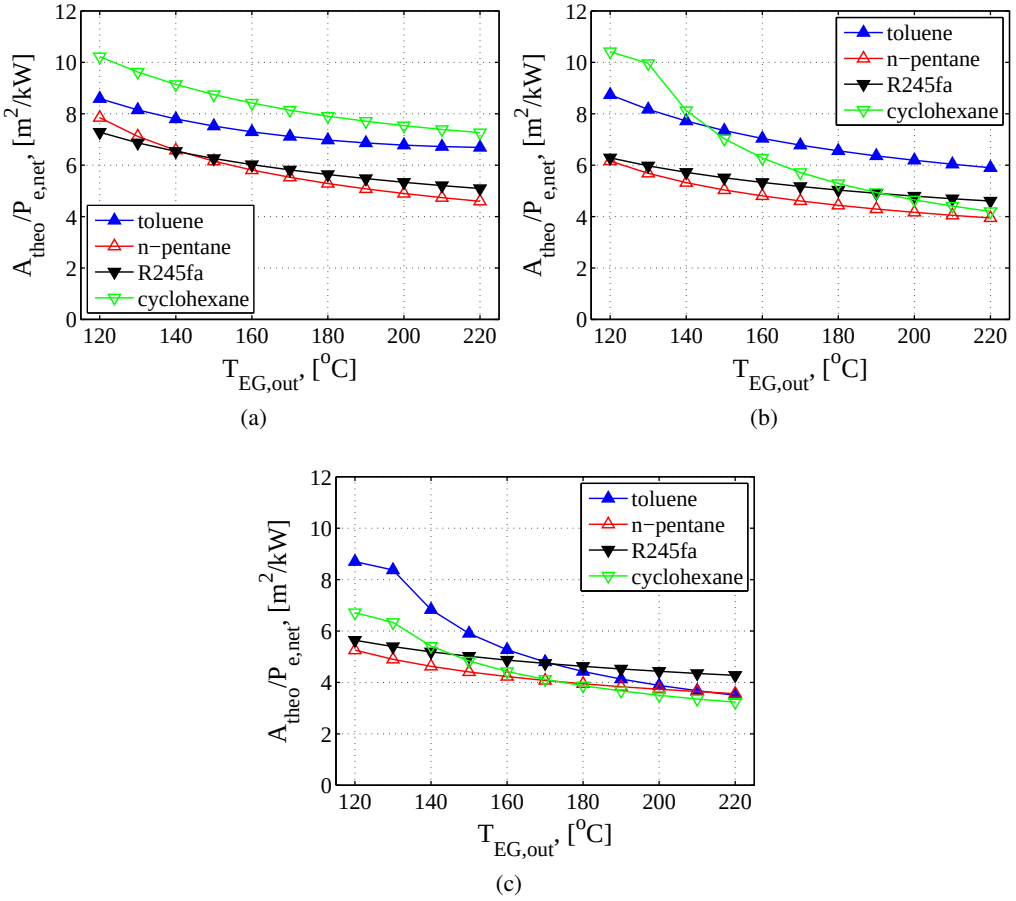

Figure 7.4: The effect of exhaust gas temperature at the outlet of the evaporator on the ratio of theoretical heat transfer area to net power output for different organic working fluids with exhaust gas inlet temperatures of (a) 300 °C, (b) 350 °C, and (c) 400 °C.

An example of the evaporator temperature profiles in 200 °C charge air utilization is shown in Figure 7.6. With working fluids toluene and cyclohexane a larger portion of the heat is needed for the fluid evaporation than with fluids R245fa and n-pentane. This can be explained by the lower evaporation temperature and pressure levels compared to the critical temperature and pressure of the fluid. Figure 7.6 also indicates that the pinch-point temperature difference occurs closer to the cold end of the evaporator with fluids toluene and cyclohexane, and only small portion of the heat is used for preheating the fluid, when compared to n-pentane and especially R245fa.

The results for the ratios of theoretical heat transfer areas compared to net electric power output are shown in Figure 7.7a, Figure 7.7b and Figure 7.7c. Based on the results, approximately 2-4 times larger ratios of heat transfer area to the process power output are

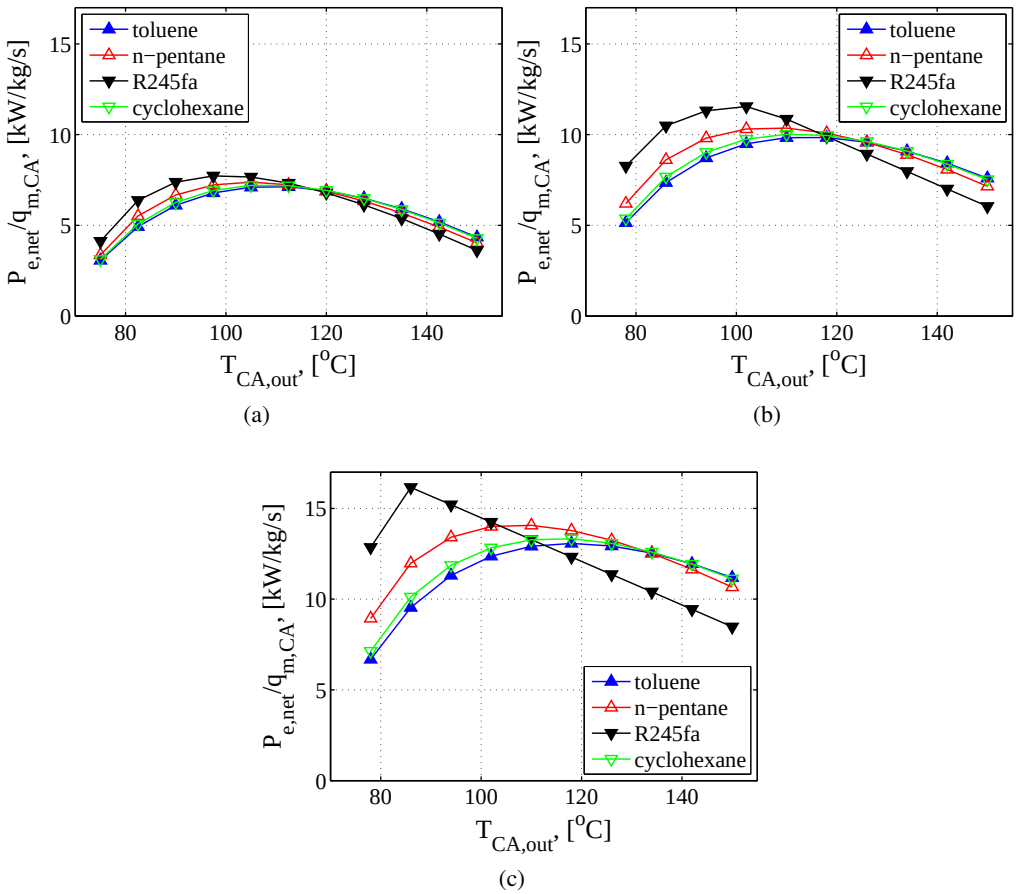

Figure 7.5: The effect of charge air temperature at the outlet of the evaporator on the ratio of net power output to charge air mass flow rate for different organic working fluids with charge air inlet temperatures of (a) 180 °C, (b) 200 °C, and (c) 220 °C.

needed in the charge air heat utilization compared to the exhaust gas heat utilization, leading to economically more unfeasible processes. The large heat transfer areas in CA utilization can be mainly explained by the smaller temperature differences between the heat source and the working fluid in the evaporator, as well as by the lower cycle efficiency when compared to the EG utilization, due to the lower evaporation temperatures.

It should be noted that the charge air outlet temperatures corresponding to the highest power outputs of ORC are relatively high compared to typical charge air temperatures after the engine CAC. Thus, an additional cooling for charge air would be required after the ORC evaporator. This heat could be used for preheating the ORC working fluid thus replacing the recuperator or cooled down with the engine cooling loop. Also the pressure losses in charge air should be minimized because the pressure loss has a negative effect on

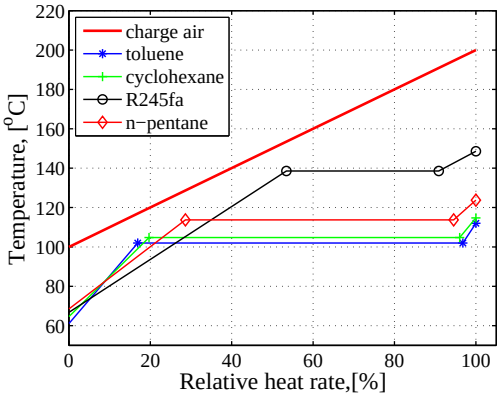

Figure 7.6: An example of temperature profiles in the evaporator in 200 °C charge air utilization.

reciprocating engine performance, and this should be taken into account when designing the ORC evaporator for charge air utilization.

7.1.3 The effect of the condensing temperature and the minimum pinch-point temperature difference on the ORC performance

The previously presented results were obtained by using the condensing temperature of 50 °C, and the minimum pinch-point temperature difference was set to 15 °C. The effect of minimum pinch-point temperature difference and condensing temperature on process performance in exhaust gas utilization and charge air utilization is presented in Figure 7.8a, Figure 7.8b, Figure 7.9a, and Figure 7.9b. The selected working fluids are toluene for EG heat recovery and n-pentane for CA heat recovery.

The results show that the minimum pinch-point temperature difference and condensing temperature have a significant effect on the process performance. If a low condensing temperature and small temperature differences are used, a greater electric power output is achieved, compared to the higher condensing temperatures and larger temperature differences in the ORC evaporator. Based on the results, the relative effect of condensing temperature and minimum pinch-point temperature difference on system power output is more significant in the CA heat utilization than in the EG heat utilization, due to the smaller temperature difference between the condenser and the evaporator. Thus, especially the potential to produce electric power from charge air heat is highly related to these above mentioned cycle operating parameters.

7.1.4 Case study

A case study of available additional electric power output was performed for engine combined cycles utilizing EG and CA heat. The used computational method is as presented in the previous sections. The minimum pinch-point temperature difference in the ORC evaporator was limited to 15 °C and the condensing temperature of 50 °C was used. The

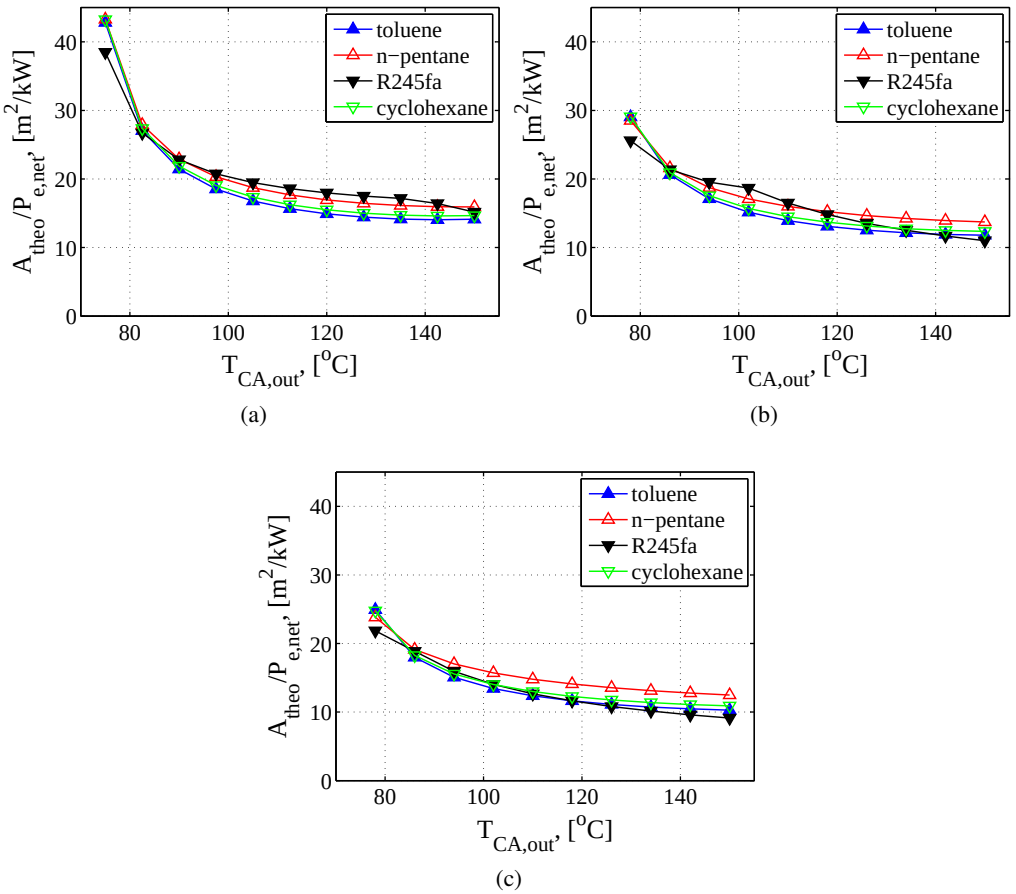

Figure 7.7: The effect of charge air temperature at the outlet of the evaporator on the ratio of theoretical heat transfer area to net power output for different organic working fluids with charge air inlet temperatures of (a) 180 °C, (b) 200 °C, and (c) 220 °C.

case study was performed for a large industrial gas-fired diesel engine having an electric power output of 16.6 MW. The EG temperature after the turbocharger of the engine is 395 °C and the EG mass flow rate is 27.0 kg/s. The CA temperature after the turbocharger is 210 °C and the CA mass flow rate is 26.2 kg/s. The selected working fluids for the analysis were toluene in EG heat recovery and R245fa in CA heat recovery. The main results are presented in Table 7.2. The results show that by utilizing the EG heat, a maximum increase of 11.4 % in the electric power output was obtained for the selected engine. The CA heat utilization increases the power output of the engine system by 2.4 %.

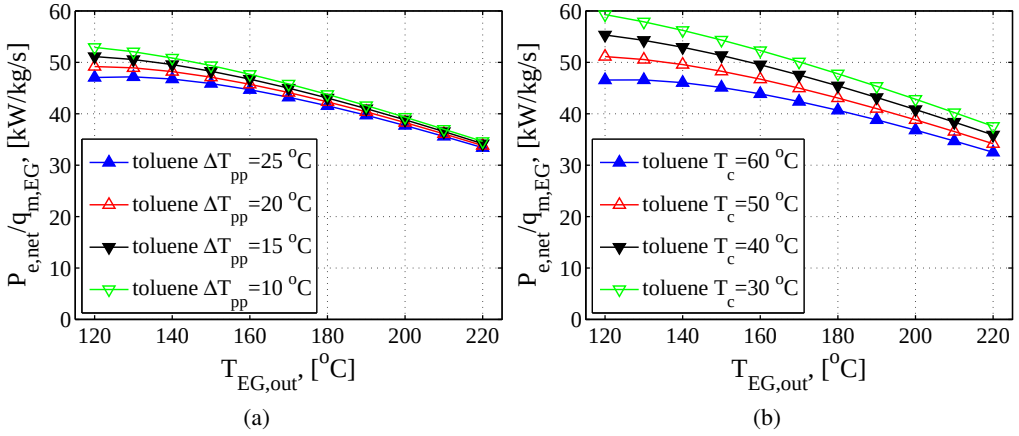

Figure 7.8: The effect of pinch-point temperature difference (a), and condensing temperature (b) on ORC power output. The working fluid is toluene and the exhaust gas inlet temperature is 350 °C

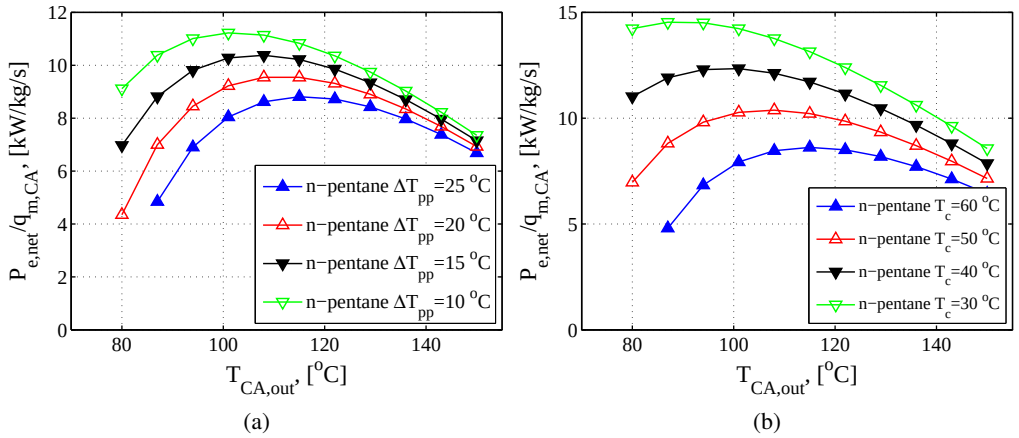

Figure 7.9: The effect of pinch-point temperature difference (a), and condensing temperature (b) on ORC power output in charge air heat utilization. The working fluid is n-pentane and charge air inlet temperature is 200 °C

7.2 Experimental results for charge air utilization

7.2.1 Description of the experimental setup

The utilization of the charge air heat by means of ORC was tested with an experimental setup. The experimental setup is located at VTT Technical Research Centre of Finland in Espoo, and the test runs were carried out in the VTT engine laboratory. The selection of the main ORC process spefications and the design of the heat exchangers was carried out at LUT. The experimental setup consists of a 1.6 MW_e diesel engine and an ORC having

Table 7.2: Case study results.

EG heat recovery 395 °C-130 °C	
heat rate to evaporator	7921 kW
ORC power output	1895 kW
ORC electric efficiency	23.9 %
increase in power plant electric power output	11.4 %
CA heat recovery 210 °C-85 °C	
heat rate to evaporator	3333 kW
ORC power output	394 kW
ORC electric efficiency	11.8 %
increase in power plant electric power output	2.4 %

the turbine replaced with a pressure reduction system, and thus, no power was extracted from the system. The main technical data of the test engine is presented in Table 7.3.

Table 7.3: Technical data of the test engine.

Electric power output	1640 kW
Rotational speed	750 rpm
Number of cylinders	4
Cylinder inner diameter	320 mm
Power/cylinder	410 kW
Mean effective pressure	22.97 bar
Charge air mass flow rate	3.14 kg/s
Compressor pressure ratio	3.43
Compressor efficiency	c. 80 %
Charge air temperature at compressor outlet	185 °C

The aim of the tests was to study especially the performance of the evaporator acting as a charge air cooler, and thus, to validate the simulated potential on producing additional power from the charge air heat.

A layout of the experimental setup is presented in Figure 7.10 and a schematic process diagram in Figure 7.11, presenting the main components of the system as well as the locations of pressure, temperature, and mass flow measurements. The evaporator was located inside the engine hall near the engine turbocharger, and the intercooler of the engine was installed after the evaporator to further cool down the charge air before it enters the engine. The rest of the experimental setup; namely the expansion valve, recuperator, condenser, condensate tank, and the feed pumps; were located outside the engine hall. Commercial heat exchangers of plate and shell type were used in the experimental setup.

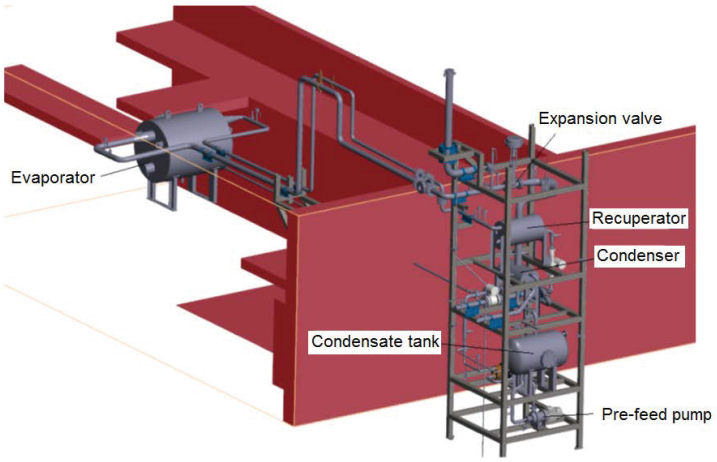

Figure 7.10: Layout of the experimental setup.

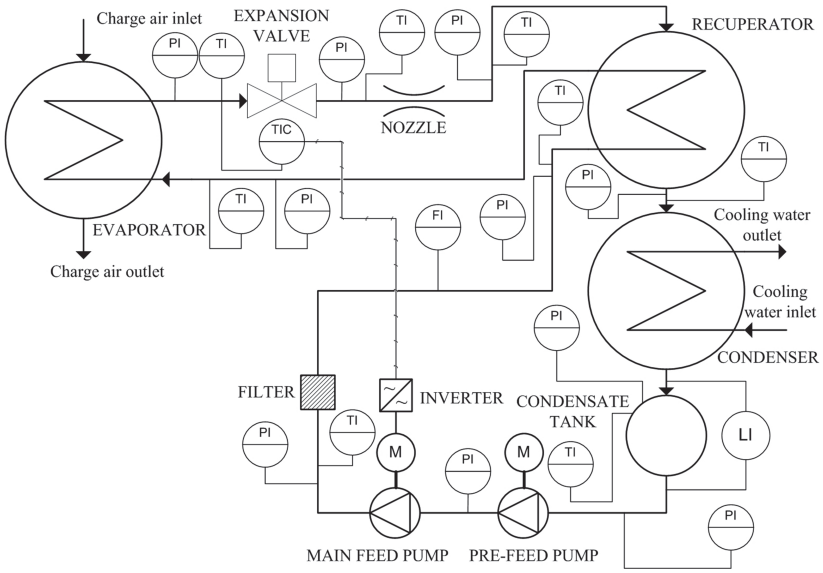

Figure 7.11: Schematic process diagram and main components of the experimental setup including the working fluid side measurements.

The thermodynamic design of the ORC experimental setup was based on the use of R245fa as a primary working fluid. In addition, the requirements of using other working fluids; namely R245ca, isopentane, and pentane; was considered in the design. The test runs were carried out by using R245fa and isopentane as working fluids. The experiments were carried out at engine full load with R245fa and isopentane and at 50 %, 75 %,and 90 % engine load with R245fa. R245ca was omitted from the test runs due to the

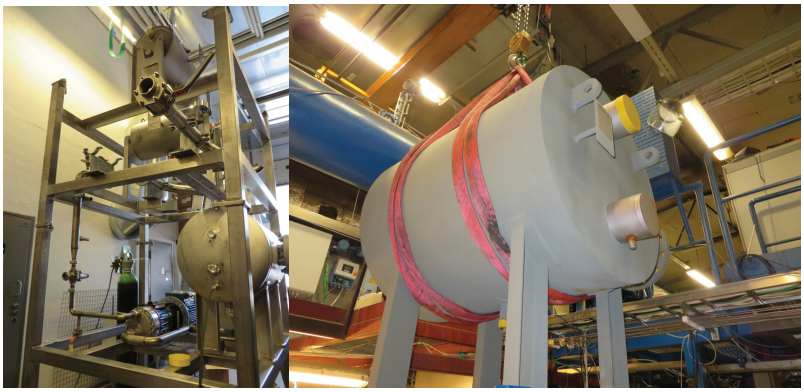

(a) (b)

Figure 7.12: Experimental setup under construction, a) recuperator, condenser, condensate tank and pre feed-pump and b) evaporator (Pictures by Jaakko Larjola).

problems related to the availability of the fluid and high price, which appeared when the amounts of the working fluids were purchased. Later, n-pentane was also omitted from the test runs due to lack of time and resources to perform the test runs with the third fluid. However, the results obtained with isopentane are well comparable with the results obtained with n-pentane, since these two fluids posses comparably similar properties from the thermodynamic point of view.

The main test results for full engine load with working fluids R245fa and isopentane are presented first, and they are followed by the presentation of the results with engine part load with working fluid R245fa.

7.2.2 Condensing conditions

From the test results, it was observed that the condensing temperature in the condenser with R245fa is 10.5 °C-12.5 °C and with isopentane 10.2 °C-10.9 °C lower than the saturated temperature corresponding to the condenser pressure. On the other hand, with R245fa the condensing pressure is 0.76 bar-0.88 bar and with isopentane 0.40 bar-0.45 bar higher than the saturated pressure corresponding to the measured condenser temperature. This can be caused by the presence of non-condensable gases in the system, such as air or small amounts of water. These condensing pressure deviations when compared to the saturated conditions in the condenser were taken into account in the analysis of the test run results.

7.2.3 Experimental results at 100 % engine load

The test runs at 100 % engine load were carried by using R245fa and isopentane as working fluids. Four different evaporation pressures were used for both fluids in order to study the performance of the evaporator with different working fluid conditions. The results for

charge air and working fluid temperature profiles at the evaporator are presented in Figure 7.13a and Figure 7.13b. The results of the heat rate introduced in the evaporator with

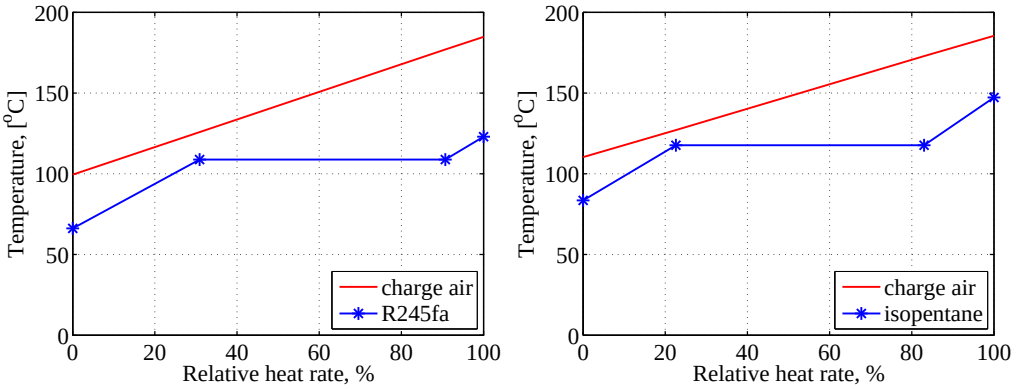

Figure 7.13: Measured working fluid and charge air temperature profiles in the evaporator. a) presents the measured temperature profile with R245fa with the evaporator outlet pressure of 15.3 bar and b) presents the measured temperature profile with isopentane with the evaporator outlet pressure of 10.39 bar

different evaporation pressures are presented in Figure 7.14a, the measured charge air temperatures at the evaporator outlet in Figure 7.14b, and measured working fluid mass flow rates in Figure 7.14c.

The results indicate that a larger heat rate was introduced to the working fluid when low evaporation pressures were used. This can be mainly explained by the fact that with higher evaporation pressures, the charge air exits the evaporator at higher temperature to maintain a sufficient temperature difference between the working fluid and the charge air, when compared to the charge air temperatures at the evaporator outlet when lower evaporation pressures are adopted. In additon, the working fluid mass flow rates are lower when high evaporation pressures are adopted.

7.2.4 Experimental results at engine part load

The test runs for engine part load operation were carried out by using R245fa as working fluid. The engine part load measurements were carried out at 50 %, 75 %, and 90 % engine loads. The measured charge air inlet and outlet temperature at engine part load are presented in Figure 7.15a, the results for measured heat rate into the evaporator at engine part load operation are presented in Figure 7.15b, and the pinch-point temperature difference in the evaporator is presented in Figure 7.15c.

Based on the results presented in Figure 7.15a, Figure 7.15b, and Figure 7.15c the charge air temperatures and the heat rate into the evaporator are significantly lower at engine part

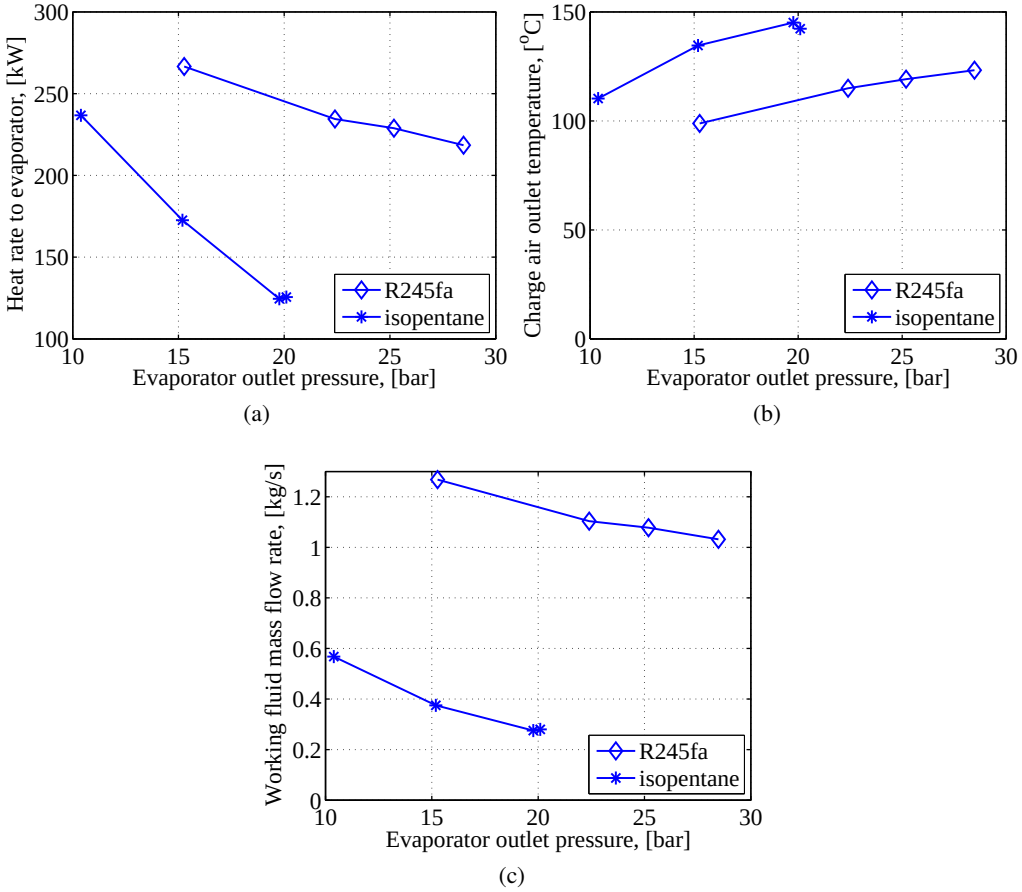

Figure 7.14: Measured heat rate to the evaporator (a), charge air temperature at the evaporator outlet (b), and working fluid mass flow rate (c) with different evaporator outlet pressures at full engine load.

loads, when compared to engine full load conditions. The pinch point temperature difference in the evaporator increases as the evaporation pressure and the engine load increases, mainly due to the higher flow rates at the charge air and working fluid side at higher engine loads. The measured working fluid mass flow rate and the evaporator outlet pressure are presented in Figure 7.16a and Figure 7.16b.

The results indicate that significantly lower working fluid mass flow rate and low evaporator outlet pressure are obtained at engine part loads, showing almost linear behaviour as a function of engine power. As a conclusion the results indicate that the availability to produce additional power from charge air at engine part loads is significantly lower when compared to full engine loads caused by the lower amount of heat introduced to the evaporator resulting to low working fluid mass flow rate and lower temperature level

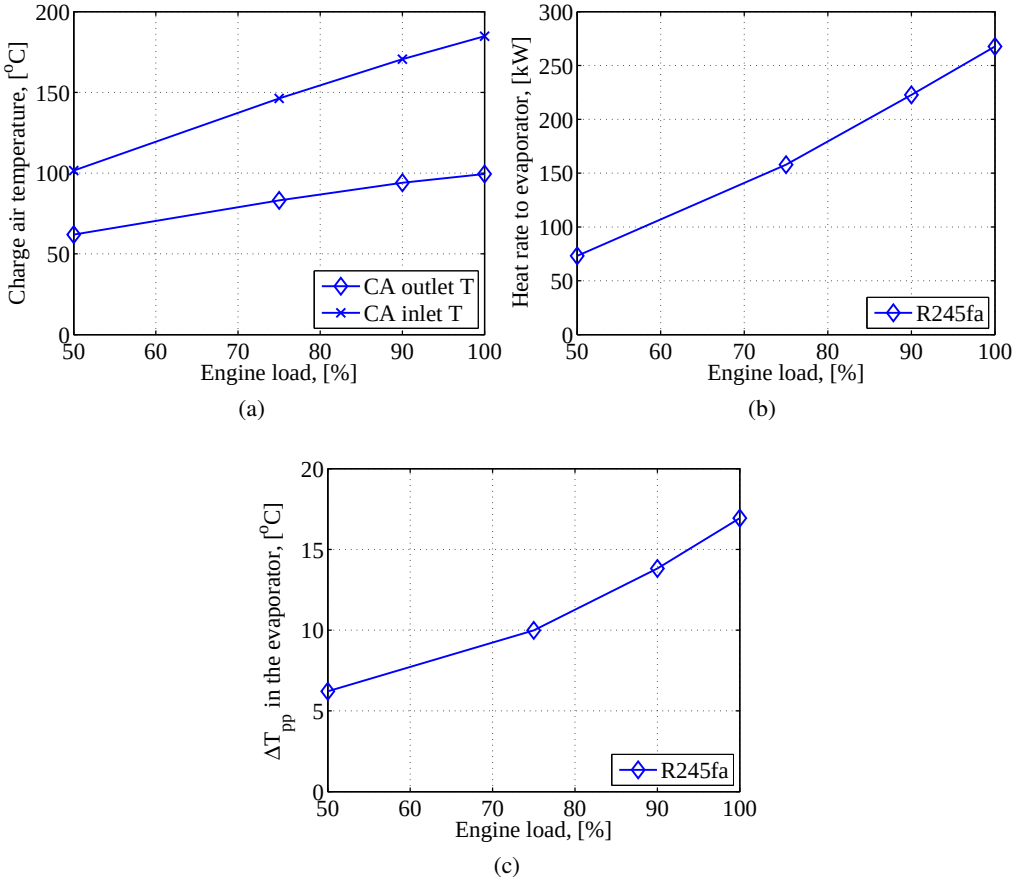

Figure 7.15: Measured charge air temperature at the evaporator inlet and outlet (a), heat rate to the evaporator (b), and pinch-point temperature difference in the evaporator (c) at engine part loads and at full engine load.

of the charge air leading to lower cycle efficiency. This is important to take into account especially when considering the use of charge air heat utilization in engines operating frequently at part load conditions.

7.2.5 Process with pressure reduction system replaced with a turbine

Based on the measured results, the power output of the system was estimated in a case when the pressure reduction system is replaced with a turbine-generator having the turbine with an isentropic efficiency of 80 % and other process values were evaluated based on the measurement results. If the process would be equipped with a turbine-generator, power would be extracted from the expansion leading to lower vapour temperature at the recuperator inlet as well as to lower liquid temperature at the evaporator inlet, when compared to the measured values with process with the pressure reduction system. If a

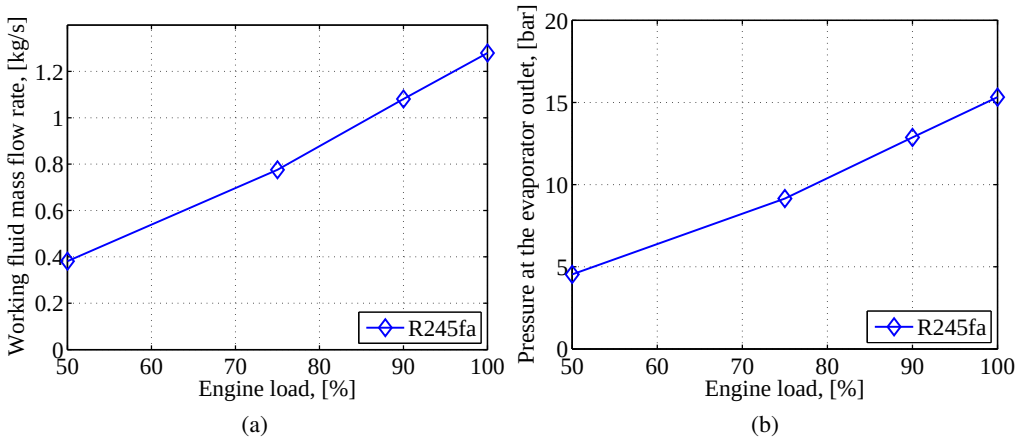

Figure 7.16: Measured working fluid mass flow rate (a), and evaporator outlet pressure (b), at engine part loads and at full engine load.

process equipped with a turbine would be used, the charge air temperature at the evaporator outlet would be slightly lower than the measured charge air outlet temperature, since the temperature difference between the charge air and working fluid at the evaporator cold end would be higher. The measured charge air temperature at the evaporator outlet and estimated charge air temperatures at the evaporator outlet, if a turbine were adopted to the system instead of the pressure reduction system, are presented in Figure 7.17. The performance of the process heat exchangers in a case if the turbine were adopted to the system were evaluated based on the measured values and by using conductances evaluated from the measurement results. The influence of mass flow rates affecting the heat transfer coefficients was taken into account in the evaluation of conductances.

The power output of the system was calculated by using the condensing temperature of about 30 °C, which was measured in test runs, and by using higher condensing temperature of 40 °C which was used in the design of the experimental setup components. The calculated results for electric power output from the ORC are presented in Figure 7.18a and the electric power output divided by the charge air mass flow rate in Figure 7.18b. The increase of the engine power is presented in Figure 7.18c and the results of the estimated ORC net electric effciency are presented in Figure 7.18d.

Based on the results presented in Figure 7.18a with isopentane, the maximum electric power output of 31.5 kW would be achieved if the measured condensing temperature of about 30 °C is used, as in the test runs, and the electric power output of 27.0 kW would be achieved with a condensing temperature of 40 °C, which was used as a condensing temperature in the experimental setup design. With R245fa, the maximum electric power output of 30.4 kW would be achieved if a condensing temperature of about 30 °C is used, and the electric power output of 26.7 kW would be achieved with a condensing temper-

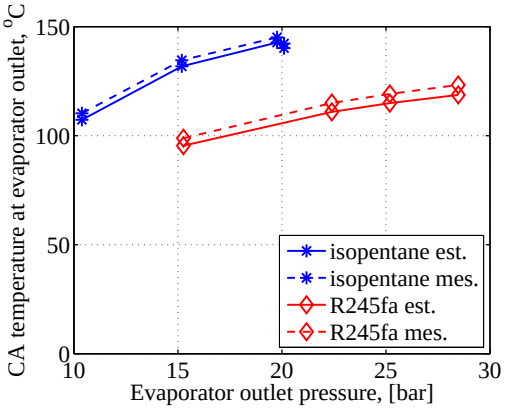

Figure 7.17: Measured charge air temperature at the evaporator outlet and estimated charge air temperature at the evaporator outlet if a turbine were adopted in the cycle instead of the pressure reduction system.

ature of 40 °C. The results of the power output divided by the charge air mass flow rate presented in Figure 7.18b are well comparable to the results obtained in the thermodynamic analysis presented in Figure 7.5a and Figure 7.5b representing comparably similar charge air temperatures but slightly higher condensing temperature and neglecting pressure losses. The highest power output of $P_{\mathrm{e,net}}/q_{\mathrm{m,CA}}$ = 10.1 $kW/kg/s$ and $P_{\mathrm{e,net}}/q_{\mathrm{m,CA}}$ = 8.7 $kW/kg/s$ were achieved with both fluids with the condensing temperatures of 30 °C and 40 °C, respectively.

The maximum power outputs from the ORC correspond to 2 % and 1.7 % power increase in the whole engine system, and in general, only small differences in the power output can be observed when comparing results obtained with both fluids. The power increase is slightly lower when compared to the simulated result presented in the case study for 16.6 MW gas-fired engine in Section 7.1.4, since the charge air temperature of the test engine was approximately 25 °C lower than the one used in the case study due to the lower turbocharger pressure ratio of 3.43 when compared to modern engines. In addition, the pressure losses were excluded from the case study, and lower charge air temperatures at the evaporator outlet were used in the case study when compared to the measured charge air temperatures at the evaporator outlet. As can be observed from Figures 7.18a - 7.18d, the points having the lowest evaporator outlet pressures represents the highest turbine power and the obtained power decreases if the highest evaporation pressures are adopted in the system. On the contrary, the highest cycle net electric efficiencies are obtained with the highest evaporation pressures. The estimated ORC net electric efficiencies vary between 9.6 %-12.8 % with R245fa, depending on the condensing temperature as well as on the evaporator outlet pressure. Slightly higher efficiencies in the range of 11.1 %-15.2 % are obtained with isopentane. The decrease on the obtainable power output as well as the increase in the net electric efficiency as the evaporator outlet pressure increses, is more significant with isopentane, when compared to the results obtained with R245fa.

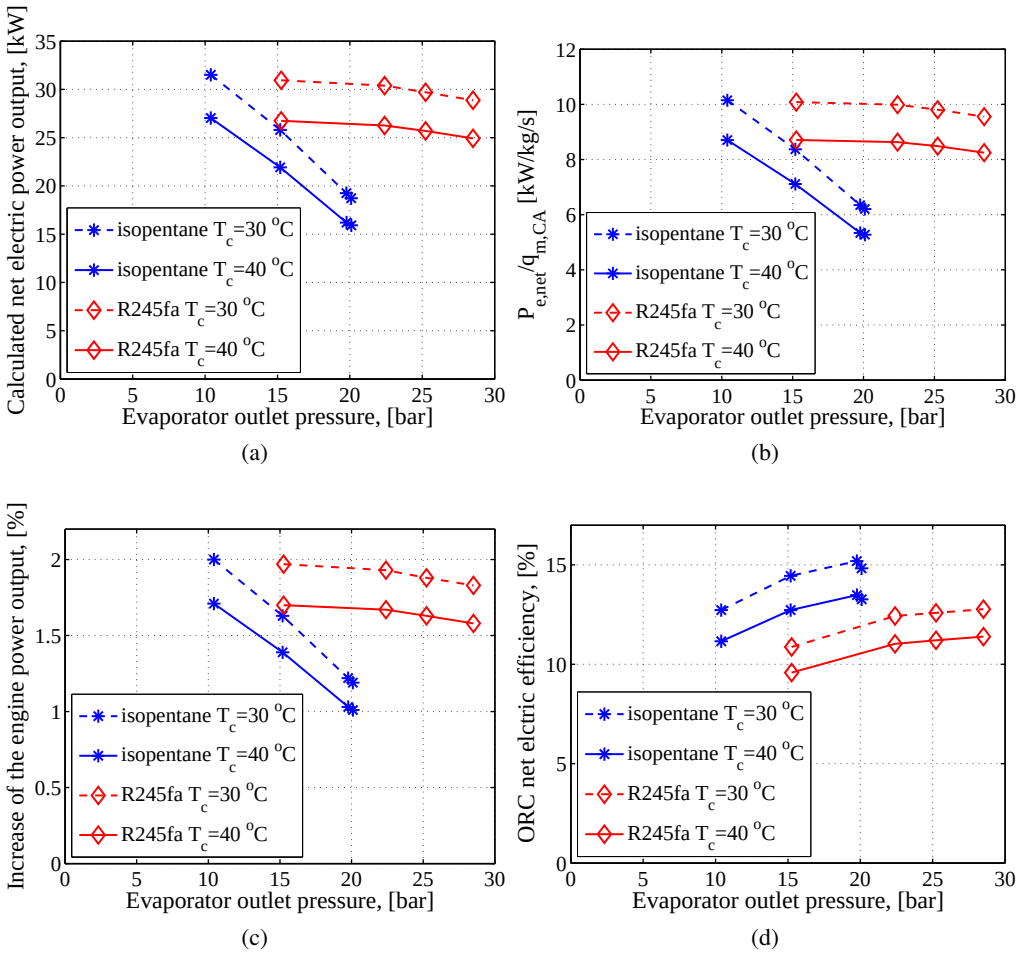

Figure 7.18: Estimated power (a), power output divided by the charge air mass flow rate (b), estimated increase of the engine power output (c), and estimated net electric efficiency (d) if the expansion valve would be replaced with a turbine. The results are presented for different evaporation pressures at full engine load.

7.3 Conclusions and discussion

The aim was to study the potential for electricity production from the waste heat of large reciprocating engines with the ORC process technology, and hence, to increase the efficiency of the engine power plant. A thermodynamic analysis was carried out for working fluids toluene, n-pentane, R245fa, and cyclohexane, and the effect of different process parameters on the cycle performance was studied. The highest potential is related to exhaust gas heat recovery, but also charge air heat can be identified as a potential for additional power production. A case study was performed for a 16.6 MW gas-fired diesel engine and the results show that the power output of the selected engine can be increased by 11.4 % by utilizing exhaust gas heat and by 2.4 % by utilizing the charge air heat.

Fluids with higher critical temperature, toluene, and cyclohexane, introduced the highest power outputs in exhaust gas heat recovery. Fluids with lower critical temperature, R245fa and n-pentane, introduced the highest performances in charge air heat utilization, especially with low charge air outlet temperatures. The ORC process performance is also highly dependent on the heat source temperature, pinch-point temperature difference in the evaporator, and the condensing temperature used in the process. The power output increases if a smaller temperature differences are allowed in the heat exchangers, but on the other hand, larger heat transfer areas are needed in the processes. The results show that the selection of the working fluid and the process parameters should not be based only on maximizing the power output of the ORC system, but also considering the economic feasibility of the process, by evaluating the ratio of heat transfer area needed and the power output of the process. The results for the ratio between theoretical heat transfer areas and power output show that the exhaust gas utilization would give approximately 2-4 times smaller heat transfer area per produced kW when compared to charge air heat utilization. In charge air heat utilization, relatively large heat transfer areas are needed compared to the electric power output achieved, leading to economically more unfeasible processes. A more detailed analysis should be carried out by taking into account more accurate heat transfer coefficients for each fluid and adopting the effects of using different heat exchanger types. In addition, a cost function based on the estimated heat exchange area could be used in the future studies to evaluate the economic feasibility of the processes in more detail.

The utilization of charge air heat was studied with an experimental setup. R245fa and isopentane were adopted as working fluids in the test runs. The test runs indicated that the measured performance of the evaporator and other process components had a good agreement in respect to the thermodynamic cycle design. Based on the measurements and calculations for the ORC power output with a system having the pressure reduction system replaced with a turbine-generator, achievable power increase in the engine system of 2.0 % was evaluated when a condensing temperature of 30 °C was used and 1.7 % was evaluated when a condensing temperature of 40 °C was used. The results for power output are comparably similar with both R245fa and isopentane.

8 Summary and recommendations

Demand for the use of energy systems, entailing high efficiency as well as availability to harness renewable energy sources, is a key issue in tackling the threat of global warming and saving natural resources. ORC technology has been identified as one of the most promising technologies in recovering low-grade heat sources that cannot be efficiently utilized by means of more conventional power systems. The ORC is based on the working principle of Rankine process, but an organic working fluid is adopted in the cycle instead of steam.

In this thesis, the design and working fluid selection in small and micro-scale ORCs based on turbine technology were studied. The effect of adopting different working fluids on the process design and performance was studied first by means of thermodynamic analysis, and the effect of the critical temperature and the group of the working fluid on the fluid selection was highlighted. In addition to the working fluid selection and cycle design by thermodynamic analysis, this thesis investigated the design of high-speed turbines for small-scale ORCs. Two main applications were selected for the study. First, the exhaust gas heat recovery from small-scale diesel engines, which can be found in numerous applications, such as in remote stationary power systems and in mobile vehicles, concentrating mainly on the working fluid selection and turbine design, and second, the heat recovery from industrial-scale power plant engines, concentrating mainly on the utilization of charge air and exhaust gas heat as well as on the optimization of the waste heat recovery processes.

The results obtained from the preliminary thermodynamic analysis with various working fluids for processes having the evaporation pressure close to the critical pressure of the fluid indicated that the critical temperature, molecular weight and the group of the working fluid highly influences the obtainable cycle efficiency, process operational parameters, and turbine design. The studied fluids can be divided into three categories; hydrocarbons, siloxanes, and fluorocarbons. The studied parameters were the cycle efficiency, condensing pressure, process expansion ratio, enthalpy change over the turbine, and speed of sound. In general, when comparing different fluids of the same working fluid group, the higher the critical temperature and molecular weight of the fluid, the higher the obtainable process efficiency. On the contrary, the high critical temperature leads to a high expansion ratio over the turbine and to low condensing pressures well below atmospheric pressure, especially with siloxanes and heavy hydrocarbons. Low critical temperature hydrocarbons and fluorocarbons represented higher condensing pressures and lower expansion ratios over the turbine. The highest cycle efficiencies were simulated when using high critical temperature hydrocarbons and siloxanes and the lowest efficiencies when using low critical temperature hydrocarbons and fluorocarbons.

The preliminary designs of radial turbines in the power range from 10 kW to 200 kW were studied with several working fluids and different working parameters. The results indicated that the turbine geometry and rotational speed are closely connected to the selection

of the working fluid. In general, the results indicate that the design of ORC turbines with a very low power output is difficult, because the turbine wheels tend to be small and fast rotating and especially due to the small blade height at the turbine rotor inlet. The results indicated that by selecting a fluid with a high molecular weight and high critical temperature leads to larger turbine wheels and lower rotational speeds when compared to the fluids having a low molecular weight and low critical temperature. On the other hand, the use of fluids having a high critical temperature results in a large increase in the rotor blade height between the rotor inlet and outlet and is estimated to have a negative impact on the turbine efficiency, if single stage turbines are considered. The studied siloxanes represented larger turbine wheels and lower rotational speeds than the fluids from the other fluid groups. The largest blade heights at the rotor inlet were simulated with the studied fluorocarbons and siloxanes. The results indicated that the flow in the turbine stator is highly supersonic in this kind of ORC turbines, representing additional losses caused by the occurrence of oblique shock waves in the turbine. Based on the results, by selecting a low turbine inlet pressure or a low degree of reaction, the blade height at the rotor inlet can be increased, rotor blade height ratio can be decreased, and larger turbine wheels and lower rotational speeds can be obtained. The results indicated that the fluids representing the highest thermodynamic performances are not necessarily the optimal fluids when taking into account the turbine design. Thus, when selecting the working fluid it is recommended to take into account both the thermodynamic performance of the cycle and availability to design a turbine with a relatively high efficiency.

The exhaust gas heat recovery of small-scale diesel engine was studied and the considered ORC application had the power output of about 10 kW. Siloxanes were considered as suitable working fluids based on the results from the preliminary thermodynamic analysis and turbine design study. Toluene was included in the analysis to compare the results obtained with siloxanes and a suitable hydrocarbon. The cycle design and a preliminary turbine designs were carried out. The results from the radial turbine design calculations show that the largest wheel diameters, largest blade heights at the rotor outlet, and lowest rotational speeds were achieved with fluids MDM and D_4, having relatively high molecular complexity. The use of toluene and MM as working fluids, would require smaller turbines with high rotation speeds (80 000 rpm-180 000 rpm). The blade heights at the rotor inlet in the preliminary turbine design were found out to be significantly small, 0.7 mm-1.4 mm, with all the studied fluids, which was estimated to have a negative impact on the turbine efficiency, manufacturing, and operation. The results showed that the net electric power output of the analyzed small-capacity ORC systems is rather insensitive to small changes of the turbine isentropic efficiency. Thus, it is recommended that the selection of the working fluid and process operational parameters should be based on the overall performance of the cycle, rather than only on the optimal design of the turbine.

A more detailed turbine design and flow analysis were presented for the turbine designed for an experimental setup using MDM as the working fluid. The selection of the working fluid was a compromise taking into account the cycle efficiency, process design, and turbine design. An accurate thermodynamic real-gas model was implemented into the CFD

solver to have a prediction on the flow field in the stator and rotor. The results obtained with different supersonic stators indicated that convergent-divergent nozzles introduce uniform flow at the straight part of the nozzle in a region before the stator trailing edge. However, the stator blade trailing edge has a significant effect on the flow after the occurrence of two oblique shock waves, their reflections, and the viscous wake. The shock waves and viscous wake causes a non-uniform flow field and fluctuations on the flow angle at the stator exit. The results showed that the flow is more tangential in off-design conditions, and the fluctuation in the flow angle increases due to non-uniform flow field. This might cause flow separation and low loading at the turbine rotor blades in off-design conditions. Different stator design methods could be studied and further developed in the future in order to reach more uniform flow angle and velocity distribution at the stator outlet in design and off-design conditions.

The CFD simulations for different turbine rotors predicted slightly higher pressure ratio over the turbine when compared to the pressure ratio in the rotor 1D design. In addition to higher pressure ratios, the temperature drop in the turbine rotor is predicted to be higher by the CFD simulations when compared to the estimation of 1D turbine design. A flow separation region at the rotor blade suction side was predicted with all the studied geometries. In addition, the angle of relative velocity at the rotor inlet and the flow velocity at the rotor inlet were slightly different when compared to the 1D design and the results obtained in stator simulations, causing a flow separation at the blade pressure side at the rotor blade leading edge. It is recommended based on the results obtained in this study to perform additional simulations in the future in which the stator and rotor are coupled together in order to study the effect of rotor inlet conditions on the flow field and performance in more details. The effect of the number of rotor blades on the flow separation in the rotor could be studied in the future. In addition, the flow field in the turbine rotor should be studied in off-design conditions as well. Unsteady simulations for similar turbine should be carried out in the future in order to study the loss mechanisms related to the interaction between the turbine stator and rotor blades. The performance of the designed radial turbine will be measured with experiments that will take place in 2014-2015 to provide more information on the design and performance of small-scale and high expansion ratio ORC turbines.

The potential for electricity production from the waste heat of large-scale reciprocating engines was studied in this thesis as well. The results showed that the highest potential is related to the exhaust gas heat recovery, but also the charge air heat was identified as a potential for additional power production. The fluids with a high critical temperature represented the highest performances in the exhaust gas heat recovery and the fluids with a lower critical temperature represented the highest performances in the charge air heat recovery. A case study was performed for a 16.6 MW gas-fired diesel engine, and the results showed that the power output of the selected engine can be increased by 11.4 % by utilizing exhaust gas heat and 2.4 % by utilizing the charge air heat. The results also indicated that the charge air heat utilization would give approximately 2-4 times larger heat transfer area per produced kW when compared to the exhaust gas heat utilization leading to economically more unfeasible processes. A more detailed analysis should be carried

out in the future by taking into account more accurate heat transfer coefficients for each fluid and adopting the effects of using different heat exchanger types. In addition, a cost function based on the estimated heat exchange area could be used in the future studies to evaluate the economic feasibility of the processes in more detail. The utilization of charge air heat was studied with an experimental setup, and R245fa and isopentane were adopted as working fluids in the test runs. The test runs indicated that the measured performance of the evaporator and other process components had a good agreement in respect to the thermodynamic cycle design. Based on the measurements and calculations for the ORC performance, a power increase in the test engine system of 2.0 % was achievable when a condensing temperature of 30 °C was used, and a power increase in the engine system of 1.7 % was estimated when a condensing temperature of 40 °C was used.

As a result of this study, suitable working fluid candidates for small-scale ORCs were identified and the availability to design ORC turbines for the selected applications was evaluated. In addition, important aspects of designing ORC systems were highlighted. Based on the current study the author would suggest that more experimental work on ORC turbines should be carried out to provide knowledge on the performance and design guidelines for small-scale ORC systems based on turbine technology. In addition, the different working fluids should be evaluated not only by taking into account the thermodynamic performance and turbine design but taking into account the thermal and chemical stability limits of the fluid, price, flammability, toxicity, as well as ozone depletion and global warming potential. ORC systems adopting working fluid mixtures, supercritical fluid conditions, or having multiple pressure levels could be investigated to better match the working fluid temperature with the heat source and further increase the power output obtainable from the ORC systems.

References

Anderson J.D. Jr. (1991). Fundamentals of Aerodynamics. McGraw-Hill, 2nd edition, ISBN 0-07-100767-9.

Angelino G. and Moroni V. (1973). Perspectives for waste heat recovery by means of organic fluid cycles. *Journal of Engineering for Power*, 95(2), pp. 75-83.

Angelino G., Gaia M., and Macchi E. (1984). A review of Italian activity in the field of organic Rankine cycles. VDI Berichte - Proceedings of the International VDI Seminar, VDI Verlag, 539, pp. 465-482.

Angelino G. and Invernizzi C. (1993). Cyclic methylsiloxanes as working fluids for space power cycles. *Journal of Solar Energy Engineering*, 115, pp. 130-137.

Angelino G. and Colonna, P. (1998). Multicomponent working fluids for Organic Rankine Cycles (ORCs). *Energy*, 23, pp. 449-463.

Angelino G. and Colonna P. (2000a). Organic Rankine Cycles (ORCs) for energy recovery of molten carbonate fuel cells. 35th Intersociety Energy Conversion Engineering Conference, Las Vegas, USA.

Angelino G. and Colonna P. (2000b). Air cooled siloxane bottoming cycle for molten carbonate fuel cells. Fuel Cell Seminar, Portland OR, October 2000, pp. 667-670.

Balje O.E. (1981). Turbomachines: A Guide to Design, Selection and Theory. John Wiley and Sons, New York.

Bini R., and Manciana E. (1996). Organic Rankine cycle turbogenerators for combined heat and power production from biomass. Energy conversion from biomass fuels; current trends and future systems. Munich, Germany, 22-23 October 1996.

Bini R., Di Prima M., and Guercio A. (2010). Organic Rankine cycle (ORC) in biomass plants: an overview on different applications. Turboden srl.

Bombarda P., Invernizzi C.M., and Pietra C. (2010). Heat recovery from Diesel engines: A thermodynamic comparison between Kalina and ORC cycles. *Applied Thermal Engineering*, 30(2-3), pp. 212-219.

Bombarda P., Invernizzi C., and Gaia M. (2013). Performance analysis of OTEC plants with multilevel organic Rankine cycle and solar hybridization. *Journal of Engineering for Gas Turbines and Power*, 135 (2013), pp. 1–8.

Borsukiewicz-Gozdur A. (2013). Experimental investigation of R227ea applied as working fluid in the ORC power plant with hermetic turbogenerator. *Applied Thermal Engineering*, 56, pp. 126-133.

Bracco R., Clemente S., Micheli D., and Reini M. (2013). Experimental tests and modelization of a domestic-scale ORC (Organic Rankine Cycle). *Energy*, 58, pp. 107-106.

Branchini L., De Pascale A., and Peretto A. (2013). Systematic comparison of ORC configurations by means of comprehensive performance indexes. *Applied Thermal Engineering*, 61(2), pp. 129-140.

Bronicki L.Y. (1988). Experience with high speed organic Rankine cycle turbomachinery. Conference on high speed technology, Lappeenranta Finland, 21-24 August 1998, pp. 47-61.

Bronicki L.Y. (2008). Advanced Power Cycles for Enhancing Geothermal Sustainability, 1,000 MW Deployed Worldwide, Power and Energy Society General Meeting - Conversion and Delivery of Electrical Energy in the 21st Century, 2008 IEEE, Pittsburgh, 20-24 July 2008, pp. 1-6.

Buecker D. and Wagner W. (2006). Reference Equations of State for the Thermodynamic Properties of Fluid Phase n-Butane and Isobutane. *Journal of Physical and Chemical Reference Data*, 35(2), pp. 929-1019.

Campana F., Bianchi M., Branchini L., Pascale A.D., Peretto A., Baresi M., Fermi A., Rossetti N., and Vescovo R. (2013). ORC waste heat recovery in european energy intensive industries: Energy and GHG savings. *Energy Conversion and Management*, 76, pp. 244–252.

Colonna P. (1991). Fluidi silossanici per cicli di potenza spaziali (Siloxane Fluids for Space Power Cycles). Master's thesis, Politecnico di Milano, Milano.

Colonna P. and van der Stelt T.P. (2004). FluidProp: a program for the estimation of thermo physical properties of fluids. Energy Technology Section, Delft University of Technology, The Netherlands.

Colonna P., Rebay S., Harinck J., and Guardone A. (2006a). Real-Gas Effects in ORC Turbine Flow Simulations: Influence of Thermodynamic Models on Flow Fields and Performance Parameters. Proceedings of the European Conference on Computational Fluid Dynamics, (ECCOMAS CFD 2006), P. Wesseling, E. Onate, and J. Périau, eds.

Colonna P. and Guardone A. (2006b). Molecular Interpretation of Nonclassical

Gasdynamics Phenomena in the Vapor Phase under the van der Waals Polytropic Model, *Physics of Fluids*, 18:056101, pp. 1-14.

Colonna P., Nannan N.R., Guardone A., and Lemmon E.W. (2006c). Multiparameter equations of state for selected siloxanes. *Fluid Phase Equilibria*, 244, pp. 193-211.

Colonna P., Nannan N.R., and Guardone A. (2008). Multiparameter equatios of state for siloxanes: [(CH3)3-Si-O1/2]2-[O-Si-(CH3)2]i=1,...,3, and [O-Si-(CH3)2]6. *Fluid Phase Equilibria*, 263, pp. 115-130.

Chacartegui R., Sánchez D., Muñoz J.M., and Sánchez T. (2009). Alternative ORC bottoming cycles for combined cycle power plants. *Applied Energy*, 86(10), pp. 2162-2170.

Chen H., Goswami D.Y., and Stefanakos, E.K. (2010). A review of thermodynamic cycles and working fluids for the conversion of low-grade heat. *Renewable and Sustainable Energy Reviews*, 14(9), pp. 3059-3067.

Chien K.Y. (1982). Predictions of Channel and Boundary-Layer Flows with a Low-Reynolds-Number Turbulence Model. *AIAA Journal*, 20, pp. 33-38.

Dambach R., Hodson H.P., and Huntsman I. (1999). An Experimental Study of Tip Clearance Flow in a Radial Inflow Turbine. *Journal of turbomachinery*, 121(4), pp. 644-650.

Drescher U. and Brüggemann D. (2007). Fluid selection for the Organic Rankine Cycle (ORC) in biomass power and heat plants. *Applied Thermal Engineering*, 27(1), pp. 223-228.

Fernández F.J., Prieto M.M., and Suárez I. (2011). Thermodynamic analysis of high-temperature regenerative organic Rankine cycles using siloxanes as working fluids. *Energy*, 36, pp. 5239-5249.

Grönman A. (2010). Numerical modelling of small supersonic axial flow turbines, PhD thesis, Lappeenranta University of Technology, Finland.

Grönman A., Turunen-Saaresti T., Röyttä P., Jaatinen A., and Backman J. (2013). Performance and flow fields of a supersonic axial turbine at off-design conditions, Proceedings of the Institution of Mechanical Engineers, Part A: *Journal of Power and Energy*, 227(3), pp. 285-294.

Guardone A. (2010). Real-Gas Effects in Supercritical Carbon Dioxide Gasdynamic Nozzle. HEFAT2010, Proccedings of 7th International Conference on Heat

Transfer, Fluid Mechanics and Thermodynamics, Antalya Turkey, 19-21 July 2010.

Guardone A., Spinelli A., and Dossena V. (2013). Influence of Molecular Complexity on Nozzle Design for an Organic Vapor Wind Tunnel. *Journal of Engineering for Gas Turbines and Power*, 135:042307, pp. 1-6.

Harinck J., Guardone A., and Colonna P. (2009). The Influence of Molecular Complexity on Expanding Flows of Ideal and Dense Gases. *Physics of Fluids*, 21:086101.

Harinck J., Turunen-Saaresti T., Colonna P., Rebay S., and van Buijtenen J. (2010). Computational Study of a High-Expansion Ratio Radial Organic Rankine Cycle Turbine Stator. ASME *Journal of Engineering for Gas Turbines and Power*, 132:054501.

Harinck J., Pasquale D., Pecnik R., van Buijtenen J., and Colonna, P. (2013). Performance improvement of a radial organic Rankine cycle turbine by means of automated computational fluid dynamic design. Proceedings of the Institution of Mechanical Engineers, Part A: *Journal of Power and Energy*, 227(6), pp. 637-645.

Heinimö J., van Buijtenen J.P., Backman J., Ojaniemi A., and Malinen H. (2004). High-speed ORC technology for distributed electricity production. 2nd World Conference on Biomass for Electricity, Industry and Climate Protection, Rome Italy, 10-14 May 2004.

Hoffren, J., Talonpoika, T., Larjola, J., and Siikonen, T. (2002). Numerical Simulation of Real-Gas Flow in a Supersonic Turbine Nozzle Ring. ASME *Journal of Engineering for Gas Turbines and Power*, 124(2), pp. 395–403.

Huber M.L., and Ely J.F. (1994). A predictive extended corresponding states model for pure and mixed refrigerants including an equation of state for R134a. *International Journal of Refrigeration*, 17, pp. 18-31.

Hung T.C., Shai T.Y., and Wang S.K. (1997). A review of organic Rankine cycles (ORCs) for the recovery of low-grade waste heat. *Energy*, 22(7), pp. 661-667.

Invernizzi C., Iora P., and Silva P. (2007). Bottoming micro-Rankine cycles for micro-gas turbines. *Applied Thermal Engineering*, 29, pp. 100-110.

Jaatinen A. (2009). Performance Improvement of Centrifugal Compressor Stage with Pinched Geometry or Vaned Diffuser. PhD thesis, Lappeenranta University of Technology, Finland.

Jokinen T., Larjola J., and Mikhaltsev I. (1998). Power Unit for Research Sub-

mersible. Proceedings of Elecship 98; International conference on electric ship, Istanbul Turkey, 1st September 1998, pp. 114-118.

Kang S.H. (2012). Design and experimental study of ORC (organic Rankine cycle) and radial turbine using R245fa working fluid. *Energy*, 41(1), pp. 514-524.

Karellas S., Schuster A., and Leontaritis A.D. (2012). Influence of supercritical ORC parameters on plate heat exchanger design. *Applied Thermal Engineering*, 33, pp. 70-76.

Khristenko P.I. (1961). On the thermodynamic feasibility of driving turbines with organic liquids heated in nuclear reactors. *Journal of Nuclear Energy*, Parts A/B. Reactor Science and Technology, 15(1), pp. 50-53.

Klonowicz P., Borsukiewicz-Gozdur A., Hanausek P., Kryllowicz W., and Brüggemann, D. (2014). Design and performance measurements of an organic vapour turbine. *Applied Thermal Engineering*, 63(1), pp. 297-303.

Lang W., Almbauer R., and Colonna, P. (2013). Assessment of waste heat recovery for a heavy-duty truck engine using an ORC turbogenerator. *Journal of Engineering for Gas Turbines and Power*, 135(4):042313, pp. 1–10

Larjola J. (1988). ORC power plant based on high speed technology. Conference on high speed technology, Lappeenranta Finland, 21-24 August 1988, pp. 63-77.

Larjola J. (1995). Electricity from industrial waste heat using high-speed organic Rankine cycle (ORC). *International Journal of Production Economics*, 41, pp. 227-235.

Leibowitz H. Smith I.K., and Stosic N. (2006). Cost effective small scale ORC systems for power recovery from low grade heat sources. Proceedings of IMECE 2006, IMECE2006-14284, Chicago Illinois, USA. 5-10 November 2006.

Lemmon E.W. and Huber M.L. (2004). Thermodynamic Properties of n-Dodecane. *Energy & Fuels*, 18, pp. 960-967.

Lemmon E.W. and Ihmels E.C. (2005). Thermodynamic Properties of the Butenes. Part II. Short Fundamental Equations of State. *Fluid Phase Equilibria*, 228-229C, pp. 173-187.

Lemmon E.W. and Span R. (2006). Short Fundamental Equations of State for 20 Industrial Fluids. *Journal of Chemical & Engineering Data*, 51, pp. 785-850.

Lemmon E.W, Huber M.L., and McLinden M.O. (2010). Reference fluid Ther-

modynamic and Transport Properties (REFPROP), Version 9.0. National Institute of Standards and Technology.

Lemort V., Quoilin S., Cuevas C., and Lebrun J. (2009). Testing and modeling a scroll expander integrated into an Organic Rankine Cycle. *Applied Thermal Engineering*, 29(14), pp. 3094-3102.

Liu B.T., Chien K.H., and Wang C.C. (2004). Effects of working fluids on organic Rankine cycle for waste heat recovery. *Energy*, 29(8), pp. 1207-1217.

Macchi E. (1977). Design criteria for turbines operating with fluids having a low speed of sound. Lecture series 100, on 'Closed Cycle Gas Turbines',Von Karman Institute for Fluid Dynamics, 9-13 May 1977.

Macchi E., and Perdichizzi A. (1981). Efficiency prediction for axial-flow turbines operating with nonconventional fluids. *Journal of Engineering for Power*, 103(4), pp. 718-724.

Madhava Hettiarachchi H.D, Golubovic M., Worek W.M., and Ikegami Y. (2007). Optimum design criteria for an Organic Rankine cycle using low-temperature geothermal heat sources. *Energy*, 32(9), pp. 1698-1706.

Menter F.R. (1993). Zonal two equation k-ω turbulence models for aerodynamic flows. 24th AIAA Fluid Dynamics Conference (Orlando, Florida), July 1993, AIAA Paper 93-2906.

Penoncello S.G., Goodwin A.R.H., and Jacobsen R.T. (1995). A Thermodynamic Property Formulation for Cyclohexane. *International Journal of Thermophysics*, 16(2), pp. 519-531.

Pini M., Persico G., Casati E., and Dossena V. (2013). Preliminary Design of a Centrifugal Turbine for Organic Rankine Cycle Applications. *Journal of Engineering for Gas Turbines and Power*, 135(4):042312, pp. 1-9

Platzer B., Polt A., and Maurer G. (1990). Thermophysical properties of refrigerants. Berlin, Springer-Verlag.

Qiu G., Shao Y., Li J., Liu H., and Riffat S.B. (2012). Experimental investigation of a biomass-fired ORC-based micro-CHP for domestic applications. *Fuel*, 96, pp. 374-382.

Quoilin S., Lemort V., and Lebrun J. (2010). Experimental study and modeling of an Organic Rankine Cycle using scroll expander. *Applied Energy*, 87(4), pp. 1260-1268.

Quoilin S., Declaye S., Tchanche B.F., and Lemort V. (2011). Thermo-economic optimization of waste heat recovery Organic Rankine Cycles. *Applied Thermal Engineering*, 31(14), pp. 2885-2893.

Rinaldi E., Buonocore A., Pecnik R., and Colonna P. (2013). Inviscid stator/rotor interaction of a single stage high expansion ratio ORC turbine. ASME ORC 2013: 2nd International Seminar on ORC Power Systems. Rotterdam, The Netherlands, 7-8 October 2013.

Roe P.L. (1981). Approximate Riemann solvers, parameter vectors, and difference schemes. *Journal of Computational Physics*, 43(2), pp. 357-372.

Rohlik H. (1975). Radial Inflow Turbines, Chapter 10 in Glassman A. J., Turbine Design and Application: Volume 1-3. NASA SP-290, 388 pages.

Saleh B., Koglbauer G., Wendland M., and Fischer J. (2007). Working fluids for low-temperature organic Rankine cycles. *Energy*, 32(7), pp. 1210-1221.

Sauer R. (1947). General characteristics of the flow through nozzles at near critical speeds. TM 1147, NACA.

Schuster A., Karellas S., Kakaras E., and Spliethoff H. (2009). Energetic and economic investigation of Organic Rankine Cycle applications. *Applied Thermal Engineering*, 29(8-9), pp. 1809-1817.

Schuster A., Karellas S., and Aumann R. (2010). Efficiency optimization potential in supercritical Organic Rankine Cycles. *Energy*, 35(2), pp. 1033-1039.

Seher D., Lengenfelder T., Gerhardt J., Eisenmenger N., Hackner M., and Krinn I. (2012). Waste Heat Recovery for Commercial Vehicles with a Rankine Process. In 21st Aachen Colloquium Automobile and Engine Technology, Aachen, Germany, 7-9 October 2012.

Siikonen T. (1995). An Application of Roe's Flux-Difference Splitting for the k-ϵ Turbulence Model. *International Journal for Numerical Methods in Fluids*, 21, pp. 1017-1039.

Span R. and Wagner W. (2003). Equations of State for Technical Applications. II. Results for Nonpolar Fluids. *International Journal of Thermophysics*, 24(1), pp. 41-109.

Sprouse III C. and Depcik C. (2013). Review of organic Rankine cycles for internal combustion engine exhaust waste heat recovery. *Applied Thermal Engineering*, 51(1-2), pp. 711-722.

Srinivasan K., Mago P. and Krishnan S. (2010). Analysis of exhaust waste heat recovery from a dual fuel low temperature combustion engine using an Organic Rankine Cycle. *Energy*, 35(6), pp. 2387-2399.

Straatman, P.J.T. and van Sark W.G.J.H.M. (2008). A new hybrid ocean thermal energy conversion–Offshore solar pond (OTEC–OSP) design: A cost optimization approach. *Solar Energy*, 82(6), pp. 520-527.

Talonpoika T. (1996). Dynamic Model of a Small Once-Through Boiler. PhD thesis, Lappeenranta University of Technology, Finland.

Tang J. (2006). Computational Analysis and Optimization of Real Gas Flow in Small Centrifugal Compressors. PhD thesis, Lappeenranta University of Technology, Finland.

Tchanche B.F., Lambrinos G., Frangoudakis A., and Papadakis G. (2011). Low-grade heat conversion into power using organic Rankine cycles - A review of various applications. *Renewable and Sustainable Energy Reviews*, 15(8), pp. 3963-3979.

Thol M., Lemmon E.W., and Span R. (2012). Equation of state for benzene for temperatures from the melting line up to 725 K with pressures up to 500 MPa. *High temperatures-high pressures*, 41(2), pp. 81-97.

Tillner-Roth R. and Baehr H.D. (1994). An international standard formulation of the thermodynamic properties of 1,1,1,2-tetrafluoroethane (HFC-134a) for temperatures from 170 K to 455 K at pressures up to 70 MPa. *Journal of Physical and Chemical Reference Data*, 23, pp. 657-729.

Turunen-Saaresti T. (2004). Computational and Experimental Analysis of Flow Field in the Diffusers of Centrifugal Compressors. PhD thesis, Lappeenranta University of Technology, Finland.

Turunen-Saaresti T., Tang J., and Larjola J. (2006). A Practical Real Gas Model in CFD. Proceedings of the European Conference on Computational Fluid Dynamics (ECCOMAS CFD 2006), P. Wesseling, E. Onate, and J. Périau, eds.

van Buijtenen J.P., Larjola J., Turunen-Saaresti T., Honkatukia J., Esa H., and Backman J. (2003). Design and validation of a new high expansion ratio radial turbine for ORC application. 5th European conference on Turbomachinery, Prague, 17-22 March 2003.

van Buijtenen J.P. (2009). The Tri-O-Gen Organic Rankine Cycle: development and perspectives. Power Engineer, Journal of the IDGTE (The Institution of Diesel and

Gas Turbine Engineers), 13(1).

Vaja I. and Gambarotta A. (2010). Internal Combustion engine (ICE) bottoming with Organic Rankine Cycles (ORCs). *Energy*, 35(2), pp. 1084-1093.

VDI-Wärmeatlas: (1988). Berechnungsblätter für den Wärmeübergang, VDI-Verlag, Düsseldorf, Germany, ISBN:3-18-400850-9.

Verneau A. (1987). Supersonic Turbines for Organic Fluid Rankine Cycles from 3 to 1300 kW: Small High Pressure Ratio Turbines. Von Karman Institute for Fluid Dynamics, Lecture series 7, 15-18 June 1987.

Wang E.H., Zhang H.G., Fan B.Y., Ouyang M.G., Zhao Y., and Mu Q.H. (2011). Study of working fluid selection of organic Rankine cycle (ORC) for engine waste heat recovery. *Energy*, 36(5), pp. 3406-3418.

Wang E.H., Zhang H.G., Zhao Y., Fan B.Y, Wu Y.T., and Mu Q.H. (2012). Performance analysis of a novel system combining a dual loop organic Rankine cycle (ORC) with a gasoline engine. *Energy*, 43(1), pp. 385-395.

Yang M.H. and Yeh, R.H. (2014). Analysis of optimization in an OTEC plant using organic Rankine cycle. *Renewable Energy*, 68, 25-34.

Zucrow M.H. and Hoffman J.D. (1977). Gas dynamics: multidimensional flow. Vol. 2. Wiley, Jhon & Son.

ACTA UNIVERSITATIS LAPPEENRANTAENSIS

574. LAMMASSAARI, TIMO. Muutos kuntaorganisaatiossa – tapaustutkimus erään kunnan teknisestä toimialasta. 2014. Diss.

575. KALWAR, SANTOSH KUMAR. Conceptualizing and measuring human anxiety on the Internet. 2014. Diss.

576. LANKINEN, JUKKA. Local features in image and video processing – object class matching and video shot detection. 2014. Diss.

577. AL-SAEDI, MAZIN. Flexible multibody dynamics and intelligent control of a hydraulically driven hybrid redundant robot machine. 2014. Diss.

578. TYSTER, JUHO. Power semiconductor nonlinearities in active d*u*/d*t* output filtering. 2014. Diss.

579. KERÄNEN, JOONA. Customer value assessment in business markets. 2014. Diss.

580. ALEXANDROVA, YULIA. Wind turbine direct-drive permanent-magnet generator with direct liquid cooling for mass reduction. 2014. Diss.

581. HUHTALA, MERJA. PDM system functions and utilizations analysis to improve the efficiency of sheet metal product design and manufacturing. 2014. Diss.

582. SAUNILA, MINNA. Performance management through innovation capability in SMEs. 2014. Diss.

583. LANA, ANDREY. LVDC power distribution system: computational modelling. 2014. Diss.

584. PEKKARINEN, JOONAS. Laser cladding with scanning optics. 2014. Diss.

585. PELTOMAA, JYRKI. The early activities of front end of innovation in OEM companies using a new FEI platform as a framework for renewal. 2014. Diss.

586. ROZHANSKY, IGOR. Resonant tunneling effects in semiconductor heterostructures. 2014. Diss.

587. PHAM, THUY DUONG. Ultrasonic and electrokinetic remediation of low permeability soil contaminated with persistent organic pollutants. 2014. Diss.

588. HOKKANEN, SANNA. Modified nano- and microcellulose based adsorption materials in water treatment. 2014. Diss.

589. HINKKANEN, JUHA. Cooperative strategy in emerging markets – analysis of interfirm R&D cooperation and performance in Russian manufacturing companies. 2014. Diss.

590. RUSKOVAARA, ELENA. Entrepreneurship education in basic and upper secondary education – measurement and empirical evidence. 2014. Diss.

591. IKÄHEIMONEN, TUULI. The board of directors as a part of family business governance – multilevel participation and board development. 2014. Diss.

592. HAJIALI, ZUNED. Computational modeling of stented coronary arteries. 2014. Diss.

593. UUSITALO, VILLE. Potential for greenhouse gas emission reductions by using biomethane as road transportation fuel. 2014. Diss.

594. HAVUKAINEN, JOUNI. Biogas production in regional biodegradable waste treatment – possibilities for improving energy performance and reducing GHG emissions. 2014. Diss.

595. HEIKKINEN, JANNE. Vibrations in rotating machinery arising from minor imperfections in component geometries. 2014. Diss.

596. GHALAMCHI, BEHNAM. Dynamic analysis model of spherical roller bearings with defects. 2014. Diss.

597. POLIKARPOVA, MARIIA.Liquid cooling solutions for rotating permanent magnet synchronous machines. 2014. Diss.

598. CHAUDHARI, ASHVINKUMAR. Large-eddy simulation of wind flows over complex terrains for wind energy applications. 2014. Diss.

599. PURHONEN, MIKKO. Minimizing circulating current in parallel-connected photovoltaic inverters. 2014. Diss.

600. SAUKKONEN, ESA. Effects of the partial removal of wood hemicelluloses on the properties of kraft pulp. 2014. Diss.

601. GUDARZI, DAVOOD. Catalytic direct synthesis of hydrogen peroxide in a novel microstructured reactor. 2014. Diss.

602. VALKEAPÄÄ, ANTTI. Development of finite elements for analysis of biomechanical structures using flexible multibody formulations. 2014. Diss.

603. SSEBUGERE, PATRICK. Persistent organic pollutants in sediments and fish from Lake Victoria, East Africa. 2014. Diss.

604. STOKLASA, JAN. Linguistic models for decision support. 2014. Diss.

605. VEPSÄLÄINEN, ARI. Heterogenous mass transfer in fluidized beds by computational fluid dynamics. 2014. Diss.

606. JUVONEN, PASI. Learning information technology business in a changing industry landscape. The case of introducing team entreneurship in renewing bachelor education in information technology in a university of applied sciences. 2014. Diss.

607. MÄKIMATTILA, MARTTI. Organizing for systemic innovations – research on knowledge, interaction and organizational interdependencies. 2014. Diss.

608. HÄMÄLÄINEN, KIMMO. Improving the usability of extruded wood-plastic composites by using modification technology. 2014. Diss.

609. PIRTTILÄ, MIIA. The cycle times of working capital: financial value chain analysis method. 2014. Diss.

610. SUIKKANEN, HEIKKI. Application and development of numerical methods for the modelling of innovative gas cooled fission reactors. 2014. Diss.

611. LI, MING. Stiffness based trajectory planning and feedforward based vibration suppression control of parallel robot machines. 2014. Diss.

612. KOKKONEN, KIRSI. From entrepreneurial opportunities to successful business networks – evidence from bioenergy. 2014. Diss.

613. MAIJANEN-KYLÄHEIKO, PÄIVI. Pursuit of change versus organizational inertia: a study on strategic renewal in the Finnish broadcasting company. 2014. Diss.

614. MBALAWATA, ISAMBI SAILON. Adaptive Markov chain Monte Carlo and Bayesian filtering for state space models. 2014. Diss.